2009

Turbulent structures in smooth and rough open channel flows: effect of depth

Vesselina Roussinova
University of Windsor

Recommended Citation

Roussinova, Vesselina, "Turbulent structures in smooth and rough open channel flows: effect of depth" (2009). *Electronic Theses and Dissertations.* Paper 94.

Turbulent structures in smooth and rough open channel flows: effect of depth

by

Vesselina Tzvetanova Roussinova

A Dissertation
Submitted to the Faculty of Graduate Studies
through Civil and Environmental Engineering
in Partial Fulfillment of the Requirements for
the Degree of Doctor of Philosophy at the
University of Windsor

Windsor, Ontario, Canada

2009

DECLARATION OF CO-AUTHORSHIP\PREVIOUS PUBLICATIONS

I. Co-Authorship Declaration

I hereby declare that this thesis incorporates material that is result of joint research, as follows:
This thesis also incorporates the outcome of a joint research undertaken in collaboration with Vesselina Roussinova under the supervision of professors Ram Balachandar and Nihar Biswas. The collaboration is covered in Chapters 2, 3, 4 and 5 of the thesis. In all cases, the key ideas, primary contributions, experimental designs, data analysis and interpretation, were performed by the author, and the contribution of co-authors was primarily through the provision of supervision

I am aware of the University of Windsor Senate Policy on Authorship and I certify that I have properly acknowledged the contribution of other researchers to my thesis, and have obtained written permission from each of the co-author(s) to include the above material(s) in my thesis.

I certify that, with the above qualification, this thesis, and the research to which it refers, is the product of my own work.

II. Declaration of Previous Publication

This thesis includes 4 original papers that have been previously published/submitted for publication in peer reviewed journals, as follows:

Thesis Chapter	Publication title/full citation	Publication status
Chapter 3	Roussinova, V., Biswas, N., and Balachandar, R. (2008). "Revisiting turbulence in smooth uniform open channel flow." *J. Hydr. Res.*, 46, 1, 36-48.	*published*
Chapter 4	Roussinova, V., Shinneeb A.-M. and Balachandar R. (2008) "Investigation of fluid structures in a smooth open channel flow using proper orthogonal decomposition (POD)" *J. Hydr. Engrg.*	*under review*
Chapter 5	Roussinova, V., and Balachandar R. (2008) "Effect of depth on flow past a train of rib elements in an open channel" *J. Hyd. Engrg.*	*under review*
Chapters 3 and 5	Roussinova, V., Biswas, N., and Balachandar, R. (2009) "Reynolds stress anisotropy in open channel flow." *J. Hydr. Engrg.*	*accepted for publication*

I certify that I have obtained a written permission from the copyright owner(s) to include the above published material(s) in my thesis. I certify that the above material describes work completed during my registration as graduate student at the University of Windsor.

I declare that, to the best of my knowledge, my thesis does not infringe upon anyone's copyright nor violate any proprietary rights and that any ideas, techniques, quotations, or any other material from the work of other people included in my thesis, published or otherwise, are fully acknowledged in accordance with the standard referencing practices. Furthermore, to the extent that I have included copyrighted material that surpasses the bounds of fair dealing within the meaning of the Canada Copyright Act, I certify that I have obtained a written permission from the copyright owner(s) to include such material(s) in my thesis.

I declare that this is a true copy of my thesis, including any final revisions, as approved by my thesis committee and the Graduate Studies office, and that this thesis has not been submitted for a higher degree to any other University or Institution

.

ABSTRACT

In this thesis, detailed experiments are performed to study the effect of the flow depth on turbulent structures in smooth and rough bed open channel flow. Shallow open channel flow is dominated entirely by the wall turbulence with a wall boundary layer that occupies a significant fraction of the flow depth. When the rough bed is introduced in the shallow flow, the local turbulence near the roughness element intensifies and becomes highly heterogeneous. The model roughness under study consists of a train of two dimensional square ribs spanning the whole length of the channel. The height of the ribs (k) occupy 10-15% of the depth of flow (d) and falls in the category of large roughness. The experimental program was designed to study k-and d-type roughnesses at intermediate flow submergence ($6 < d/\mathrm{k} < 10$). Velocity measurements were conducted using laser Doppler velocimetry (LDV) and particle image velocimetry (PIV) systems.

While on the smooth bed, mean velocity scaling in the classical logarithmic format was confirmed from the present experiments, for the deep-flow cases, turbulence quantities were found to be influenced by the free surface. A modified length scale based on a region of constant turbulence intensity is proposed to account for the effect of the free surface. The new length scale provides a better description not only for the mean velocity profiles but also for the Reynolds shear stress profiles and correlation coefficients. With the use of this new length scale, the estimation of the wake parameter is positive and provides for a more accurate estimate of the friction velocity.

Two-dimensional PIV measurements were made in the streamwise-wall normal plane of the smooth open channel flow at d = 0.10 m and Re_d = 21,000 ($Re_d = dU_0/\nu$) to further study the influence of the free surface on the turbulent structures. Proper orthogonal decomposition (POD) and swirling strength analysis were employed to investigate the structures present in the flow. Analysis of the POD reconstructed velocity fields reveals the presence of large-scale energetic structures near the free surface. These structures are almost parallel or slightly inclined to the free surface creating long zones with uniform momentum.

When large distributed bed roughness is introduced in the open channel, the anisotropy of the Reynolds stresses is reduced in the outer layer and found to depend on the rib spacing and roughness density. At shallow depth, the presence of roughness increases the turbulence intensities, Reynolds shear stress and higher-order moments in the outer layer of various locations along the rib wavelength. While for the shallow depth, the ratio of the shear contribution of sweep to ejection events is very different from that obtained on the smooth bed, for the deep flow cases, this difference diminishes in the outer layer.

DEDICATION

To my little daughter, Alexandra.

ACKNOWLEDGEMENTS

Many people contributed to this work and made it possible. I would like first to sincerely thank my advisors Dr. Ram Balachandar and Dr. Nihar Biswas for their inspiration, guidance and support during my PhD study at the University of Windsor.

I would also like to thank all of my colleagues Faruque, Arindam and Arjun with whom I shared an office for the last 5 years. Their curiosity and helpful discussions provided an enriching environment to work in.

Many thanks also go to Dr. Stefano Leonardi of the University of Puerto Rico-Mayagüez for making his DNS simulation on rough wall available to me.

I would like also to acknowledge the encouragement and support received from my family especially from my husband without him this work could not have been possible.

Finally, this work was made it possible by the financial support of the National Science and Engineering Research of Canada (NSERC) through Canadian Graduate Scholarship program and the University of Windsor Graduate Scholarship.

TABLE OF CONTENTS

I. INTRODUCTION

II. EXPERIMENTS

III. TURBULENCE IN SMOOTH UNIFORM OPEN CHANNEL FLOW

IV. TURBULENT STRUCTURES IN SMOOTH OPEN CHANNEL FLOW

V. EFFECT OF DEPTH ON FLOW PAST A TRAIN OF LARGE RIB ELEMENTS IN AN OPEN CHANNEL

VI. CONCLUSIONS, CONTRIBUTIONS AND FURURE RECOMENDATIONS

VII. REFERENCES

APPENDIX A

UNCERTAINTY ESTIMATES AND VELOCITY VALIDATION

LIST OF TABLES

LIST OF FIGURES

LIST OF SYMBOLS

$a_i(t)$ = temporal functions

u_τ = friction velocity (m/s)

u = fluctuating streamwise velocity measurement (m/s)

v = fluctuating vertical velocity measurement (m/s)

u' = instantaneous streamwise component (m/s)

v' = instantaneous vertical component (m/s)

u_{rms} = RMS streamwise component (m/s)

v_{rms} = RMS vertical component (m/s)

$\overline{u^2}$ = turbulence intensity (m^2/s^2)

$\overline{uv}_{ave}$ = average Reynolds shear stress contribution at every measurement point (m^2/s^2)

$-\overline{uv}$ = Reynolds shear stress (m^2/s^2)

$(uv)_{Q_i,H}$ = Reynolds shear stress contribution from a different quadrant at specific H (m^2/s^2)

$I(t)$ = detection function

Re_θ = Reynolds number based on momentum thickness (θ) $\left(\mathrm{Re}_\theta = \frac{\theta U_0}{\nu}\right)$

uv_{Q_i} = percent contribution from a given quadrant

H = hole size

A = constant

B = constant

b = width of the channel (m)

d = depth of flow (m)

g = acceleration due to gravity (m/s^2)

P_{Qi} = probability of occurrence of event

S_0 = open channel slope

U = average velocity (m/s)

U_0 = maximum average velocity (m/s)

y^+ = inner scaling ($y^+ = \frac{yu_\tau}{\nu}$)

Greek letters

Π = wake strength parameter

δ = boundary layer thickness (m)

δ' = constant turbulent intensity length scale (m)

ν = kinematic viscosity (m^2/s)

κ = Von Karman constant

ρ = fluid density (kg/m^3)

θ = momentum thickness $\theta = \int_0^d \frac{U}{U_0}\left(1-\frac{U}{U_0}\right)dy$

$\omega(\eta)$ = wake functions

τ_w = wall shear stress (Pa)

$\tau(y)$ = total shear stress (Pa)

η = dimensionless outer length scale (y/d)

$\phi_i(x)$ = spatial POD modes

CHAPTER

I. INTRODUCTION

1.1. Motivation

The present study investigates the characteristics turbulent structures in smooth and rough bed open channel flows (OCF). Flow in an open channel is unique because it is developing under a confinement bounded by side walls and by the free surface which is subject to atmospheric pressure. The flow is driven along the slope of the channel by the streamwise component of the weight of the liquid and the shear force on the channel boundaries is the main resisting force. While in the limit of infinite depth, flows in open channels could be described by the theory of classical turbulent boundary layers. On many practical applications and hydraulic engineering practice, this approximation is violated due to the finite shallow depth of flow. Open channel flows can be classified as shallow when the vertical length scale of the flow (usually the depth, d) is significantly smaller than the horizontal length scale (Jirka and Uijttewaal, 2004). Shallow OCF are common in practice and are also often generated in laboratory settings.

This research originated from the need to better understand the effect of the flow (water) depth on the turbulent structures present in smooth and rough bed open channel flows. Turbulent flow over a rough surface is of great practical importance and it has been the subject of numerous studies in fluids engineering. In hydraulic engineering, virtually all flows of interest (for examples, rivers and man-made channels) are considered rough with varying roughness height (k), shape, density, etc. Only a few limited laboratory investigations deal with the effects of large uniformly distributed roughness. In classical turbulent boundary layer flows, roughness is classified as large if the ratio of the boundary layer thickness, δ, to the roughness height, k, is less than 50. According to Jimenez (2004), in flows with $\delta/k < 50$, the effect of the roughness extends across the entire boundary layer. In fully developed turbulent open channel flow which will be discussed here in detail, the wall boundary layer occupies the entire depth of flow and thus $\delta = d$. Following the open channel flow terminology where the ratio of the d/k is known as submergence, Nikora et al., (2001), classified the rough open channel flow as shallow if $d/k < 10$. In this case, the classical boundary layer theory fails in search of the universal logarithmic law for the mean velocity profile and the turbulent statistics. For the case of open channel flow with large submergence ($d/k > 10$), the roughness is deeply buried into the boundary layer and there is enough space for the logarithmic layer to develop. Such flows can be described using theoretical concepts developed for classical rough turbulent boundary layers. The experiments reported in this thesis complement previous research on rough open channel flow and are particularly important since they fall in the transitional category between narrow and wide channels with respect to aspect ratio ($6 < b/d < 10$) and large distributed bed roughness with intermediate submergence of $6 < d/k < 10$.

Many studies have investigated the structure of turbulent boundary layer (TBL) on the smooth and rough walls. One interesting question that still remains is: what is the difference between the turbulent structure of turbulent boundary layer flow and open channel flow? In fact, can one state at what conditions the two will be the same? The obvious answer would be that if the depth of flow is infinite (no effect of the free surface) the two types of flow should be similar in the vicinity of the bed. This has implication for hydraulic engineers who need to know the practical limits where turbulent boundary layer correlations can be applied for the case of the open channel flow.

This study addresses a number of important questions about turbulent structures in open channel flow. A partial list of some questions might be as follows:

1. What is the effect of the flow depth on the turbulent structures in smooth open channel flow?
2. Why does shallow flow on a smooth bed lead to increasing friction (flow resistance) and how this increase relate to the turbulent structures?
3. Is the flow anisotropy reduced in the smooth shallow flow case and if so why?
4. What is the effect of the large 2-D distributed roughness on the turbulent structures in OCF?
5. What is the effect of depth on the turbulent structures in rough open channel flow?

Some answers to questions 1, 2, and 3 can be found in Chapters III and IV. These chapters address the effect of depth on the turbulent structures in uniform smooth open channel flow. In Chapter III, laser Doppler velocimetry (LDV) is used to acquire velocity measurements in smooth open channel flow at three different water depths. From the LDV data, information about the lower- and higher-order turbulence statistics is extracted as well as information for the conditional quadrant analysis and Reynolds stress anisotropy. In Chapter IV, two-dimensional particle image velocimetry (PIV) measurements are performed in the streamwise-wall-normal plane (x-y) of smooth open channel flow. The instantaneous velocity fields were analyzed using proper orthogonal decomposition (POD) and swirling strength to expose the vortical structures. The velocity fields were reconstructed using different combination of POD modes to expose the large-scale energetic structures and small-scale less energetic structures. The POD results were further combined with the results from the momentum analysis as well as with the conditional quadrant analysis performed on the instantaneous PIV maps at three different threshold levels. In Chapter V, the effect of the large roughness on the higher-order turbulence moments and Reynolds stress anisotropy is studied at three different roughness conditions for three depths of flow using a train of rib elements located in an open channel. The rib elements are composed of two-dimensional square rods spanning the width of the channel and are located throughout the length of the flume.

1.2. Background

Prior to describing the theoretical background, common notation is defined. The Cartesian coordinates (x, y, z) are used to denote streamwise, vertical (wall-normal) and transverse (spanwise) directions, respectively. The components of the mean velocity and turbulent fluctuations in these directions are denoted by (U, V, W) and (u, v, w). In Cartesian tensor notation, the mean and the fluctuation velocities in the positive x_i direction are denoted by U_i and u_i. In the forthcoming Chapters, $i = 1, 2, 3$ denote the streamwise, vertical and spanwise direction, respectively. Furthermore, the superscript "+" is used to represent the quantities in wall units (velocity normalized by u_τ and distance normalized by the viscous length scale ν/u_τ, where ν is the kinematic viscosity and u_τ is the wall friction velocity).

1.2.1. Turbulent boundary layers vs. open channel flows

Turbulent boundary layer (TBL) flows are external flows that develop a distribution of streamwise mean velocity *U(y)* near the solid wall. Such flows are of practical importance and the literature devoted to them is extensive. The simplest example of a turbulent boundary layer flow is that over a smooth flat plate. In this case, the boundary layer occurs at zero incidence so that the pressure gradient along the smooth wall is zero and the velocity outside the boundary layer is constant and equal to the free stream velocity (U_∞). The turbulent boundary layer is shown schematically in Figure I-1 and it is described by the following set of equations:

$$\begin{gathered}\frac{\partial U}{\partial x}+\frac{\partial V}{\partial y}=0 \\ U\frac{\partial U}{\partial x}+V\frac{\partial U}{\partial y}=\frac{\partial}{\partial y}\left(\nu\frac{\partial U}{\partial y}-\overline{uv}\right)\end{gathered} \tag{I.1}$$

With an appropriate model for the Reynolds shear stress ($-\overline{uv}$), the mean velocity components can be determined from Eq. (I.1) subject to appropriate initial and boundary conditions. The appropriate boundary conditions are

$$U(x,0)=V(x,0)=0, \quad U(x,y\to\infty)\to U_\infty(x)=U_0 \tag{I.2}$$

Note that in Eq. (I.2), U_0 is the maximum (free stream) velocity.

The structure and dynamics of zero-pressure gradient turbulent boundary layers over smooth walls have been extensively studied (see reviews by Robinson 1991 and Panton 2001) and the two-layer structure of the boundary layer flows is widely accepted. In Figure I–1, the profile of the mean velocity *U(x,y)* is shown at streamwise section (*x*) where flow is fully developed. In turbulent wall bounded flows, it can be shown that the viscosity (ν) and the wall shear stress (τ_w) are important parameters. From these quantities we define viscous scales that are the appropriate velocity and length scales in the near-wall region. These are the friction velocity $u_\tau\,(\;=\sqrt{\frac{\tau_w}{\rho}}\,)$ and the viscous length scale, $\delta_\nu = \frac{\nu}{u_\tau}$. The mean velocity gradient ($\frac{\partial U}{\partial y}$) in a fully developed channel flow is a universal non-dimensional function which depends on just two non-dimensional parameters so that

$$\frac{\partial U}{\partial y} = \frac{u_\tau}{y}\Phi\left(\frac{y}{\delta_\nu},\frac{y}{\delta}\right). \tag{I.3}$$

The idea behind the choice of the two parameters is that δ_ν is the appropriate length scale in the viscous region ($y^+ < 50$) while δ is the appropriate length scale in the outer region ($y^+ < 50$). While in the inner layer the mean velocity *U(y)* is dominated by the viscous processes (Figure I–1), in the outer layer the viscous effects are unimportant. Following Pope (2000), the inner layer is the region where $y/\delta < 0.1$ and the outer layer is where $y^+ > 50$. For sufficiently high Reynolds number, an inertial sublayer or logarithmic layer exists roughly in the region $30 < y^+ < 300$, $y/\delta < 0.2$. The viscous sublayer is the region where $y^+ > 5$, and the buffer layer is the region between the viscous layer and logarithmic layer $5 < y^+ < 30$. In Chapter III, the two-layer structure of the turbulent boundary layers is revisited and applied to the velocity distributions obtained on the smooth bed open channel flow.

In fully developed turbulent channel flow, the total shear stress $\tau(y) = \mu\frac{\partial U}{\partial y} - \rho\overline{uv} = \rho u_\tau^2(1-\frac{y}{\delta})$ decreases linearly from the value at the wall, to zero at

$y = \delta$, where $(-\overline{uv})_{y=\delta}$ and $\left(\frac{\partial U}{\partial y}\right)_{y=\delta}$ each vanish. In Figure I–1, the flattening of the mean velocity profile implies that viscous shear stress drops below the linear variation, so that the Reynolds shear stress must start from zero at the wall, increase to a maximum at some location, y_p, and then asymptote to the linear curve as the slope of $U(y)$ vanishes. The net force exerted by the Reynolds shear stress is $d(-\overline{uv})/dy$ and according to the variation of the Reynolds shear stress sketched in Figure I-1, the net force must be negative and roughly constant above y_p and positive below y_p. The mean transport of turbulent momentum represented by the net Reynolds force retards the mean velocity in the core of the flow and accelerates it near the wall, compared to the case of the laminar boundary layer. The increased mean velocity near the wall causes the gradient of the mean velocity to increase, leading to higher wall shear stress (τ_w). Since the Reynolds shear stress is the unclosed term in the momentum equation (Eq. (I.1)), the main question in wall turbulence concerns the mechanism responsible for creating the Reynolds shear stress. A possible mechanism can be explained by the presence of different organized motions (eddies) present in the wall flows that persists for a long time.

One of the fundamental notions in turbulence research is to break the complex, multiscaled, random turbulent motions into organized activities that are commonly called *coherent structures*. Coherent structures can be thought of as individual entities (eddies) that consist of parcels of vortical fluid occupying a confined space and possessing *temporal coherence*. Most of the early studies on turbulent structures in smooth-wall turbulent boundary layers have emphasized the flow organization in the inner (wall) region for $y^+ < 40$. A review of experimental work and discussions on the existence of such coherent structures are provided by Kline et al., (1967), Robinson (1991) and most recently by Adrian (2007), among many others. Based on flow visualization observations, Falco (1977) has illustrated several of the now well-known types of coherent structures in wall-bounded flows. Theodorsen (1955) had proposed that several of the structures take the form of hairpin-shaped loops. In this conceptual model, Theodorsen visualized a vortex filament oriented spanwise to the mean flow with the head part of the filament, located away from the wall. The vortex head is subjected to a greater mean velocity and it is convected downstream faster than the lower-lying ‘legs’. The lower-lying legs tend to get stretched causing the farther-lying parts to be lifted further into the flow.

Lu and Willmarth (1973) have shown that in the inner layer of turbulent boundary layers, the streamwise (u) and vertical (v) velocity fluctuations are anticorrelated most of the time. They developed a statistical conditional quadrant technique to further investigate the velocity fluctuations. Once u and v fluctuations are plotted on the u-v plane it was observed that most of the time they occupied quadrant 2 (Q2) and quadrant 4 (Q4) so that on average the product of u and v becomes negative. Events in the second quadrant correspond to negative streamwise fluctuations being lifted away from the wall by positive wall-normal fluctuations, and are referred to as *ejections*. Events in the fourth quadrant correspond to positive streamwise fluctuations being moved toward the wall. They are associated with motions called *sweeps*. Early flow visualization studies have shown that there is a sequence of events that came to be known as the *bursting cycle*, in which the fluid parcel streaks fluctuated vertically with increasing amplitude and then lifted away from the wall in a vigorous, chaotic motion. The bursting concept generated considerable interest, and many subsequent researchers sought mechanisms to explain the origin of explosive upward motions, using quadrant analysis of time series data to identify events occurring before and after the signatures of bursts. Of particular note is the mean tendency of Q2 events to be followed almost immediately by somewhat longer duration Q4 events, and the fact that Q2 events tend to occur in groups. In two dimensional channel flows, recent observations by Liu et al., (2001) have shown that the second quadrant (Q2) events are followed immediately by the fourth quadrant (Q4) events and there is a sequence of such events.

While the regions of strong second quadrant fluctuations ($u < 0$ and $v > 0$) are usually associated with the presence of the hairpin vortex core near the wall, there are many hairpin vortices in the outer region that are grouped in packets and the individual hairpin vortices in each packet travel in the streamwise direction with a relatively small dispersion in their velocity of propagation (Adrian et al., 2000). These packets grow in the streamwise direction creating long regions of the strongly retarded uniform momentum zones. The instantaneous configuration of packets determines the pattern of the zones of uniform momentum. Since the packets move with different velocities, the pattern is ever evolving. Meinhart and Adrian (1995) suggest that the long region of uniformly retarded flow in each zone is the backflow induced by several hairpins that are aligned in a coherent pattern in the streamwise direction. The near-wall sweep/ejection events cannot be described by the uniform momentum zone analysis. However, when combined with the quadrant analysis they provide better interpretations of the coherent structures (Hurther et al., 2007).

With the advent of the PIV technique and development of the direct numerical simulations (DNS), the concept proposed by Theodorsen (1995) was further extended and modified by Liu et al., (2001). In the review paper by Adrian (2007) the quasi-streamwise vortices, hairpin vortices, and packets of hairpins are prevalent coherent structures in wall turbulence that persist for a long time. The same concept of the coherent structures is applied to the case of smooth open channel flow and the results are discussed in Chapter IV.

Unlike turbulent boundary layers which are formed on a smooth wall in an unbounded domain, open channel flows develop in a channel confined by side walls and bounded by the free surface as shown in Figure I–2. Because of the existence of the free surface condition, the gravitational force is important and Froude number ($Fr^2 = U_o^2 / gd$) becomes an important dimensionless parameter. Here, U_0 is maximum velocity, g is the acceleration due to gravity and d is the depth of flow.

Most laboratory experiments in open channels have usually been performed at low Froude number (sub-critical conditions) in order to avoid disturbance of the free surface. This also restricts the Reynolds number from being very high. The usual treatment of uniform open channel flow is to assume that the channel is wide compared to the depth of flow and therefore the effect of the side walls is negligible or reduced. In computational models, the free surface is often simplified as a symmetry boundary (rigid–lid hypothesis). With these two approximations, the turbulent boundary layer equations (Eqs. (I.1)) can be further simplified to result in 1-D equations of motion for flow in rectangular, wide channel with small slope (S). With these assumptions, the flow in the central portion of the channel is described by the continuity equation,

$$\frac{\partial U}{\partial x} = 0\,, \tag{I.4}$$

and the momentum equation

$$0 = -\frac{1}{\rho}\frac{dP}{dx} + \frac{\partial}{\partial y}\left(\mu\frac{\partial U}{\partial y} - \rho\overline{uv}\right). \tag{I.5}$$

The effect of the bottom friction is usually described by the bed shear stress (τ_w) that is related to the bed friction velocity u_τ as

$$\tau_w = \rho u_\tau^2 \tag{I.6}$$

From 1-D momentum equation, the total shear stress becomes a sum of the Reynolds shear stress $-\rho\overline{uv}$ and the viscous stress, $\mu\frac{\partial U}{\partial y}$ similar to the case of the turbulent boundary layer discussed above. Consequently, the distribution of the total shear stress $\tau(y)$ in the vertical direction becomes

$$\tau(y) = \mu\frac{\partial U}{\partial y} - \rho\overline{uv} = \rho u_\tau^2(1-\frac{y}{d})\,. \tag{I.7}$$

In Eq. (I.7), the boundary layer thickness (δ) is replaced by the depth of flow (d) which is a characteristic of the fully developed open channel flow ($\delta = d$). This analysis shows that with some approximations the boundary layer equations can be applied successfully to describe the flow in open channels. Therefore, it has become a common practice among hydraulic engineers to apply correlations valid for turbulent boundary layers to flow in open channels. Even though such correlations might be useful, many of them are based only on the similarity of the mean velocity and their limitations should be known. In rough open channel flow, the effect of turbulence combined with channel confinement, surface roughness conditions and relative submergence (ratio between depth of flow, *d* and roughness height, *k*) could alter the flow resistance as well as the transport processes and needs further investigation.

Research on open channel flow turbulence has been conducted intensively only since the 1970s because of the development of the velocity measurement techniques such as hot-film anemometry, laser Doppler velocimetry (LDV), and particle image velocimetry (PIV). Since the present study deals with the analysis of the velocity measurements, a detailed descriptions of the velocity measurements techniques is provided in Chapter II. Almost all fundamental turbulent quantities (mean velocity and turbulent intensities) of various types of 2-D open-channel flows are now available and have been compared favorably with those of the other wall-bounded turbulent flows such as turbulent boundary layers and pipe flows. On the basis of the LDV measurements, Nezu and Rodi (1985) proposed a criterion for the relative importance of 3-D characteristics in open-channel flows in a rectangular cross-section with either fixed- or movable-boundary beds. They argued that when the channel aspect ratio b/d was smaller than 5, the maximum velocity on the channel centerline U_0 occurred below the free surface, the so-called velocity-dip phenomenon (Figure I–2), indicating that the effects of secondary currents were present. Nezu and Nakagawa (1993) reexamined the critical value of b/d (~5) and proposed that rectangular smooth bed channels could be classified according to whether the aspect ratio $b/d < 5$ (narrow channel) or $b/d > 10$ (wide channel). The boundary between the narrow and wide channels is not exactly defined. The aim of the present effort is to further understand the effect of flow depth and the changes in the turbulence structure under shallow flow conditions.

1.2.2. Shallow open channel flow

Jirka (2001) characterized shallow flows as largely unidirectional, turbulent shear flows driven by the piezometric pressure gradient and occupying a confined layer of depth (*d*). The situation is similar to one depicted in Figure I–2, where the flow is predominantly horizontal and occurs in a vertically limited layer whose depth is *d*. If the characteristic horizontal length scale *L* satisfied the following kinematic condition,

$$L/d >> 1 \tag{I.8}$$

the flow is classified as shallow. One practical example of the shallow open channel flow is the low-gradient river flows in alluvial channels classified by large width – to – depth aspect ratio, b/d ~ O(100).

The dynamic requirement for the shallow flow is related to the nature of the confinement surfaces. At least one boundary must be supporting the shear (e.g., the solid bed of the channel) while the other may be largely shear–free (e.g., the free surface in the open channel flow). The flow is then unidirectional and driven against the shear by the weight of the fluid. The velocity profile is influenced by the vertical shear and the Reynolds number ($Re = \frac{Ud}{\nu}$) is sufficiently large – greater than 1 x 10^3 so that the flow is fully turbulent. Here, Reynolds number is defined based on the *U* and *d,* where *U* is the characteristic velocity scale. The shallow open channel flow is governed entirely by the wall turbulence. In some cases, the mean velocity can still be characterized by the logarithmic – law of the wall as will be discussed in Chapters III and V. However, recent experiments by Pokrajac et al., (2007) in shallow open channel flows over rough beds have shown that the logarithmic layer will form only if there is enough space between the top of the roughness and the free surface. If this is not the case, the velocity profile may still have a logarithmic shape, but the parameters of the corresponding logarithmic law may not have the same physical meaning as the parameters of the universal logarithmic law of the wall. The structure of the turbulence in shallow flows is three-dimensional, produced by the ejection and sweep events of the shear layer near the smooth bed. Because of the shallow depth, most of the low-speed fluid parcels often reach the water surface, and at times still being attached to the bed. Nikora et al., (2007) speculate that these low-speed parcels can be viewed as clusters of fluid-made ‘cylinders’ randomly distributed in space and embedded into the faster moving surrounding flow. These “attached” eddies, can be responsible for weakening the horizontal eddies present in the flow providing for a very different mechanism of energy transfer. Some common turbulent structures such as the hairpin vortices with length scales smaller or on the order of the flow depth have been also found in shallow open channel flows and turbulent boundary layers (Nezu and Nakagawa, 1993).

The shallow flows are extremely susceptible to various kinds of disturbances, undergoing transverse oscillations which grow into the 2-D large–scale coherent structures in the transverse direction (Jirka and Uijttewaal, 2004). The length scale of these structures is much larger than the depth of flow ($l_{2D} \gg d$). Thus, confinement is responsible for a separation of turbulent motions between small scale three-dimensional turbulence ($l_{3D} < d$), and large scale two-dimensional turbulent motions ($l_{2D} \gg d$) with some mutual interactions. The effect of the confinement is manifested by the presence of the secondary currents. Such secondary currents (known as the ‘secondary currents of Prandtl’s second kind’) are generated by the non-homogeneity and anisotropy of turbulence. Even though the secondary currents are only 5% of the mean streamwise velocity and their size is less than the flow depth, they can have an important effect in altering the patterns of the streamwise velocities, bed shear, turbulence and sediment transport.

In shallow open channel flow, one can expect anisotropy in turbulence to be present mostly at the bed and at the free surface. Side wall effects are not important, since the channel is wide with aspect ratio $b/d > 10$. Narrow channels ($b/d < 5$) on the other hand can present strong secondary currents. Roughness can introduce another complexity to the shallow flow. It has been recognized that the bed roughness will influence the turbulence anisotropy and thus secondary currents; the extent of such influence has only been partially addressed by Naot (1984) and Tominaga et al., (1989). In Chapters III and V, the Reynolds stress anisotropy of the normal stresses $\overline{u^2}$ and $\overline{v^2}$ are examined to further quantify the effect of the shallow depth on smooth and rough bed open channel flows.

1.2.3. Rough open channel flow

Turbulent open channel flow over rough walls is a topic of significant interest and numerous publications have appeared in the last two decades. In his review on wall bounded turbulent flows, Jimenez (2004) analyzed experimental and theoretical work and noted that the effect of roughness is restricted to the region close to the wall, generally known as the roughness sublayer. Outside the roughness sub-layer, the flow structure is not directly affected by the presence of the rough wall. This conforms to the similarity hypothesis proposed by Townsend (1976) which states that the effect of roughness is limited to a wall-normal distance of 3 ~ 5 roughness heights (*k*) at sufficiently high Reynolds number and specifically for small values compared to the height of the turbulent boundary layer (δ). Based on existing experimental evidence, in order for the mean similarity to be valid, *k* should be less than 0.02δ. Recently, Connelly et al., (2006) provided experimental evidence that the self similarity of the mean velocity profile in a turbulent boundary layer is universal in the outer region for the relative roughness range beyond the criteria proposed by Jimenez (2004). Their experiments covered a range of roughness heights ranging from 0.009δ to 0.06δ and suggested that larger values of *k* require longer streamwise flow development length to attain a self-similar state.

Prior research has revealed some differences between the structure of turbulent flow over smooth and rough surfaces (Grass 1971, Krogstad et al., 1992, 1999, Djenidi et al., 1999). Krogstad et al., (1999) have shown that these differences exist even among different kinds of rough wall flows with almost identical mean velocity profiles in the approach flow. They have also questioned the validity of the Townsend’s hypothesis that the effect of the wall geometry will be forgotten after a few roughness heights from the bed. Their study indicates that despite the similarity in the mean velocity, the turbulent quantities are more indicative of the effect of the roughness. Lack of reliable measurements in the vicinity of the roughness elements combined with additional bias due to the use of different scaling approaches; continue to make the effect of roughness on turbulence in the outer layer a debated issue.

In this thesis, the roughness is constructed by using a train of 2-D square ribs. A brief overview of the literature pertaining to the study of the rib roughness in several flows is summarized below. In case of the rough surfaces constructed from a series of two-dimensional elements (such as ribs), it is possible to influence the overlying turbulence by altering the pitch separation (*p*) between the roughness elements. This was first observed by Perry et al., (1969) who classified such roughness as d- and k-type based on the pitch to roughness height ratio (p/k), with $p/k < 5$ considered as *d-type*; and $p/k \geq 5$ considered as *k-type*.

Okamoto et al., (1993) were among the first to study experimentally the turbulent boundary layer development over a rib roughness for a wide variety of pitch to height ratios (p/k) between 2 and 17. They used a Pitot tube to measure the mean velocities as well as the streamwise turbulent intensities. In the case of d-type roughness ($p/k < 5$), a stable recirculation region inside the cavity between adjacent ribs was observed. Flow visualization showed that the flow streamlines above the cavity region were not disturbed and on average the effect of surface roughness was quickly absorbed in the outer region. With increasing rib pitch, the flow inside the cavities start to reattach between successive ribs and at $p/k = 9$, the streamwise turbulence intensity attain a maximum value. A reduction of turbulent intensities was observed for all cases of $p/k > 9$. The development of the separating shear layer was also found to depend on the surface conditions.

A combination of laser-induced fluorescence (LIF) and laser Doppler velocimetry (LDV) was used by Djenidi et al., (1999) to study the structure of a turbulent boundary layer over a wall of two-dimensional square cavities classified as d-type roughness. All measurements were obtained at a distance x = 122k ($x^+ = xu_\tau/\nu$ = 13,313, x is the streamwise distance) at fully rough conditions, $k^+ = (ku_\tau/\nu)$ = 124, and the height of the roughness was k/δ = (0.11 - 0.14). Here, u_τ refers to the friction velocity. It was found that the cavity plays an important role by providing an outflow to the overlaying flow in a random manner. Flow visualization revealed that along the span of the cavities, outflows alternate with inflows, consistent with the alternating low-speed and high-speed streaks. The increase in turbulence intensities as well as the Reynolds shear stress was indicative for the strong outflow originating from the cavities. This suggests that the effects of the surface condition are not limited to the inner region but spread into the outer region. The authors hypothesized that by modifying the separation and/or the width of the cavities, the outflows will be influenced, resulting in different turbulent fields (mean velocity, Reynolds shear stresses). Thus, it might be possible to alter the level of interaction between the near-wall region and the outer flow in a manner that reflects the changes due to the disturbance to either the near-wall region or the outer region.

Because the measurement accuracy of all turbulent quantities drops in the immediate vicinity of the roughness, direct numerical simulations (DNS) can provide for a better understanding very close to the rough surface. The DNS solves directly the governing equations without imposing any assumptions but it is restricted to a moderate Reynolds numbers. A number of numerical studies of a boundary layer over a rib roughness have been recently conducted by Cui et al., (2003), Leonardi et al., (2004, 2006), Nagano et al., (2004), Krogstad et al., (2005), Ikeda and Durbin (2007) and Lee and Sung (2007). Different numerical methods as well as different roughness configurations have been investigated. Cui et al., (2003) used large eddy simulations (LES) to study the turbulent flow in a channel with transverse rib roughness on one wall. The study shows that for the k-type roughness, the separation and reattachment process is consistent with previous experimental studies. The simulations also revealed that larger and more frequent eddies are ejected outwards, resulting in strong interaction between the roughness and the outer flow. Using a similar geometry, Leonardi et al., (2004) performed the DNS simulation to investigate the effect of the rib separation on the organized structures near a rough wall. By analyzing the two-point velocity correlations, they found that with the increase of the pitch separation, the flow structures become less organized in the streamwise direction and the vertical motion emanating from the cavities becomes increasingly important. While for $p/k < 3$ the effect of the rough wall extends up to $2k$ above the plane of the ribs, for $p/k = 7$ this layer becomes as large as $5k$. Distributions of the normal vorticity show that the structure of the flow for larger $p/k > 7$ resembles the flow over a smooth wall with a presence of short streaky structures.

An experimental and DNS study of the fully turbulent channel flow with smooth and rod-roughened walls have been performed by Krogstad et al., (2005). The mean velocity confirms the existence of the portion of the velocity profiles where the law of the wall is valid for rough surfaces. In the outer region, no effect of the roughness was observed as suggested from the velocity defect law. Reynolds shear stress, quadrant and anisotropy analyses show that the smooth and the rough surface geometries appear to be very similar outside the roughness sub-layer ($y \approx 5k$). The 2-D closed channel flow result is very different from previous boundary layer results where the outer layer is very much affected by the roughness (Krogstad et al., 1992, 1999). The latter study speculated that the effect of the surface roughness on the outer layer may be dependent not only on the surface conditions but also on the type of flow: internal or external flow.

Most of the recent experiments in open channel flow (Tachie et al., 2003, Poggi et al., 2003 and Tachie et al., 2007) have been completed with laser based instrumentation and report various turbulence quantities. A low Reynolds number ($Re_d < 20{,}000$) experiment comparing turbulent quantities on a sand grain bed with that on the wire mesh roughness have been performed by Tachie et al., (2003). The height of the roughness varied from k/d = 0.01 to 0.03 and it was within the limit for the wall similarity to be valid proposed by Jimenez (2004). It was found that bed roughness enhances the levels of turbulence intensities, Reynolds shear stress and triple correlations over most of the outer layer. Close to the rough wall ($y/\delta < 0.1$), the Reynolds stress anisotropy was smaller than that on the smooth wall. At the edge of the turbulent boundary layer on the border between the turbulent/non-turbulent interface, the anisotropy was also reduced. Smalley et al., (2002) reported similar results for the anisotropy in boundary layers on smooth and rough walls. Tachie and Adane (2007), particle image velocimetry (PIV) was used to study the turbulence quantities in rough open channel flow over d- and k- type transverse ribs of different cross-section. The experimental conditions were such that only a few ribs were considered at the straight section of the flume which raises the question of the fully developed flow nature as well as the periodicity of the flow at the measurement location. The reported results are in line with the previous studies on rib roughness confirming that for k-type roughness, the interaction between the shear layers produces higher turbulence. It was also found that the flow acceleration had no significant effect on the flow resistance.

The small scale structure of turbulence in rough open channel flow was studied by Poggi et al., (2003). High resolution LDV system was used to acquire data near the wire mesh rough wall (k/d = 0.02) at a vertical location y^+ = 23. A lower level of intermittency and anisotropy was observed at the rough conditions. Energy spectra and high order structure functions suggest a link between the lower anisotropy and the increase of turbulent energy which is injected from the roughness. The integral structure functions shows that the small scale structures in the rough open channel are affected beyond the near wall region ($y^+ = 400$) and they have direct impact on the larger structure existing in the outer layer.

None of the above mentioned studies consider the effect of the flow depth systematically. In many practical applications in environmental hydraulics, natural streams and overland flows belong to the class of shallow hydraulically rough-bed open channel flows. In such flows, the relative ratio of depth of flow to the roughness height can affect not only the flow itself but also alter the transport of sediments and pollutants. Nikora et al., (2001) developed classification of shallow flows based on the value of the relative submergence defined as the ratio between the water depth (d) and roughness height (k). For the case of rough open channel flow with large submergence, where the roughness is deeply buried into the boundary layer there is enough space for the logarithmic layer to develop. Such flows can be described using theoretical concepts developed for turbulent boundary layers. Significantly less is known for the case of rough flows with small submergence ($d/k < 10$) where the existing boundary layer theory fails in search of the universal law for the mean velocity profiles and turbulent statistics. Manes et al., (2007) studied rough open channel flow with small submergence ($2.3 < d/k < 6.5$) using double-averaged Navier-Stokes equations. They were able to identify the presence of the logarithmic layer only for the case of $d/k = 6.5$. Once the logarithmic layer is absent, the experimental data cannot be fit with the universal law since the shape of the velocity profile is not known a priori. Despite the absence of the logarithmic layer, reasonable collapse of the double–averaged velocity profiles in the outer layer was obtained for all flow cases reported by Manes et al., (2007). This suggests that for shallow open channel flow the structure of the outer layer is preserved and maintains its characteristics irrespective of the bed conditions (smooth and rough). It is interesting to note that the experiments by Manes et al., (2007) were conducted in a flume with channel aspect ratio of $5 < b/d < 15$ where the secondary currents may also affect the flow. According to Nezu and Nakagawa (1993) the smooth channel should be considered narrow if the channel aspect ratio is $b/d < 5$ or wide if it is $b/d \geq 10$. In open channels, not only the bed conditions but also the lateral walls and free surface contribute to the mechanism of suppression/formation of secondary currents. There are still not enough systematic studies available that document the effect of the bed roughness conditions on the development of the secondary currents. The experiments reported in this thesis, complement previous research on open channel flow and are particularly important since they fall in the transitional category between the narrow and wide channels with aspect ratio of $6 < b/d < 10$ with large distributed bed roughness with intermediate submergence of $6 < d/k < 10$.

1.3. Research objectives and thesis overview

The present thesis investigates effect of the flow depth on turbulence structures in smooth and rough bed open channel flows. Understanding the effect of the depth is important not only from a scientific point of view but also to assess the limitations of the commonly used correlations in hydraulic engineering. In many practical applications in environmental hydraulics, the flows are considered shallow which can have a profound impact on the turbulence, flow resistance and sediment transport. Information provided herein for the roughness effects at shallow flow condition is an important first step towards better understanding of the flow over artificial bed forms such as dunes and ripples encountered in natural alluvial channels. To understand better the flow and transport implications of such bed feature at shallow conditions, the present work reports on measurements of mean and turbulent characteristics of flow over model train of large 2-D ribs using laser Doppler velocimetry (LDV).

Chapter II discussed the flow facilities and provide detailed description of the velocity measurement techniques employed. In Chapter III, single point 2-D LDV measurements are performed to examine the effect of the depth in smooth open channel flow at Reynolds number $Re_d > 30,000$. Two-dimensional PIV measurements performed in the streamwise-wall normal (x-y) plane are analysed in Chapter IV to expose the turbulent structures near the free surface. Chapter V deals with the analysis of the 2-D LDV measurements obtained on the rough bed in open channel flow under different roughness conditions and flow depths.

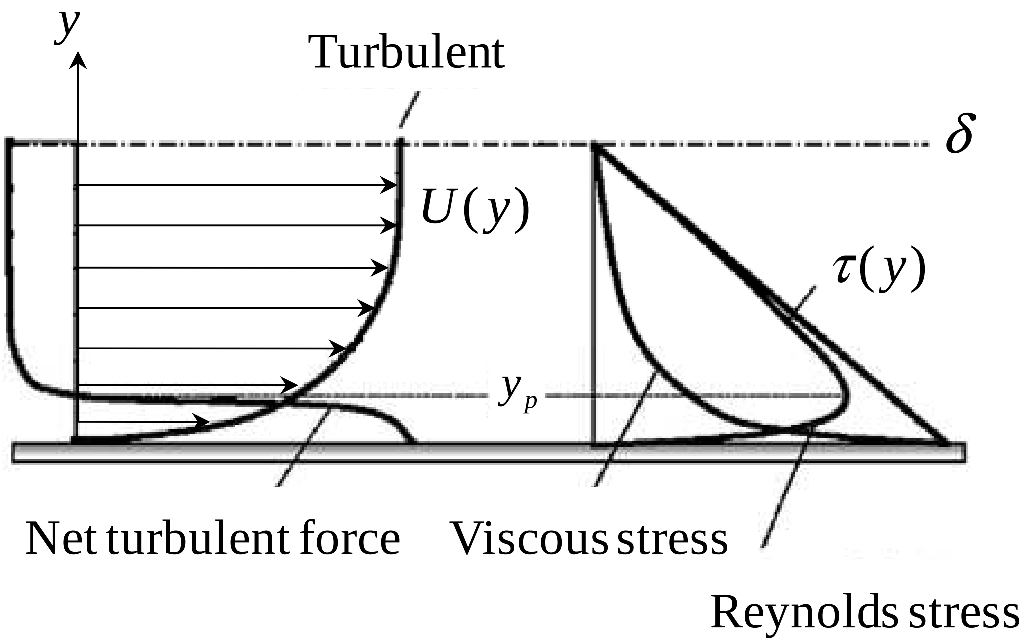

Figure I-1. Velocity profile and variations of Reynolds shear stress and viscous stress in a turbulent channel flow.

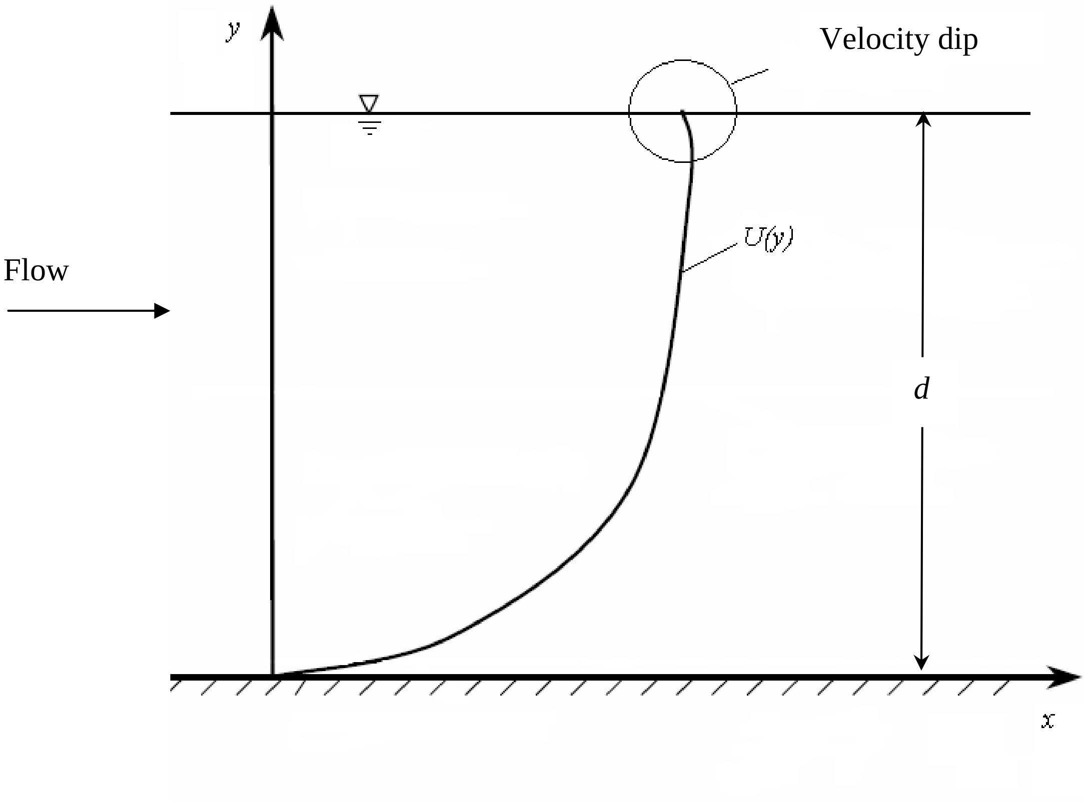

Figure I-2. Velocity profile of uniform smooth open channel flow.

CHAPTER

II. EXPERIMENTS

This chapter summarize the experiments undertaken in this study including a description of the flow facilities and detailed descriptions of the laser Doppler velocimetry (LDV) and particle image velocimetry (PIV) techniques. Typical uncertainty estimates and validation of the velocity measurements are also provided in Appendix A.

2.1. Open channel flume facilities

The experiments on smooth and rough bed OCF were conducted in a rectangular tilting flume with 610 x 610 mm cross-section and 10 m long. A settling tank as well as a contraction section was located at the entrance to the flume. At the end of the flume, water was collected through a diffusing section and recirculated with a pump. For all experiments, the measurement station was selected to be at least 70*d* (depths) away from the flume entrance to ensure that the flow is in a fully developed stage and in the middle of the channel where the effect of the secondary currents is negligible. The flow depth for the smooth wall experiments was varied and the Reynolds number based on the momentum thickness (= Re_θ) and Froude number (= Fr) are indicated in Table II-1. In the case of the fully developed open channel flow, the momentum thickness was defined by

$$\theta = \int_0^d \frac{U}{U_0}\left(1 - \frac{U}{U_0}\right) dy \tag{II.1}$$

In Eq. (II.1), the limit of the integral was modified and the boundary layer thickness (δ) is replaced by the depth of flow (*d*) which is a characteristic of the fully developed open channel flow ($\delta = d$). The flow conditions for all cases are fully turbulent and subcritical. The mean velocity profiles were obtained at streamwise locations ±100 mm of the measurement station to ensure that the flow is fully developed.

The rough bed consists of a long train of rib elements positioned along the flume length at three different pitch separations p/k (Figure II–1). The roughness elements were equally spaced so that the flow pattern repeats along the flume bed. All the experiments were conducted at a location $x = 6.7$ m (or $x/d = 70$) from the flume entrance where the flow was verified to be fully developed. The normalized streamwise distance, x^+ $(= xu_\tau/\nu)$ measured from the start of the rectangular cross-section, for $p/k = 4.5$ was $x^+ = 279 \text{ x } 10^3$, for $p/k = 9$ was $x^+ = 356 \text{ x } 10^3$ and $x^+ = 340 \text{ x } 10^3$ for $p/k = 18$. The flow development length depends not only on the distance from the flume entrance, but also on the upstream flow conditions. While the measurement location for all experiments was kept constant, the upstream conditions were somewhat different. More ribs were part of the roughness train for the lower pitch ratio of $p/k = 4.5$ (measurements were conducted on the top of the 147th rib) compared to $p/k = 9$ (measurements were conducted on top of the 74th rib) and $p/k = 18$ (measurements were conducted on top of 36th rib). The present number of ribs for $p/k = 18$ is larger than that used in most previous studies. For example, Connelly et al. (2006) reported experiments on the rough surfaces at $x = 1.35$ m ($x^+ = 180 \text{ x } 10^3$), Djenidi et al. (1999) reported 2-D LDV measurements at $x = 0.610$ m ($x^+ = 133 \text{ x } 10^3$), Bakken et al. (2005) measured with X hot-wires at $x = 4.95$ m ($x^+ = 59.4 \text{ x } 10^3$) and Agelinchaab and Tachie (2006) measured with PIV (for k-type ribs) at x = 0.072 m (x^+ = 1.52 x 10^3). The measurement location and the corresponding k^+ values summarized in Table II-2, reveal that the flow is in a turbulent, fully rough regime. In Table II-2, the values of the u_τ(= $\sqrt{gdS_0}$) are calculated based on the measured slope of the channel (S_0). There are two criteria by which the fully developed flow condition for the present rough experiments was assessed. First, the mean velocity profiles were inspected at the measurement location and the boundary layer thickness (δ) was found equal to depth of flow (d) which is a characteristic of fully developed open channel flow. Secondly, the mean velocity and turbulence intensity profiles on top of two neighbouring ribs were measured and a match of the two profiles was obtained for all cases confirming that the flow is spatially periodic.

Additional information for the rib tests is listed in Table II-2. The Reynolds number based on the maximum velocity (U_0) and d was higher than 25,000 for all experiments. At these flow conditions, it is reasonable to assume that the effect of Reynolds number on the turbulence characteristics is negligible. The Froude number ($Fr^2 = U_0^2 / gd < 0.28$) is low ensuring that the flow is in the sub-critical range.

The PIV measurements analyzed in Chapter IV were conducted in a re-circulating open channel flume having a straight, rectangular cross-section 9.5 m long and 1.2 m wide. The water depth d was maintained uniform at 0.10 m. A high channel aspect ratio (= 12) was deliberately chosen to minimize the secondary flow effects (Nezu and Nakagawa, 1993). A sand trip was installed at 3 m from the flume entrance. The test section was located at 1.5 m downstream of the sand trip and the measurement plane was chosen to be in the middle of the channel. The flow was fully developed in the measurement section with a maximum velocity of 0.19 m/s, corresponding to a Reynolds number based on the water depth ($Re_d = U_0 d/\nu$) of 21,000. Prior to the experiment, the water in the flume was filtered through a 5 μm filter. Then, the water was seeded with hollow glass bead particles with a specific gravity of 1.1 and a mean diameter of 12 μm.

2.2. Velocity measurements

2.2.1. Laser Doppler velocimetry (LDV)

The laser Doppler velocimeter (LDV) is an instrument for collecting single point velocity measurements in laboratory flows. It is non–intrusive, operates in highly turbulent flows and has better spatial resolution then the Pitot tube and hot-wire systems. An LDV system is superb for collecting thousands of instantaneous velocity samples in a well-defined region of space and thus providing accurate single point measurement of turbulence quantities of interest.

In this thesis, a commercial two-component LDV system (TSI Inc.) powered by a 2W Ar-Ion laser was used for the velocity measurements which was borrowed from the University of Iowa. The system consists of a 2W Argon Ion laser, optical system with a Bragg cell and 300 mm focusing lens. The beam spacing was 50 mm and the half angle was 3.96°. The LDV system is operated in backward scattering mode. For all experiments, the LDV system with a coincidence window size of 1,000 μs was adopted. Details of the choice of the window are available in an earlier study (Balachandar and Patel 2005) and are omitted here for brevity. No statistically significant differences in the mean velocity were noted by varying the sample size from 5,000 to 20,000. Data rates of the order of 60–80 Hz were obtained while operating the system in a coincidence mode. At each measurement location, 10,000 validated samples were acquired. A standard residence-time-averaging procedure was used. Due to the restrictions imposed by the geometry of the transmitting optics, two-component velocity measurements were possible only in the mid-85% of the flow depth, while one-component (streamwise velocity) measurements were made over the entire depth. For the rib tests, some modifications were made to the channel support structures and additional near-wall measurements were possible.

In an LDV system, the raw instantaneous velocity data (as a function of time) are collected whenever seeding particles traverse the measuring volume. The process of particle arrivals is random and it should follow normal (Poisson) distribution. A number of distinct deviations from the normal distribution can occur due to incorrect settings of the burst validation criteria, dead time of the processor, velocity/ particle bias, arrival time noise and multiple validations. Multiple validations occur if two particles simultaneously are present in the measuring volume, which results in false detection of the signal processor. All of the above factors are important error sources and they are considered in the uncertainty analysis of the present velocity measurements which is discussed in detail in Appendix A.

2.2.2. Particle image velocimetry (PIV)

The PIV system consists of dual pulse Nd:YAG lasers of 532 nm wavelength and 400 mJ/pulse. The laser sheet was formed through a 1000 mm spherical lens and expanded through a cylindrical lens. The light sheet was oriented vertically and included the streamwise wall-normal (*x, y*) central plane of the flume. The laser sheet was illuminated from the bottom of the flume while the optical axis of the camera was positioned perpendicular to it. The images were recorded using a TSI PowerViewPlus 4 MP 12-bit digital camera with a resolution of 2048 × 2048 pixel operating in dual capture mode. A TSI PIV LaserPulse synchronizer was used to synchronize the operation of the camera with the laser. The camera was fitted with a 28-105 mm Zoom-Nikkor lens and adjusted to give the desired field-of-view. 2000 image pairs were acquired at a frequency of 1.04 Hz and a time separation of 1.7 ms between consecutive frames. The images were analyzed using a commercial software *Insight 3G*® developed by TSI. The images were analyzed with 32 × 32 pixels interrogation area and 50% overlap using a FFT correlator. The correlation peak was located within sub-pixel accuracy using a Gaussian curve-fitting method. This process yielded a final interrogation area with a size of 16 × 16 pixels. For the field-of-view of 100 mm x 100 mm and camera resolution of 2048 x 2048 pixels used in the present PIV measurements 1 pixel corresponds to 0.049 mm and the actual spatial resolution that this process yielded is 0.79 mm. Very near the wall, velocities smaller than the measurement limit were discarded and the inner scaled PIV grid spacing resolution in streamwise and wall-normal directions are $\Delta x^+ = \Delta y^+ = 7.8$. The closest locations near the free surface where reliable velocity measurements were acquired was at $y/d = 0.85$.

After the correlation analysis was complete, velocity outliers were rejected using the cellular neural network method with a variable threshold as proposed by Shinneeb et al., (2004). This technique uses information about the local velocity gradient in the flow to make a suitable choice for the local threshold. The percentage of rejected vectors was ~8% and they are primarily located at the edges of the velocity fields. The rejected vectors were replaced using a Gaussian-weighted interpolation scheme. PIV validation as well as uncertainty analysis of the velocity measurements is presented in Appendix A.

Table II-1. Experimental conditions for the smooth OCF experiments.

Channel aspect ratio (*b/d*)	Flume width *b* = 610 mm			
	S_0x10^{+3}	Re_θ^*	Froude number (*Fr*)	$Re_x^{**}\times10^{-6}$
6.0	0.80	2979	0.50	3.6
7.5	0.85	3350	0.56	3.4
10.0	0.95	4824	0.65	3.5

$^*Re_\theta$ is defined based on the momentum thickness

$^{**}Re_x$ is defined based on the streamwise location

Table II-2. Experimental conditions for the rough OCF tests.

Surface type	Pitch ratio (p/k)	Depth d (mm)	k/d	U_o (m/s)	$Re=U_od/\nu$	$Fr^2=U_o^2/gd$	u_τ (m/s)	k^+
Rough	4.5	100	0.10	0.5	56287	0.25	0.037	417
Rough	9	105	0.10	0.51	55008	0.25	0.052	534
Rough	9	85	0.12	0.45	40420	0.24	0.046	486
Rough	9	65	0.15	0.36	25965	0.20	0.043	477
Rough	18	105	0.10	0.51	61772	0.25	0.044	508
Rough	18	85	0.12	0.46	43595	0.25	0.041	457
Rough	18	65	0.15	0.36	27560	0.20	0.037	436

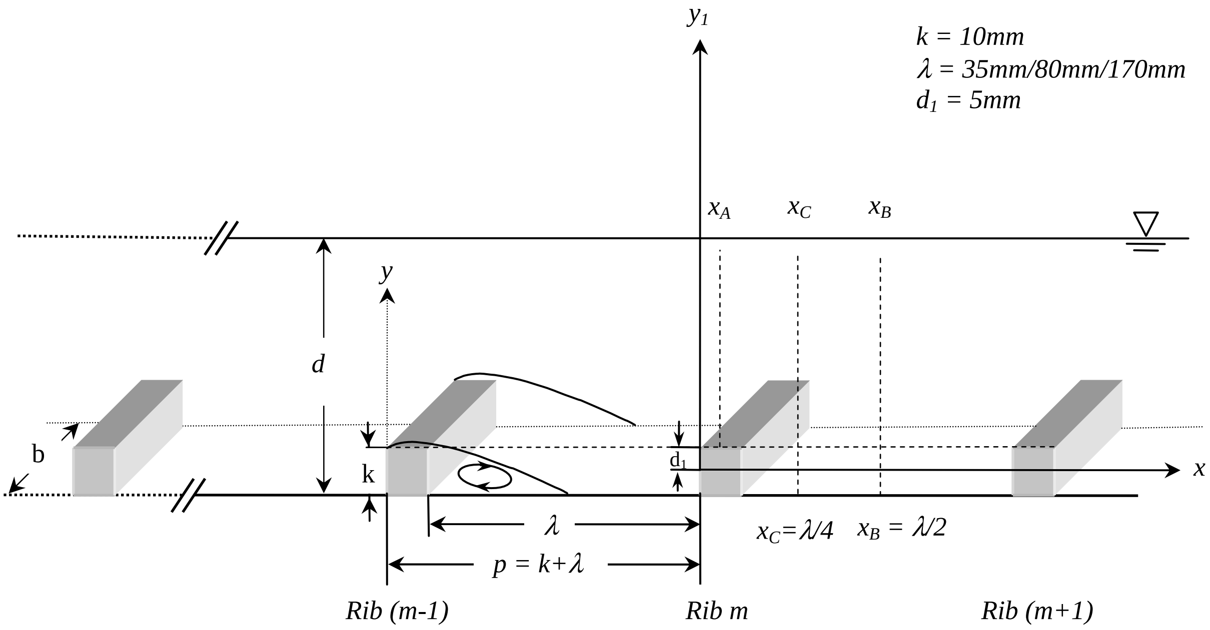

Figure II-1. Turbulent flow over a train of ribs (not to scale).

CHAPTER

III. TURBULENCE IN SMOOTH UNIFORM OPEN CHANNEL FLOW

The conventional approach used to describe flow in open channels borrows ideas from the general theory of turbulent boundary layers. In search of a universal mean velocity scaling law that will collapse the velocity profiles on to a single curve, hydraulics engineers have resorted to using classical relations developed for turbulent boundary layers. Similar to turbulent boundary layers, the velocity distribution in open channel flow is divided into inner and outer regions with two distinct sets of characteristic velocity and length scales. In the inner region closest to the wall, the friction velocity $u_\tau = (\tau_w / \rho)^{1/2}$, is the appropriate velocity scale, and the characteristic length scale is ν / u_τ. Here, τ_w is the wall shear stress and ν is the kinematic viscosity of the fluid. Since the direct measurement of the wall shear stress is rather difficult, the standard approach has been to compute the u_τ from the measured velocity distribution. An accurate estimate of u_τ is required in order to test for self-preservation of not only the mean flow but also the higher order turbulent moments. Traditionally, in the outer region of the fully developed open channel flow the depth of flow (d) is used as the characteristic length scale while maximum velocity U_0 is a characteristic velocity scale.

Even though analogies exist between turbulent boundary layers and the flow in open channels, there are important differences influenced by the channel geometry and the presence of the free surface (Nezu and Rodi 1986, Nezu 2005). A majority of the experimental evidence in open channel flow seems to support the existence of a region near the wall where the velocity profiles scale logarithmically. Steffler et al., (1985), Nezu and Rodi (1986) and Balachandar et al., (2002) have shown that there is an overlap layer ($30 \le y^{+} \le 0.2\frac{du_{\tau}}{\nu}$), where the mean velocity profiles agree well with the classical log-law given as:

$$\frac{U}{u_{\tau}} = A\ln\left(\frac{yu_{\tau}}{\nu}\right) + B \qquad \text{(III-1)}$$

An estimate of the friction velocity can be obtained by assuming the validity of the log-law. Clauser (1956) found that the constants A and B in the logarithmic equation to be 2.44 and 5.0 (Hinze, 1959). These values are adapted on the basis of various experimental data obtained for the case of turbulent boundary layers on smooth plates. The existence of the universality of the log-law has been also confirmed by the recent direct numerical simulations (DNS) for a turbulent boundary layer over a smooth plate (Spalart, 1988) and a two-dimensional channel. For the case of smooth open channel flow, it was found that the value of constant A is the same as that proposed by Clauser (1956) and it is independent of both Reynolds number and Froude number. Different values have been reported for constant B. Nezu and Rodi, (1986) reported value of B = 5.29, while Steffler et al., (1985) found that the value of B is 5.5. Values ranging from 5.0 to 5.5 have been commonly used.

The velocity distribution in the turbulent boundary layer farther from the wall ($y/\delta >$ 0.2), is not affected by viscosity and the characteristic velocity scale is defined by the free stream velocity, U_0 at $y = \delta$, while the characteristic length scale is the boundary layer thickness, δ. Coles (1956) was among the first to propose a modified velocity defect law by combining two universal functions: the law of the wall and the law of the wake. The defect law in a turbulent boundary layer therefore can be expressed as:

$$\frac{U}{u_\tau} = \frac{1}{\kappa}\ln y^+ + B + \frac{2\Pi}{\kappa}\omega\left(\frac{y}{\delta}\right) \tag{III.2}$$

The non-dimensional quantity Π is called the wake strength parameter and its value is generally flow dependent. Coles (1956) showed that in the outer region of the turbulent boundary layer where the flow is mainly controlled by turbulence, the velocity defect law reads:

$$\frac{U_e - U}{u_\tau} = -\frac{1}{\kappa}\ln\left(\frac{y}{\delta}\right) + \frac{2\Pi}{\kappa}\cos^2\left(\frac{\pi}{2}\frac{y}{\delta}\right) \tag{III.3}$$

In Eq. (III.3), Π is the Coles' wake parameter and it is a measure of the deviation of the velocity distribution from the log-law in the outer region. Coles found that for zero-pressure gradient smooth boundary layers the value of Π is 0.55 at high Reynolds numbers. In dealing with velocity profiles in the outer region of smooth open channel flows, Nezu and Rodi (1986) have noted that Π is dependent on Reynolds number and decreases with decreasing Reynolds number. This is very important as most laboratory studies are usually conducted at lower values of Reynolds number while field applications can be at considerably larger values. Cardoso et al., (1989) noted that values of Π varied from –0.27 to +0.02 in smooth, uniform open channel flow. Kirkgoz and Ardichoglu (1997) have also indicated very low values of Π (≈ 0.1) for the case of open channel flow. Krogstad et al., (1992) reviewed the velocity defect equation (Eq. (III.2)) and based on the study by Granville (1976), they proposed the following form of the velocity defect law for smooth turbulent boundary layers

$$\frac{U_e - U}{u_\tau} = \frac{2\Pi}{\kappa}\left[1 - \frac{1}{2\Pi}\left((1+6\Pi)\left(\frac{y}{\delta}\right)^2 - (1+4\Pi)\left(\frac{y}{\delta}\right)^3\right)\right] - \frac{1}{\kappa}\ln\frac{y}{\delta} \tag{III.4}$$

Balachandar et al., (2001) and Tachie et al., (2000) have applied Eq. (III.4) to flow in an open channel, and by optimization of both parameters, Π and u_τ, they found different Π values. In Tachie et al., (2003) it was shown that the value of the wake parameter depends strongly on the wall condition. Larger values of Π are obtained on the rough surfaces providing an indication that the roughness effects are not confined only near the wall. These results are in line with the observations of Krogstad et al., (1992) for the case of the zero pressure gradient turbulent boundary layers.

All of the aforementioned differences between classical turbulent boundary layers and flows in open channels can be attributed to the constrained flow condition that exists in open channels. These constraints are due to the presence of the free surface and the sidewalls of the channel. The proximity of the free surface does not allow for developing of a region of a constant free stream velocity observed in the fully developed turbulent boundary layer. In open channel flow, the maximum velocity is attained slightly below the free surface as documented by Cardoso et al., (1989) and Balachandar and Patel (2002). The presence of the free surface has two effects on the turbulence charactersistics as discussed by Rashidi et al., (1990). The first effect is similar to the effect of the solid boundary where velocity fluctuations in the direction normal to the boundary are surppessed by the effect of the surface tension. Contrary to the solid boundary, the velocity fluctuations parallel to the free surface are relatively unimpeded and Balachandar and Patel (2002) noted a region of constant streamwise turbulent intensity very near the free surface. In a recent review paper by Nezu (2005), the free surface is considered as a “weak wall” which generates quite different patterns of secondary recirculation. All of these effects are attributed to the transfer of energy from the wall-normal component which is suppressed by the free surface.

Despite numerous investigations on the mean flow, there is no general consensus on the behavior of higher order moments of velocity fluctuations even for the simple case of smooth open channel flow. The third-order moments retain the sign (+/-) information and provide useful statistical information on the temporal distribution of the fluctuations around the mean velocity. Contrary to the view that most of the turbulence is confined to a region close to the wall, there is strong evidence that some of it is transported to the outer region by the presence of large coherent structures. Nezu and Nakagawa (1993) have speculated that the bursting motions in the inner layer interact with the large eddies formed in the outer layer. Only the stronger bursting motion near the wall can produce and sustain eddies in the outer region. This hypothesis is supported by the fact that the period of the bursting motion at the wall coincides with the period of the boils formed at the free surface.

In this chapter, information for the lower and higher-order turbulent moments are extracted from the LDV measurements obtained on the smooth bed in open channel. Three different flow depths 0.06 m, 0.08 m and 0.10 m are compared with the available turbulent boundary layer data. Analysis of the higher-order moments combined with the conditional quadrant decomposition are used to further study the effect of the free surface on turbulence in simple case of smooth open channel flow.

3.1. Mean velocity scaling and friction velocity

In what follows, different methods of estimation of u_τ over a smooth wall are compared. The first method is based on the assumption that the velocity distribution follows the universal law of the wall suggested by the Clauser chart method. In Figure III-1a, a typical plot of the mean velocity profiles in inner scaling for three different flow depths are compared with the law of the wall given by Eq. (III.1) with constants A = 2.44 and B = 5.0. All profiles follow the universal law of the wall in the range between $y^+ > 30$ and $y/d < 0.2$. The values of u_τ that provide the best fit to the velocity profiles are shown in Table III–1.

In the outer region of the fully turbulent channel flow, the contribution of the viscous term becomes negligible and the friction velocity can be found by extrapolating the Reynolds shear stress profile asymptotically to the wall by

$$u_\tau^2 = -\overline{uv}\Big|_{at\ \frac{y}{d}=0} \qquad \text{(III.5)}$$

The implication of Eq. (III.5) is that the Reynolds shear stress is distributed linearly across the channel and it can be used to predict the friction velocity. An estimate of the friction velocity was obtained by extrapolating the measured $-\overline{uv}$ profiles to the wall. At y/d = 0.2, a maximum of $-\overline{uv}$ exists for all cases at $Re_\theta > 2{,}000$. The obtained values are listed in Table III–1 and vary by about ± 6% compared to the values obtained by the Clauser method. The error in this method is a combination of the higher level of uncertainty involved in measuring $-\overline{uv}$ as well as the extrapolation errors.

In Figure III-1b the classical Reynolds shear stress distributions of smooth open channel flow are compared with the recent experimental data of both a smooth turbulent boundary layer flow reported by Schultz at el., (2005) at $Re_\theta \approx$ 9,000 and a two-dimensional channel flow reported by Bakken et al., (2005) at $\mathrm{Re}_\tau = u_\tau h / \nu \approx$ 3,300 (*h* is the channel half depth). For consistency, star symbols are used to denote the turbulent boundary layer data set while cross symbols are used to denote the 2-D channel data set in all of the forthcoming figures. The turbulent boundary layer data are scaled with the boundary layer thickness (δ), while the mid depth of the channel is used as a scaling parameter for the 2-D channel. For the open channel flow data the total depth of flow (d) is used as the scaling parameter. The present open channel data are further compared with the large eddy simulation (LES) by Williams (2005) at Re^+ = 171 ($\mathrm{Re}^+ = \frac{u_\tau d}{\nu}$). All velocity profiles are normalized with the shear velocities obtained by the Clauser method (Table III−1). The present smooth open channel data are considerably lower than the turbulent boundary layer data. Poor collapse among the different tests is evident for the entire outer region. Only the data set with the shallow depth (*d* = 0.06 m) agrees well with the two-dimensional channel data as well as the large eddy simulation data in the outer region. For all depths, the open channel data attained maximum of about $-\overline{uv}^+$ = 0.8 at approximately *y/d* = 0.2 which is lower than the maximum value for the turbulent boundary layer data. The present results are consistent with the observation of Tachie et al., (2003) who observed lower values of the Reynolds shear stress for smooth and rough open channel flow compared to the DNS simulation of Spalart (1988). Furthermore, the Reynolds numbers for the smooth open channel data do not vary much and any differences among the $-\overline{uv}$ profiles will be most likely due to the effect of the depth. In Figure III-1b, at a given *y/d*, the Reynolds shear stress distribution increases at shallow depths. The examined open channel profiles are separated in the outer region and they become similar when approaching the maximum at $y/d = 0.2$. It appears that the classical scaling does not absorb the effect of depth even though a similar maximum velocity of 0.5 m/s was used for all experiments. The total shear stress distributions $\tau(y)$ can also be used to determine the shear velocity. By balancing the mean forces, for a fully developed flow in a channel the total shear stress distribution is given by

$$\tau(y) = -\rho\overline{uv} + \mu\frac{dU}{dy} = \rho u_\tau^2\left(1 - \frac{y}{d}\right). \tag{III.6}$$

The total stress was calculated by adding the Reynolds shear stress to the viscous stress. To minimize the error in determining the velocity gradient, the measured mean velocity profiles were numerically smoothed and differentiated. The total shear stress profiles normalized by the local wall shear stress are shown in Figure III-1c. From this graph, it is evident that only the shear distribution for the case of d = 0.06 m closely follows Eq. (III.6) in the outer region. This discrepancy clearly suggests that the depth is important in open channel flow. The values of the shear velocity calculated from the total shear stress distributions are shown in Table III–1. While in the case of shallow depth $d = 0.06$ m, the shear velocity is overestimated by 4%, for the other two cases, the error in the calculated shear velocity is higher (7 ~ 10 %).

One other common method widely used in hydraulic engineering practice described by Chow (1959) uses the slope of the water surface (S_0), the flow depth (d), and the acceleration due to gravity (g) to calculate the shear velocity, i.e., $u_\tau = (gdS_0)^{1/2}$. In Table III–1, the shear velocities calculated by using the slope of the water surface are also shown. This method does not provide a measure of the shear velocity at a specific location, but rather an average value for the entire channel. Compared to the Clauser plot method, the differences in u_τ become larger.

A more accurate method for determining the shear velocity is explored by using the mean velocity information in the outer region. It is worthwhile to note that in this region, more velocity data is generally available with lower measurement uncertainty. In this study, the defect law of the form given by Eq. (III.4) was adapted. In this regard, U_0 is the maximum velocity and δ is replaced by the measured total depth of flow (d) where the maximum velocity is observed.

The values for u_τ and Π are obtained by following the two-parameter optimization procedure described by Tachie (2001), for $y/d > 0.2$. In Table III–1, the optimized values of u_τ and Π are shown. The errors in the shear velocity obtained by the two-parameter optimization procedure is ± 30% for the $d = 0.10$ m, ± 22% for the $d = 0.08$ m and only ±3% for the $d = 0.06$ m compared to the values obtained by the classical Clauser method. Only the value of the wake parameter for the case of $d = 0.06$ m is close to the value of 0.10 reported by Kirkgoz et al., (1997). Negative values of Π are obtained for the other two cases. This is similar to the observations of Cardoso et al., (1989) who also reported negative values of the wake parameter ranging from -0.27 to +0.02. The wake parameter depends strongly on the pressure gradient. Libby (1996) examined in detail the effect of the wake parameter in terms of different pressure gradients. His analysis shows that the deviation from the logarithmic distribution applicable at the outer edge of the boundary layer significantly increases as the adverse pressure gradient becomes stronger. Conversely, in favorable gradients the logarithmic law applies over most of the boundary layer thickness. The negative values of the wake parameters are physically possible for flows with favorable pressure gradients (accelerating flow). In the present experiments, a uniform open channel flow was maintained, and thus the pressure gradient should be very close to zero or slightly favorable. Thus it is expected that the value of the wake parameter will be positive but smaller than the case of a zero pressure gradient turbulent boundary layer. The role of the wake function, $w(\eta)$ in the defect law (as defined in Eq. (III.2) with (η = y/δ) is further examined for two different equations related to the wake function. The wake function defined by Coles (1956) given by

$$w(\eta)_{Coles} = \sin^2(\frac{\pi}{2}\eta) \tag{III.7}$$

is compared to the wake function proposed by Granville (1976) and later implemented by Krogstad et al., (1992)

$$w(\eta)_{Krogstad} = \frac{1}{2\Pi}\left((1+6\Pi)\eta^2 - (1+4\Pi)\eta^3\right) \tag{III.8}$$

The two wake functions are first compared for a zero pressure gradient turbulent boundary layer data of Osterlund (1999) on a smooth surface at Re_θ = 2532. Figure III-2 shows the complete velocity profile in the traditional overlap and outer regions of the flow, but in inner co-ordinates. The turbulent boundary layer profile is compared with the data from the present experiments. All open channel profiles show extended region where the logarithmic law is valid, which implies that the flow in open channels tend to be closer to turbulent boundary layer under favourable pressure gradients.

For the turbulent boundary layer data the wake parameter of Π = 0.55 was obtained by both Eqs. (III.7) and (III.8). However, the Coles wake function becomes invalid when the edge of the boundary layer is approached ($\eta \rightarrow 1$) due to the fact that $\frac{dU}{dy} \neq 0$.

Recently, Guo et al., (2004) proposed a modification for the Coles wake function, which satisfies the zero velocity gradient requirements at the edge of the boundary layer. The wake function given by Eq. (III.8) is a more natural choice because it is derived at the boundary condition where $\frac{dU}{dy} = 0$ at $\eta \rightarrow 1$. Further analysis of the turbulence intensity in the outer region as well as the effect of the free surface is sought.

3.2. Turbulence intensities

Figure III-3 shows the streamwise turbulence intensity ($\overline{u^2}$) for the three depths in outer scaling. The turbulence intensities are normalized by the maximum velocity, U_0. The velocity and length scales are selected in such a way that they refer to directly measured quantities. Thus, any inaccuracies associated with the calculated scaling parameters are minimized. In the subsurface portion of the profiles for the deep flow cases d = 0.10 m and 0.08 m, a clear constant turbulence intensity region exists where $\overline{u^2}/U_0^2 \approx 0.001$. It seems that the portion of constant turbulence tends to widen with increasing depth of flow. For the shallow case d = 0.06 m, the constant turbulence region is very small.

Turbulent flow in open channels contains motions with a broad range of scales. The presence of free surface and the bottom wall creates uneven distribution between the turbulent fluctuations, which leads to anisotropic conditions in the outer region. Because the mean velocity scaling laws are derived under isotropic turbulence, to eliminate or reduce the effect of the free surface, the edge of the boundary layer has been redefined on the basis of the region of constant turbulence intensity. This length scale denoted as δ'

can be interpreted as the largest eddy size in the streamwise direction of the flow. The values of δ', the corresponding u_τ and the wake parameters are computed using this length scale is shown in Table III-2. More accurate values for the shear velocities are obtained by using the new length scale excluding the effect of the free surface. The errors in the calculated friction velocity values for d = 0.10 m and 0.08 m are within ± 2%. The wake parameters are all positive with an average of 0.15. However, the present data indicate a much lower value of Π, albeit positive.

In Figure III–4, the new length scale provides for better collapse of both the Reynolds shear stress and the normalized total shear stress distribution. The graphs in Figure III–4 indicate that any effects arising due to the aspect ratio seems to be better absorbed in this type of scaling. Furthermore the present open channel flow data closely resemble the turbulent boundary layer data.

3.3. Higher order moments

Contributions to the turbulent diffusion in the momentum budget in both directions longitudinal ($Du = \overline{u^2 v}$) and vertical ($Dv = \overline{uv^2}$) are also analyzed at different flow depths. In Figures III–5a and 5b, the distributions of the longitudinal (Du) and vertical (Dv) fluxes normalized by u_τ^3 are shown. The open channel data are once again compared with the recent measurements in a smooth turbulent boundary layer by Schultz et al., (2005) and a two-dimensional channel data by Bakken et al. (2005). The boundary layer data are normalised by the thickness of the boundary layer, the two-dimensional channel is scaled with the channel half-depth and the open channel data are scaled with the total depth of flow.

In open channel flow *Du* is negative similar to the case of the boundary layer. The distributions of the *Dv* are positive and decay in the outer region. Close to the free surface the diffusion becomes negligible. It is observed that the diffusion coefficients in both directions are higher for the case of *d* = 0.06 m. However, poor agreement is noticed between the boundary layer data, the two-dimensional channel data and the open channel data. Both the boundary layer and the two-dimensional channel distributions are consistently higher than the open channel data throughout the depth of flow. Only the data at the shallow depth tends to be closer to the data obtained at the two dimensional channel. Significant improvement of the similarity between the open channel data and the boundary layer data is achieved by applying the modified length scale (Figures III–5c and 5d).

3.4. Conditional quadrant analysis

It is documented (Handler et al., 1993, Rashidi et al., 1990) and should be expected that the turbulence characteristics at the free surface of an open channel flow be different from that near a solid wall. Conditional quadrant analysis is used to study the basic features of the coherent motions in open channel flow and how they are affected by the proximity of the free surface. By sorting the two instantaneous velocity components into different quadrants of the (*u*, *v*) plane, the contribution to the total Reynolds shear stress from different extreme events can be quantified. The most important events are the ejections and sweeps, which occur, in the second and fourth quadrants. Previous studies on smooth wall flows have observed that the ejections are responsible for drawing fluid from the low-speed streaky structures in the viscous sub-layer and transporting it to the outer layer. In contrast, the sweeping (inrush) motions (driven by the continuity considerations) are confined to the wall region. The ejection and sweep motions and their cyclic variations are the most important features of the bursting phenomena identified not only in the open channel flow (Grass, 1971) but also in all types of wall bounded flows (Krogstad et al., 1992).

Our aim here is to apply the quadrant decomposition technique for examining the extent of the coherent motions in the outer region for three different flow depths. At every vertical location, the Reynolds shear stress is calculated and further decomposed as a sum of different events according to the procedure described by Lu and Willmarth, (1973). By using the concept of a hyperbolic hole of size H, defined by $|uv| = Hu_{rms}v_{rms}$, the contribution to $\overline{uv}$ from a particular quadrant can be written as

$$\begin{aligned} &(uv)_{Q_i} = \lim_{T\to\infty}\frac{1}{T}\int_0^T u(t)v(t)I(t)dt \\ &for \quad i = 1\, to\; 4 \end{aligned} \tag{III.9}$$

where, $I(t)$ is a detection function defined so that

$$I(t) = \begin{cases} 1 & when \quad |uv|_Q \geq Hu_{rms}v_{rms} \\ 0 & otherwise \end{cases} \tag{III.10}$$

Here, the velocity vector used to compute $(uv)_{Q_i}$ is assumed to be a function of time only. A parameter H defines a threshold value, which separates the extreme events from the random background turbulence. Another way of defining the percentage contribution from each quadrant can be given as

$$Q_i = (uv)_{Q_i} / (-\overline{uv}) \times 100\% \tag{III.11}$$

where $-\overline{uv}$ is the average contribution at every measurement point.

In Figures III–6a and 6b, contributions by ejections (Q2- events) and sweeps (Q4- events) to the average Reynolds stress for H = 0 are presented. The profiles show that the magnitudes of ejection and sweep events decrease towards the free surface. As expected, the ejection phenomenon is the strongest in the vicinity of the wall, but persist at mid-depth at all flow depths. Furthermore, there is no significant effect of depth on the Q2 and Q4 distributions at the level H = 0. The present open channel data are in fair agreement with the data of the smooth turbulent boundary layer (Schultz et al., 2005) shown as solid lines in Figures III–6a and 6b.

To further examine the strength of the extreme events, the decomposition of the Reynolds shear stress at other threshold values was also undertaken. For example, only the contributions from the events whose amplitude exceeds the threshold value of H = 2 are shown in Figures III–6c and 6d. In these figures, only the contribution from the more energetic eddies is examined while contribution from the small random turbulent fluctuations is filtered out. In this study, H = 2 corresponds to instantaneous Reynolds shear stress producing events stronger than $5.5\overline{uv}$. In the Q4 events the effect of aspect ratio is visible in the mid portion of the flow. As seen in Figures III–6c and 6d, the profiles of the smooth wall boundary layer differ significantly from the values of the open channel flow results. Both ejections and sweeps for the open channel flow are substantially higher. This discrepancy confirms the existence of the violent ejections and sweeps which produce a large portion of the Reynolds shear stress in open channel flow. Even though the Reynolds stress distributions in open channel flow clearly resemble that in a smooth wall turbulent boundary layer as shown in Figure III–4c, there are distinct turbulence features that are revealed only from the high-order analysis. At H = 0, the magnitude of the Q2 and Q4 events of open channel flow was similar or slightly lower than that observed in turbulent boundary layers. The turbulent events observed in H = 2 level can have important implications in mixing, scour and sediment transport.

The percentage contributions to $-\overline{uv}$ from different quadrants measured in the outer region at both threshold levels of H = 0 (solid symbols) and H = 2 (open symbols) are shown in Figure III-7. The data are presented as the percentage contribution to the average, as defined previously by Eq. (III-11). Previous studies have adopted this velocity scaling based on measured quantities as it conveniently avoids any inaccuracy in the selection of scaling variables such as u_τ. In all figures, the open channel data are compared with the results of Krogstad et al. (2005) obtained for two-dimensional channel for H = 0 and shown as a solid line. In the case of two-dimensional channel, δ' represents the half height of the channel.

In Figure III-7a, for H = 0 and 2, the outward interactions are negative throughout the depth and almost constant in the range $0.2 < y/\delta' < 0.5$. Further, there is no distinct effect of the depth that is noticeable in the figures. A decrease in Q1 is observed for $y/\delta' > 0.6$. In the outer region of Figure III-7b, a substantial increase in the ejection activities is evident for all flow depths. In the region close to the free surface the ejections show a local positive stress with values over 200% of the average. Similar observations are reported by Nakagawa and Nezu (1977) for open channel flows. At H = 2, the distribution of Q2 is similar to that at H = 0 with a noticeable downward shift. The effect of the depth on Q3 events, denoted as the inward interactions, is shown in Figure III-7c. The trends are similar to the Q1 events and almost constant contribution to the Reynolds shear stress is observed up to $y/\delta' \approx 0.5$. For $y/\delta' > 0.6$ a negative increase in the Q3 events is noted for all cases. In Figure III-7d, the sweep effects (Q4) are constant at all channel aspect ratios and they start to increase rapidly at y/δ′ = 0.6. Close to the free surface the local value of the Q4 events exceeds the average Reynolds shear stress. The magnitude of Q4 is lower than that at H = 0 and their contribution to the Reynolds shear stress becomes less important. No depth effect on Q1 to Q4 can be noticed in this type of presentation due to magnitude of the scales chosen in the axes. The quadrant analysis comparison between the open channel data and the two-dimensional channel data is shown only for H = 0. In the outer region, the collapse between the open channel data and two dimensional closed channel data is very good. Both types of flows seem to have similar fractional contributions as in smooth turbulent boundary layers at H = 0 when all turbulent events are included.

The number of extreme events (N_Q) above the threshold value of H = 2 is shown in the insets of Figures III–7a - d. While the number of ejections decreases when the free surface is approached, the number of the Q1 and Q3 events tends to increase. However, the relative number of the extreme Q1 and Q3 events is two times smaller than the number of ejections. At H = 2, the following relation exists ejections > sweeps > inward interactions > outward interactions within the range of y/δ′ which is consistent with the observations of Nakagawa and Nezu (1977). Starting at the bed, a sharp reduction of the Q4 events is evident up to y/δ′ < 0.6 suggesting that sweeps are localized close to the wall.

The sign of the streamwise turbulent transport of $\overline{u^2}$ shown in Figure III-8 can be related to turbulent events. Comparison between open channel, turbulent boundary layer (Schultz et al., (2005) and 2-D channel flow (Bakken et al., 2005) are in fair agreement. In all cases, the streamwise turbulent transport of $\overline{u^2}$ is negative which means that most of the turbulent energy is transported away from the location of the maximum turbulent production near the wall. Since ejections and sweeps are significantly stronger they are primarily responsible for the turbulent energy transport and there should be a tendency to attain equilibrium in the Q2-Q4 events. It will be helpful to examine the variation of the ratio Q2/Q4 at the three flow depths.

Figure III-9 shows this ratio at two different threshold values of H = 0 and H = 2.5. The level H = 2.5 is chosen to compare with available data for the two–dimensional channel (Bakken et al., 2001). In all cases, the Q2/Q4 ratios reach maximum around y/δ' = 0.8 and then decreased towards the free surface. The suppression of the depth effect due to the compression of the data noticed earlier in Figures III–7b and 7d is revealed in Figure III-9. For the case of d = 0.06 m, and H = 0 the Q2/Q4 ratio attains a maximum (≈ 1.3) while for the other two cases of d = 0.10 m and 0.08 m the maximum value attained is 1.6. The trend is similar at H = 2.5 as shown in Figure III-9. At H = 0 the Q2/Q4 ratio for a two dimensional channel agrees well with the open channel data at d = 0.10 m and 0.08 m. The maximum is located at $y/\delta' = 0.8$. At higher threshold value of H = 2.5 (which corresponds to contributions only from events that are six times stronger than the $\overline{uv}$) the differences in the turbulence structure for the case of the open channel flow and two-dimensional channel becomes more obvious.

3.5. Anisotropy analysis

In the previous section, analysis of the contributions between Q2 and Q4 events obtained from the conditional quadrant analysis have shown that the flow anisotropy is affected by the presence of the free surface. It was also suggested that the shallow flows tend to be more isotropic than the deep flow cases. In this section, closer examination of the differences between $\overline{u^2}$ and $\overline{v^2}$ components are carried out to further examine the effect of the depth on the components of the Reynolds stress tensor.

3.5.1. Correlation coefficient

Figure III-10 shows the variation of correlation coefficient $\rho_{uv} = -\overline{uv}/(\overline{u^2}\,\overline{v^2})^{1/2}$ at the three depths in smooth open channel flow. The recent data set from Afzal et al., (2009) for depth (*d* = 0.10 m) is also included in Figure III-10. The correlation coefficient has a value of 0.4 at a wall normal location *y/d* = 0.2 for the intermediate and shallow depths (*d* = 0.08 and 0.06 m), while for the largest depth this value is slightly lower. However, the effect of depth is clearly noticeable. In the outer region, ρ_{uv} decreases monotonically for all cases and reaches a minimum near the free surface. As shown in Figure III-10a, at *y/d* > 0.5 the fluctuations are transporting momentum more efficiently at the shallow depth of *d* = 0.06 m. Outside the logarithmic layer (*y/d* > 0.2), the shallow flow indicates a tendency towards lower anisotropy. To reduce the effect of the depth, the new length scale (δ') defined on the basis of a region of constant turbulence intensity close to the free surface is used. When this new length scaling was applied, the effect of depth was relatively absorbed and the data collapsed on to a single line. Furthermore, turbulence distributions, including that of $-\overline{uv}$, and triple correlations, also collapsed onto a single line making them nearly independent of the flow depth. In Figure III-10b, a significant improvement in the similarity and reduction of the depth effect is noticed between the three cases. The present data suggest that the mechanism of energy transfer between the individual components of the turbulent kinetic energy is altered near the free surface at deep flow cases and it might be linked to the secondary currents. One may hypothesize that the appearance of the secondary currents does not solely depend on the aspect ratio or channel geometry but also on the proximity of the free surface.

3.5.2. Reynolds stress anisotropy analysis

Several experimental (Shafi and Antonia 1995, Smalley et al., 2002) and numerical studies (Leonardi et al., 2006) have shown that anisotropy is strongly related not only to the presence of the surface roughness but also to the type of flow. In carrying out such an analysis, previous studies on turbulent boundary layers have suggested the use of the ratio, $\overline{v^2}/\overline{u^2}$. Others have recommended a more detailed analysis which accounts the departure from isotropy by calculating the components of the Reynolds stress anisotropy tensor given by (Lumley, 1978)

$$b_{ij} = \frac{\overline{u_i u_j}}{\overline{u_i u_i}} - \frac{\delta_{ij}}{3} \tag{III.12}$$

Here, $\overline{u_i u_i}$ is twice the turbulent kinetic energy and δ_{ij} is the Kronecker delta function. The b_{ij} tensor is symmetric and the components are bounded by $-1/3 \le b_{ij} \le 2/3$. In the case of isotropic turbulence, $b_{ij} = 0$. The sign of each diagonal component in b_{ij} is a measure of the contribution of each velocity component to the turbulent kinetic energy.

As only the streamwise (u) and the wall normal (v) velocity components are available from the present LDV measurements, the spanwise (w) component need to be modeled. The approximation of the spanwise component was based on the experimental data of Nezu and Nakagawa (1993) on a smooth wall which confirmed that the spanwise stress is proportional to the sum of the other two given by $\frac{\overline{w^2}^{1/2}}{U_0} = C(\frac{\overline{u^2}^{1/2}}{U_0} + \frac{\overline{v^2}^{1/2}}{U_0})$ with a coefficient of proportionality *C*. A value of *C* = 0.40 was used in the present analysis. Smooth open channel flow profiles of the components of b_{ij} are shown in Figure III-11, together with the corresponding components from the DNS calculations of Leonardi et al., (2006) and Handler et al ., (1993). In the outer region ($y/d > 0.2$), the profiles of the anisotropy tensor indicate constant anisotropy levels with increasing distance from the smooth bed. The values of the b_{11} component for the open channel flow show higher anisotropy than the values obtained from the DNS simulations of Leonardi et al., (2006). This is perhaps due to the relatively low Reynolds number of the DNS simulations. Near the free surface, a slight increase in b_{11} is observed which is consistent with the numerical simulations of Handler et al., (1993). While in the DNS simulations of Leonardi et al., (2006), two-dimensional closed channel flow with asymmetric boundary of a smooth and a rough wall was used, in the simulations of Handler at al., (1993) the free surface was explicitly modeled. In the case of the two-dimensional channel flow simulations, the half-depth of the two-dimensional channel was used as outer length scale, while in the open channel flow the depth of flow is adopted as the proper outer length scale. Close to the free surface, the anisotropy of the present LDV data slightly increases as the wall normal component becomes suppressed and energy is distributed between the other two components. A similar effect is also present in the free surface simulation of Handler et al., (1993). This is in contrast to turbulent boundary layers where a reduction of the anisotropy is observed for $y/d > 0.8$ by Smalley et al., (2002). This reduction is due to the influence of the turbulent/non turbulent interface at the edge of the boundary layer. Similar reduction in the anisotropy is also visible from the DNS simulations of Leonardi et al., (2006). The relative magnitude of the anisotropy components (i.e. $|b_{22}| < |b_{11}|$) are consistent with both DNS simulations and shows how sensitive they are to the change of the boundary conditions. In the region $0.2 < y/d < 0.6$, the b_{22} components calculated from LDV data are independent of the wall normal location. The $-b_{12}$ component (equivalent to the Townsend's structure parameter) show reduction throughout the depth. A small flat portion of the $-b_{12} = 0.14$ exists for shallow and intermediate flow depths ($d = 0.06$ m and 0.08m) at $0.2 < y/d < 0.4$. All values of the $-b_{12}$ decrease towards the free surface. As indicated by the above anisotropy analysis, as the flow depth reduces on the smooth bed, the flow tends to become less anisotropic. This result is in line with the previous conditional quadrant analysis.

3.6. Summary

In dealing with the velocity characteristics of smooth open channel flow many of the formulations and empirical relations have been borrowed from the classical turbulent boundary layer theory. It has therefore become a common practice for hydraulic engineers, to use them without further modification. Even though some similarities between the open channel flow and turbulent boundary layer exist, there are important differences in the turbulent structure that need to be recognized. In open channel flow these differences are influenced by the channel geometry and by the free surface. This chapter revisits the velocity scaling in the outer region of smooth open channel flow taking into account the effect of the free surface. As suggested by Nezu (2005), the free surface can be considered as a "weak wall" affecting only the normal turbulent fluctuations and a driving force for the secondary recirculation. A modified length scale is proposed based on the region of constant turbulent intensity. The new length scale provides a better description not only for the mean velocity profiles but also for the Reynolds shear stress profiles. With the use of this new length scale, the estimation of the wake parameter is positive and provides for a more accurate estimate of the friction velocity.

The results from the present quadrant analysis (Figure III-6 and Figure III-7) show that the turbulent structure in the outer region of the open channel is similar to the structure of turbulent boundary layers and two-dimensional closed channels but only for the case of H = 0 where all turbulent events are included. Very different results are obtained at higher threshold values. At H = 2.0, the ejections are spread through most of the depth of flow and they are the major contributor to the Reynolds shear stress. Close to the free surface an increase in Q1 and Q3 events are observed which are responsible for the negative production. Even though the change of flow depth does not show any significant effect on the Reynolds shear stress some interesting differences are revealed by the ratio between Q2 and Q4 events. In the case of the lower depth the distribution of the Q2/Q4 is more spread out and the turbulence energy is more evenly distributed which implies that the turbulence would tend to be more isotropic. At higher depths and lower aspect ratio the conditions become anisotropic which greatly affect the momentum transfer.

The anisotropy results indicate that in shallow smooth open channel flow the turbulence in the outer layer tends to be more isotropic which implies that the turbulent kinetic energy tends to be equally distributed among the three components. In the outer region, an increase of correlation coefficient, show that at shallow depth of d = 0.06 m flow tends to increase the turbulence level compared to the d = 0.10 m which greatly affects the flow resistance.

Table III-1. Calculated friction velocities.

Depth, d (m)	Friction velocity, u_τ (m/s) Clauser Plot	 Reynolds stress	 Total shear stress	 Channel slope	 Defect law	Π
0.06	0.0220	0.0224	0.0211	0.0216	0.0214	0.157
0.08	0.0214	0.0226	0.0229	0.0231	0.0262	-0.097
0.10	0.0212	0.0207	0.0190	0.0243	0.0277	-0.319

Table III-2. New defect law parameters (Krogstad et al., 1992) calculated with a modified length scale δ'.

Depth *d* (m)	Defect law δ'/d	 u_τ (m/s)	 Π
0.06	1.0	0.0214	0.157
0.08	0.80	0.0211	0.195
0.10	0.70	0.0210	0.100

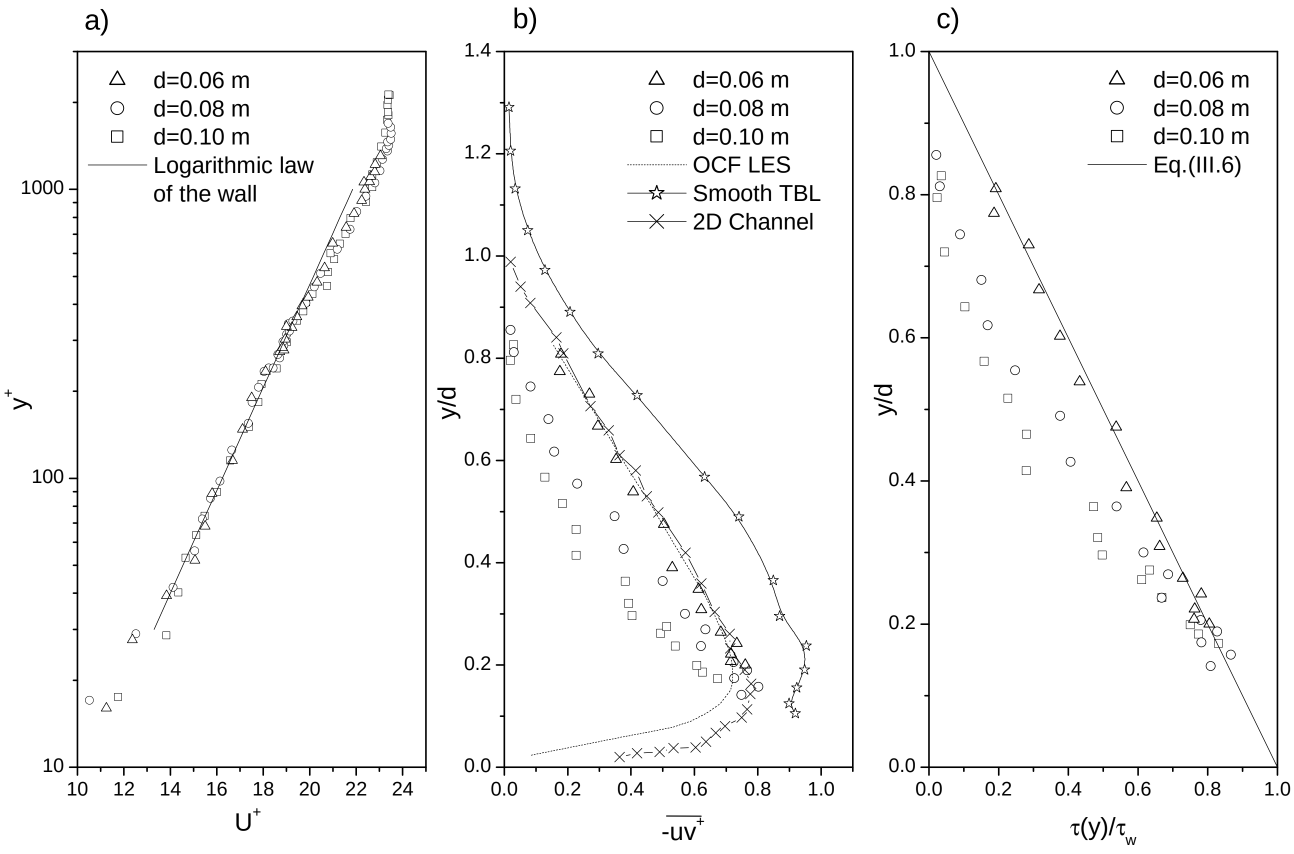

Figure III-1. Determination of the u_τ for smooth OCF; a) Log-law format b) Classical scaling for the Reynolds shear stress profiles and c) Total shear stress distributions.

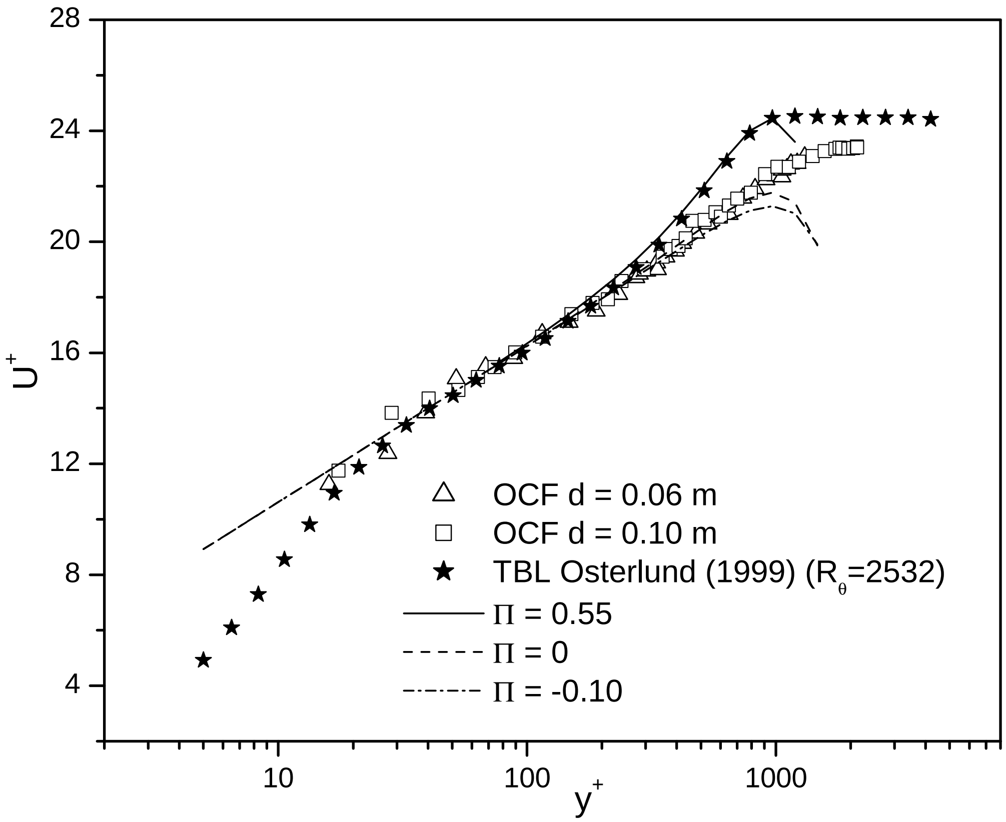

Figure III-2. Velocity defect profiles in inner scaling. Comparison between the wake functions proposed by Coles (1956) (Eq. (III.7)) and Krogstad et al., (1992) (Eq. (III.8).

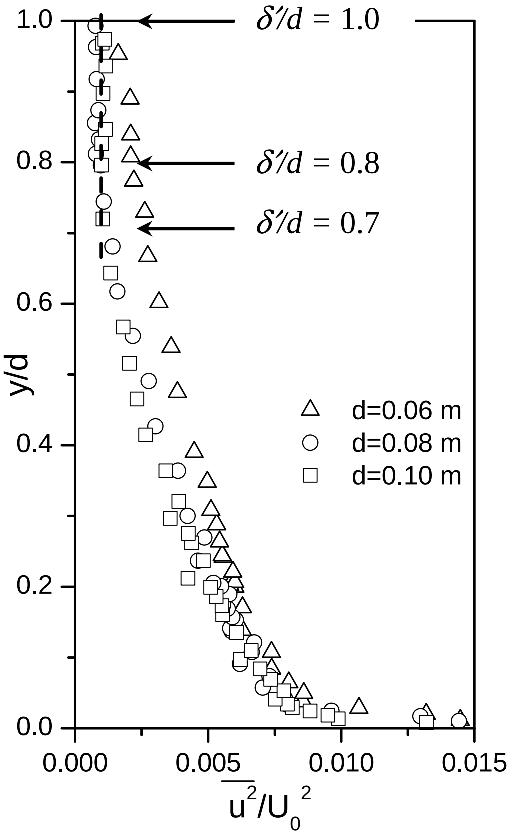

Figure III-3. Outer scaling of the turbulent intensities showing a subsurface region of constant turbulent intensity for *d* = 0.06 m, 0.08 m and 0.10 m.

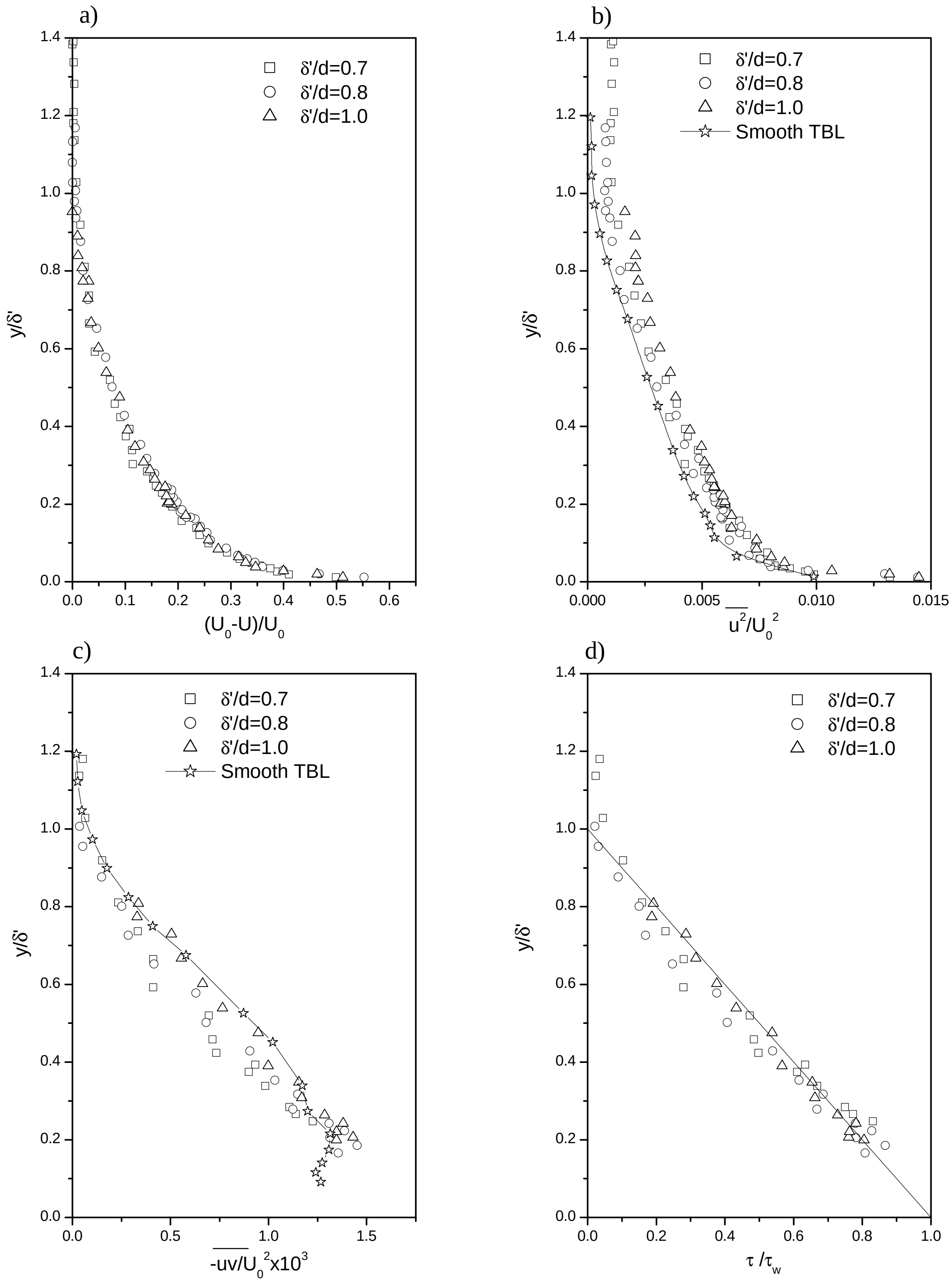

Figure III-4. Improved outer region scaling for various turbulence quantities. Legend as in Figure III-1.

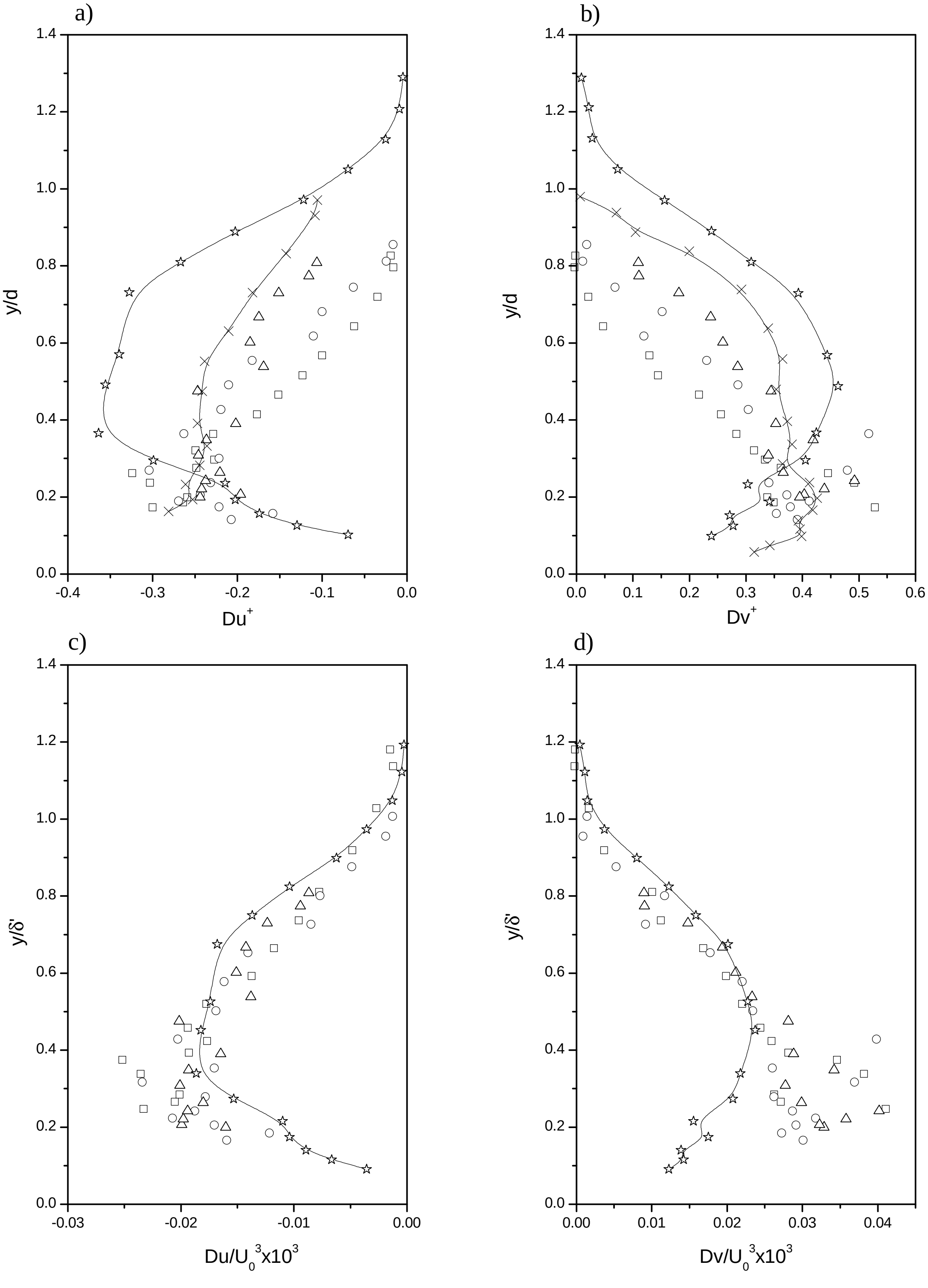

Figure III-5. Inner (a and b) and outer scaling (c and d) of the longitudinal (*Du*) and vertical (*Dv*) turbulent fluxes of shear stress. Symbols as in Figure III-1.

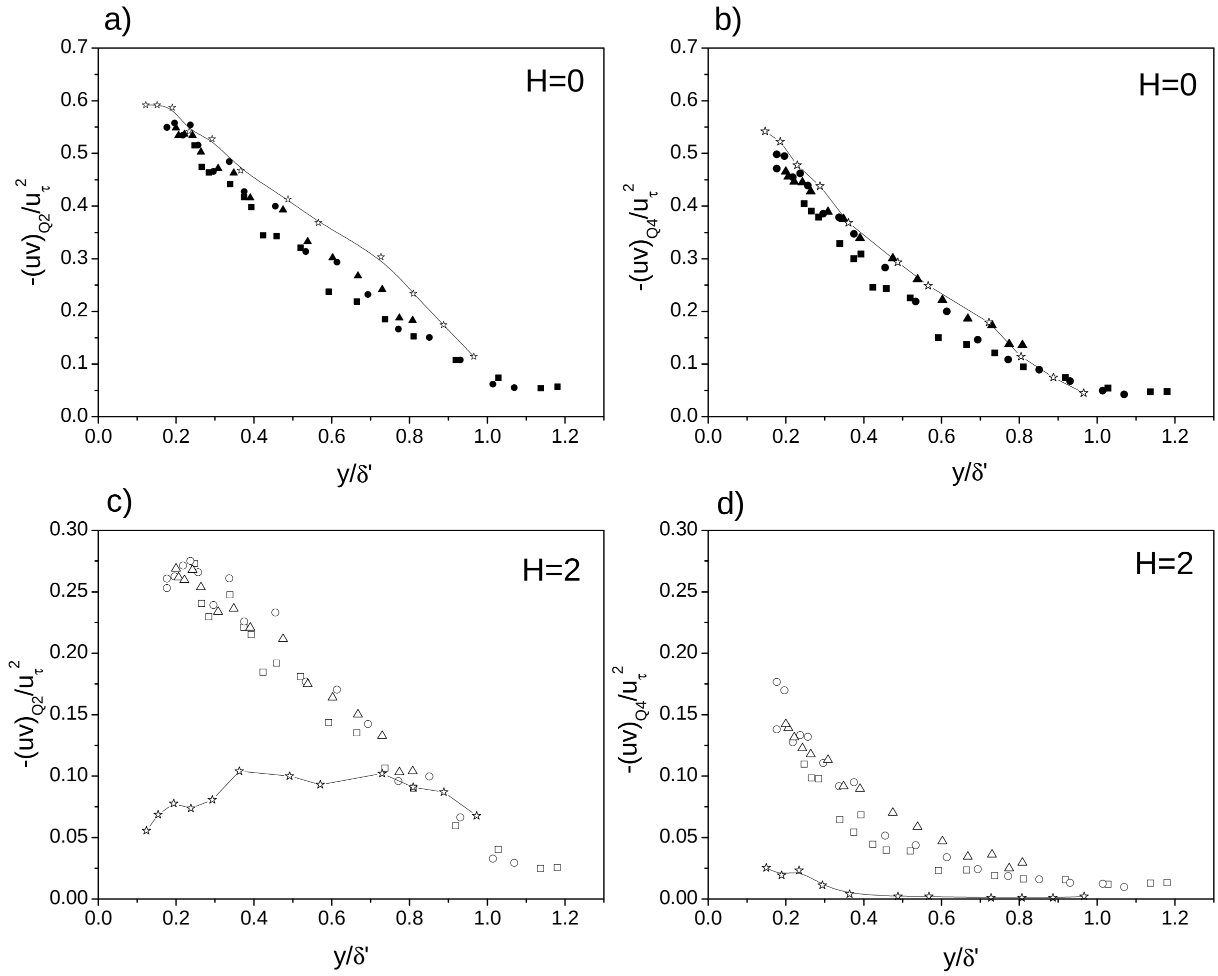

Figure III-6. Comparison between open channel flow and turbulent boundary layer data by Schultz et al., (2005) at H=0 (a) Q2 and (b) Q4 and at H=2 (c) Q2 and (d) Q4. Symbols as in Figure III-1.

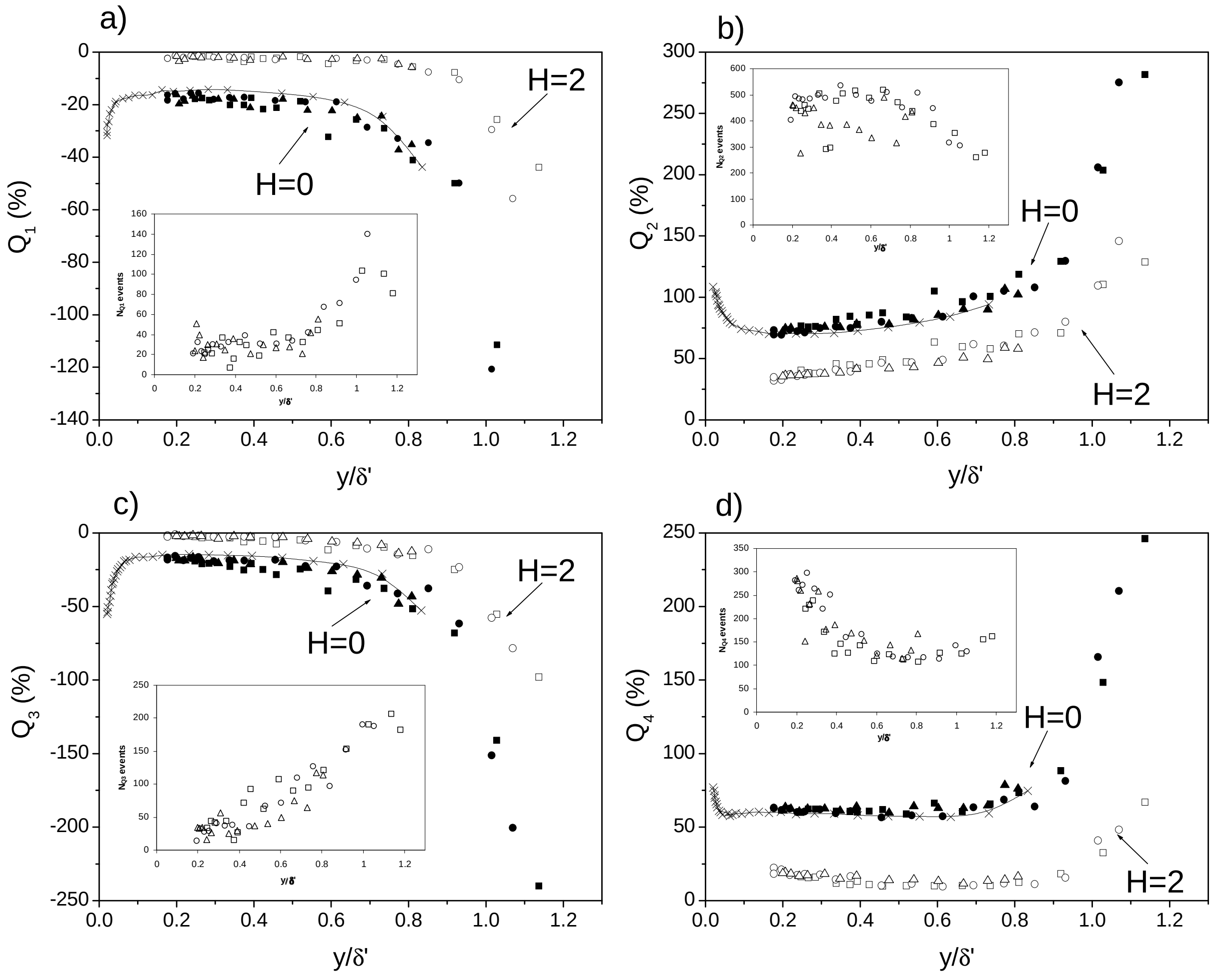

Figure III-7. Comparison between open channel flow and 2-D channel data by Krogstad et al., (2005) (a) Q1 (b) Q2 (c) Q3 (d) Q4. Symbols as in Figure III-1.

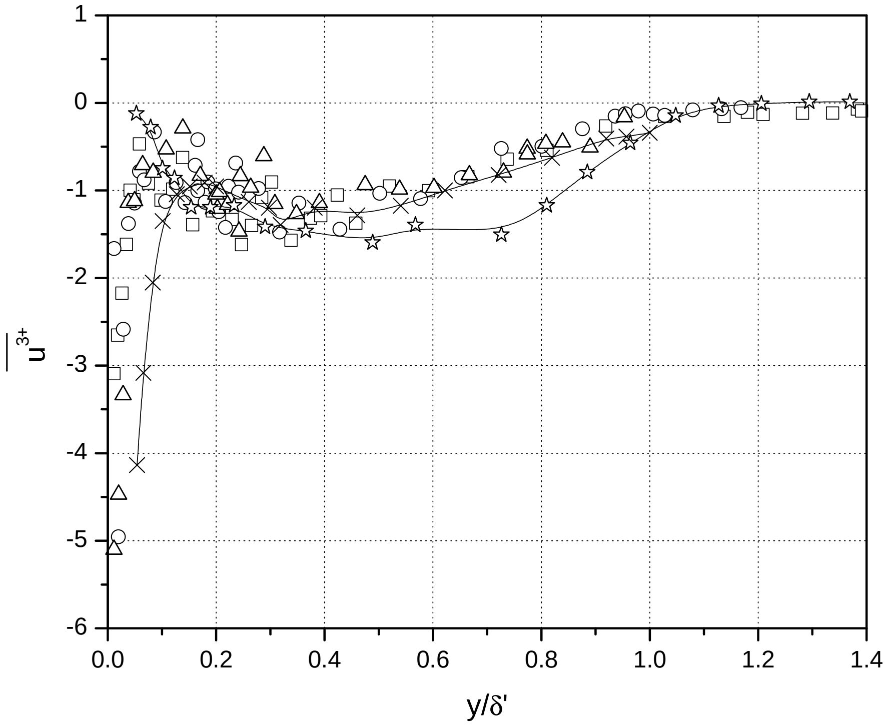

Figure III-8. Distributions of the third order moments ($\overline{u^{3+}}$) in open channel flow, turbulent boundary layer (Schultz et al., 2005) and two-dimensional channel (Bakken et al., 2005a). Symbols as in Figure III-1.

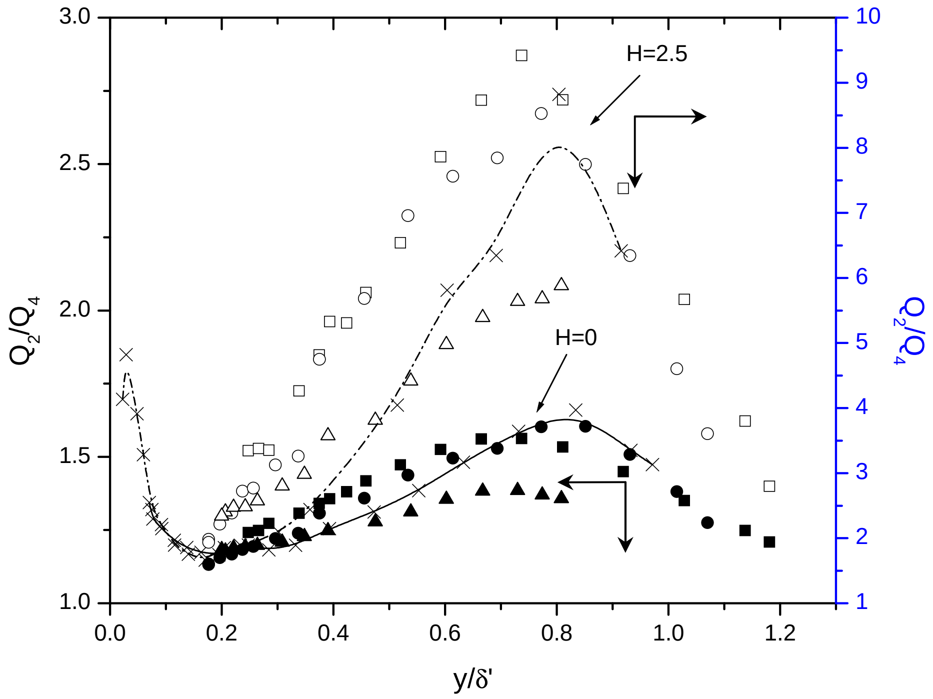

Figure III-9. Ratio between Q2 and Q4 contributions in outer variables at H = 0 and H = 2.5 of open channel flow and two-dimensional channel (Bakken et al., 2001). Symbols as in Figure III-1.

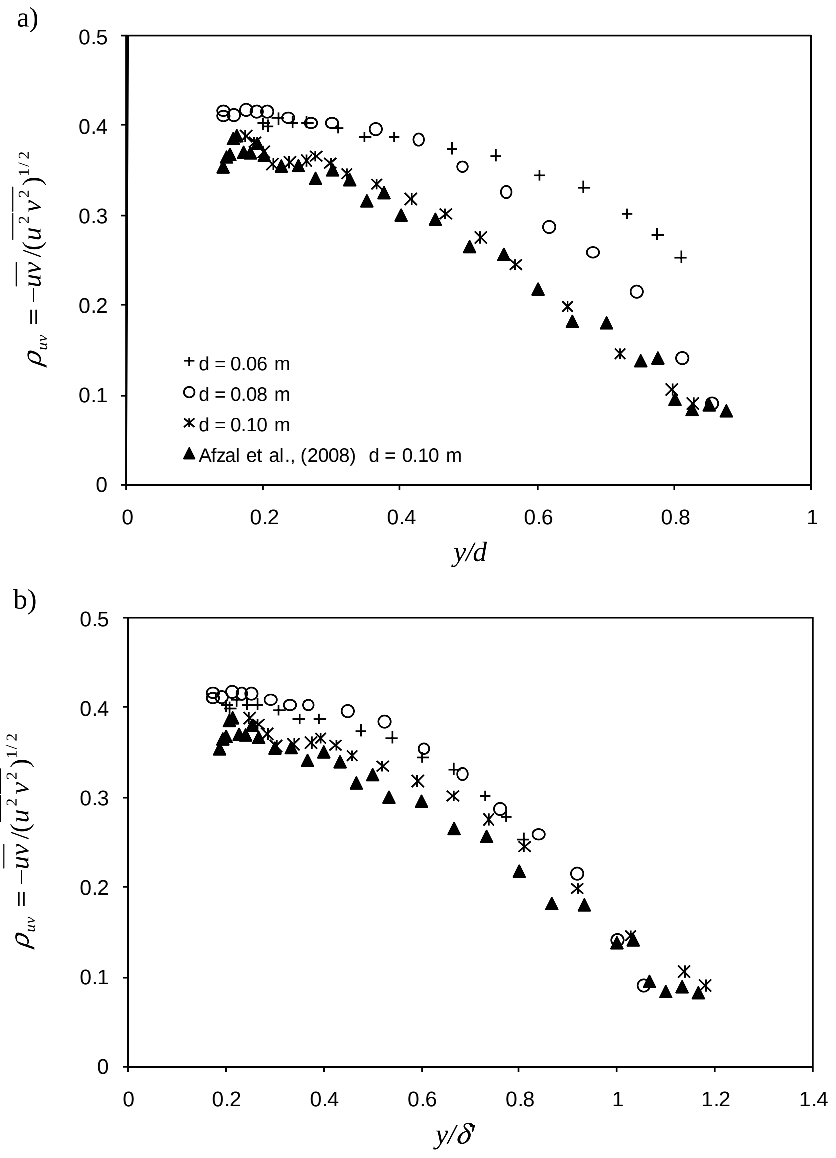

Figure III-10. Coefficients of correlation, ρ_{uv} for the smooth open channel flow at three different flow depths of *d* = 0.06 m, 0.08 m and 0.10 m. Improved scaling is shown in (b).

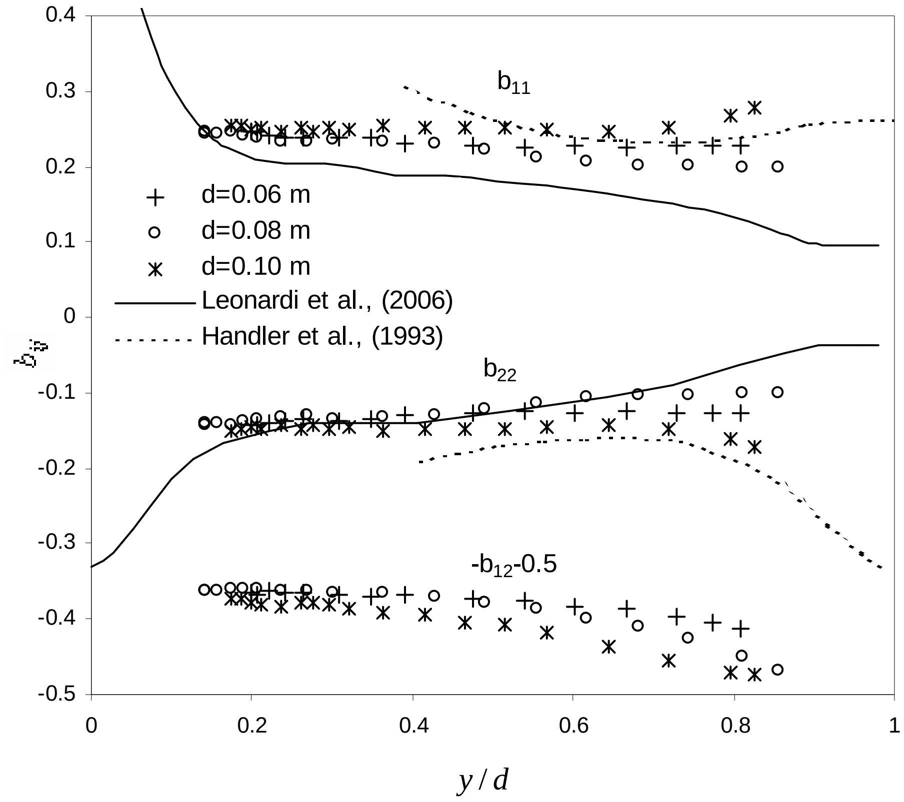

Figure III-11. Components of the b_{ij} for the smooth open channel flow at three different flow depths 0.06 m, 0.08 m and 0.10 m. Solid lines denote the DNS simulations of Leonardi et al., (2006) on the smooth wall while dash lines denote the free surface simulations of Handler et al., (1993).

CHAPTER

IV. TURBULENT STRUCTURES IN SMOOTH OPEN CHANNEL FLOW

This chapter deals with particle image velocimetry (PIV) measurements in the streamwise-wall normal (*x*-*y*) plane in a smooth open channel flow. The Reynolds number of the flow based on the flow depth and maximum velocity (U_0 = 0.18 m/s) was 21,000. The 2-D instantaneous velocity fields are analyzed using proper orthogonal decomposition (POD) to expose the vortical structures. To this end, a brief description of POD technique and analysis of the reconstructed velocity fields using different combination of POD modes is presented. The POD modes used for velocity reconstruction are selected in such a way to expose both the large-scale and the small-scale structures present in the flow. The first set of POD modes recovers 50% of the turbulent kinetic energy while the second set of modes recovers 33% of the kinetic energy. The POD results are further combined with the results from the swirling strength analysis, momentum analysis as well as with conditional quadrant analysis performed at three different threshold levels.

4.1. Proper Orthogonal Decomposition (POD)

Proper orthogonal decomposition is an efficient mathematical tool for defining a suitable set of basis functions for an ensemble of data. Of particular interest in the present application of POD is its capability to separate the most-dominant (large) and the small-scale features of the flow from an infinite-dimensional process with only few modes. This technique is also relevant for studying inhomogeneous turbulent flow fields.

4.1.1. Theory

It is recognized that not all turbulent scales contribute to the same degree in determining the statistical properties of the flow. Methods can be applied to extract from a turbulent-flow database only the relevant information for the physical understanding of a turbulent phenomenon, i.e., to separate the effects of appropriately defined modes of the flow from the background flow or to extract the coherent structures of turbulence, irrespective of the definition of the coherent structure adopted. A powerful technique for the eduction of the coherent structures of turbulent flows is the proper orthogonal decomposition (POD). The ultimate goal of the POD analysis is to determine the best approximation of the given instantaneous turbulent velocity field $u(x,t)$, in terms of N deterministic spatial POD modes $\phi_i(x)$, $i = 1,..,N$ and N random temporal functions $a_i(t)$, $i = 1,..,N$. Mathematically, this problem can be expressed as

$$\min \int_{\Omega}\int_{T} \left\{ u(x,t) - \sum_{i=1}^{N} a_i(t)\phi_j(x) \right\}^2 dtdx \tag{IV.1}$$

Here, the integrations are over the spatial domain, Ω, and time interval T. Arbitrary variations of the unknowns $\phi_i(x)$ and $a_i(t)$ lead to

$$\int_T (u - \sum_j a_j\phi_j)a_i dt = 0 = \int_\Omega (u - \sum_j a_j\phi_j)\phi_i dx. \tag{IV.2}$$

Assuming orthogonality of $\phi_i(x)$ and $a_i(t)$ in meaning that $\int_T a_i a_j dt = 0 = \int_\Omega \phi_i\phi_j dx \ \ for\ i \neq j$, Eq. (IV-2) can be simplified as

$$\phi_i(x) = \frac{\int_T u a_i dt}{\int_T a_i^2 dt} \tag{IV.3}$$

and

$$a_i(t) = \frac{\int_\Omega u\phi_i dx}{\int_\Omega \phi_i^2 dx} \tag{IV.4}$$

Substituting Eq. (IV.3) into Eq. (IV-4) and Eq. (IV.4) into Eq. (IV-3) yields two eigenvalue problems with positive definite Hermitian kernels of the form

$$\lambda_i\phi_i(x) = \int_\Omega \left(\int_T u(x,t)u(x',t)dt \right) \phi_i(x')dx' \tag{IV.5}$$

and

$$\lambda_i a_i(t) = \int_T \left(\int_\Omega u(x,t)u(x,t')dx \right) a_i(t')dt' \tag{IV.6}$$

Equation (IV.5) shows that the spatial POD modes, $\phi_i(x)$, represent the eigenfunctions of the integral operator with the temporal auto-correlation of $u(x,t)$ as a kernel. Similarly, Eq. (IV.6) shows that the temporal coefficients, $a_i(t)$, are eigenfunctions of the integral operator with the spatial auto-correlation of $u(x,t)$ as a kernel. Both equations are equivalent to solving the POD modes $\phi_i(x)$ and coefficients $a_i(t)$. The classical realization of the POD first introduced by Lumley (1967) utilizes Eq. (IV.5) while snapshot POD used in this study, first suggested by Sirovich (1987), employs Eq. (IV.6).

The above eigenvalue problems are Fredholm integral equations of the second kind whose properties are given by the Hilbert-Schmidt theorem. According to this theorem if the eigenfunctions are orthogonal they are also solutions of Eq. (IV.1). In addition, the Hilbert-Schmidt theorem states that the eigenvalues λ_i are real and positive and form a decreasing, convergent series. The instantaneous velocity field $u(x, t)$ can therefore be fully reconstructed from the eigenfunctions when $N \to \infty$. It should be noted that the eigenfunctions are usually normalized such that spatial POD modes are ortho-normal and the coefficients $a_i(t)$ are square root of the eigenvalues. In this chapter the POD analysis is performed on the fluctuating velocity fields, meaning that the i^{th} eigenvalue, λ_i, represent the turbulent kinetic energy contribution of the i^{th} POD mode ϕ_i, and the fractional contribution of i^{th} POD mode to the total turbulent kinetic energy, k_i, can be expressed as $k_i = \frac{\lambda_i}{k}$, where $k = \sum_{i=1}^{N} \lambda_i$ is twice the total turbulent kinetic energy of the flow. It can be shown that POD modes are optimal in the sense that, for a given number of modes N, the projection on the subspace spanned by the N leading POD eigenfinctions contains the largest turbulent kinetic energy on average compared to any set of basis functions (Cordier and Bergmann, 2002). Finally, a reconstruction of any given instantaneous fluctuating field at t_n using the leading K POD modes can be calculated by

$$u(x,t_n) \approx u_L(x,t_n) = \sum_{k=1}^{K} a_k(t_n)\phi_k(x). \tag{IV.7}$$

The physical meaning of the dominant POD modes has been related by Holmes et al., (1996) to coherent structures. PIV measurement provides velocity fields $u^{n,m}$ at discrete points x^n and at time interval t^m. Let N_g be the total number of grid points within a velocity field and M be a total number of velocity fields in a given ensemble. Because of the discrete nature of the spatial velocity fields as well as their acquisition, the POD analysis described above must be discretized, meaning that the spatial and temporal integrations must become summations over n and m. As a result, the discretized versions of the eigen-problem given in Eqs. (IV.3) and (IV.4) become matrix eigenvalue problems. For two-component velocity fields (u, v) as the case for the streamwise–wall normal PIV measurements presented herein, the spatial POD modes are also vectors given by (ϕ_u, ϕ_v) and the discretized version of Eq (IV.5) can be expressed in matrix form as:

$$\lambda_i \begin{bmatrix} \phi_{u,i}^1 \\ \dots \\ \phi_{u,i}^{N_g} \\ \phi_{v,i}^1 \\ \dots \\ \phi_{v,i}^{N_g} \end{bmatrix} = C \begin{bmatrix} \phi_{u,i}^1 \\ \dots \\ \phi_{u,i}^{N_g} \\ \phi_{v,i}^1 \\ \dots \\ \phi_{v,i}^{N_g} \end{bmatrix}, \tag{IV.8}$$

where, $C = \begin{bmatrix} R_{uu}^{n,n'} & R_{uv}^{n,n'} \\ R_{vu}^{n,n'} & R_{vv}^{n,n'} \end{bmatrix}$, and $R_{\alpha,\beta}^{n,n'} = \sum_{m=1}^{M} \begin{bmatrix} \alpha^{1,m}\beta^{1,m} & \dots & \alpha^{1,m}\beta^{N_g,m} \\ \dots & & \dots \\ \alpha^{N_g,m}\beta^{1,m} & \dots & \alpha^{N_g,m}\beta^{N_g,m} \end{bmatrix}$. Thus the POD modes and eigenvalues are the eigenvectors and eigenvalues of the symmetric positive definite matrix C. Equation (IV.6) can be discretized in a similar manner as

$$\lambda_i \begin{bmatrix} a_i^1 \\ \dots \\ a_i^M \end{bmatrix} = S \begin{bmatrix} a_i^1 \\ \dots \\ a_i^M \end{bmatrix} \tag{IV.9}$$

Here, $S = \begin{bmatrix} q^1 q^1 & \dots & q^1 q^M \\ \dots & & \dots \\ q^M q^1 & \dots & q^M q^M \end{bmatrix}$ and $q^\gamma = \sum_{n=1}^{N_g} \left(\left(u^{n,\gamma}\right)^2 + \left(v^{n,\gamma}\right)^2 \right)$. In this context, the coefficients $a^m{}_i$ and eigenvalues are determined from the diagonalization of the symmetric positive definite matrix S. From this analysis, the POD modes at grid point x^n are computed from Eq. (IV.3) as

$$\phi_{u,i}^n = \frac{\sum_{m=1}^{M} u^{n,m} a_i^m}{\sqrt{\lambda_i}}, \quad \phi_{v,i}^n = \frac{\sum_{m=1}^{M} v^{n,m} a_i^m}{\sqrt{\lambda_i}} \tag{IV.10}$$

From the above analysis, the dimension of the matrix C in classical POD is equal to the number of grid points (≈ 10^5 in the present experiments) while the dimension of the matrix S in a snapshot POD method is equal to the number of the time intervals (or snapshots) in an ensemble ($\approx 10^3$ in the current experiments). Therefore, it is clear that it is more numerically efficient to employ the snapshot POD method to analyze the PIV data rather than to use the classical POD method. Recently, the snapshot method has gained popularity and it has been used to study the most energetic flow structures in turbulent jets, wakes and boundary layers (Shinneeb et al., 2006, Singha et al., 2009, among others).

In the next section, the PIV fields in the (*x*-*y*) plane were analyzed using the snapshot POD technique to reveal the energy-containing structures present in the smooth bed open channel flow.

4.1.2. POD analysis of smooth open channel flow at (*x*-*y*) plane

To illustrate the current PIV data, mean velocity and two examples of the instantaneous velocity fields at time instants t = 17.3 s and 28.3 s are presented in Figure IV-1a-c. Figure IV-1a shows mean velocity profiles obtained by ensemble averaging of 2000 instantaneous PIV velocity fields which conforms to the expected pattern in fully developed turbulent open channel flow. More details regarding the validation of the present PIV data can be found in Appendix A. Note that only every eighth velocity profile is displayed in Figure IV-1a in order to avoid cluttering. The instantaneous velocity fields shown in Figure IV-1b and 1c do not reveal any vortices present in the flow because all motions are hidden by the overlying mean component. These PIV fields will be used in the forthcoming POD analysis. Figure IV-2 presents the energy distributions of the calculated POD modes. The fractional contribution of the first POD mode is 15% and decreases with successively increasing number of the POD modes. While lower-order POD modes are representative of the large-scale energetic motions, higher-order POD modes correspond to the small-scale less energetic motions. The cumulative energy distribution shows that in order to recover 95% of the total kinetic energy the POD reconstruction should include ~300 POD modes. Examples of the POD-reconstructed velocity fields are shown in Figure IV-3 and Figure IV-4. In these figures, the horizontal and vertical axes represent streamwise x and vertical y locations, respectively; and both are normalized by the flow depth, d. The purpose of these figures is to bring forth some interesting features of the turbulent structures in the open channel flow.

Figure IV-3a shows a typical example of a fluctuating velocity field of the instantaneous field shown in Figure IV-1b. This field provides little evidence of the flow structures/events because of the interaction of all flow scales. However, a small vortex (highlighted by a circle) can be seen in this field as well as a typical signature of an ejection (Q2) event in the bottom-left corner of the field (highlighted by a square) where fluid particles are being lifted away from the wall by positive wall-normal fluctuations. Several events can be seen in Figures IV–3b to 3d which show some examples of the POD-reconstructed fluctuating velocity fields. These velocity fields were reconstructed using the first twelve POD modes. Figure IV-3b is a POD reconstruction of the fluctuating velocity field shown in Figure IV-3a. This field shows a relatively large structure close to the bed (highlighted by an ellipse) and is rotating in the clockwise direction. The vortical structure appears to be somewhat elongated in the streamwise direction and inclined towards the wall in the streamwise direction x. This vortical structure induces a relatively strong backward flow which represents the ejection event (labeled Q2) and a forward flow with positive streamwise fluctuations being moved towards the wall which represents the sweep event (labeled Q4). It is believed that this vortical structure represents a cross-section of a conditional eddy. As hypothesized by Adrian (2007), the conditional eddy is a combination of a hairpin eddy and two relatively short counter-rotating quasi-streamwise vortices. This eddy sweeps flow from around the eddy and thrusts it upwards in a strong ejection inboard of the head of the eddy and the legs. The relatively strong ejection flow shown in Figure IV-3b (labeled Q2) supports the occurrence of this phenomenon. Further, the occurrence of local maxima in velocity (shown by the extracted velocity profile at x/d = 0.2) supports Adrian's (2007) observations. This figure also shows that a stagnation line separating the ejection (Q2) and sweep (Q4) events is formed (highlighted by dashed line). This line is inclined to the horizontal axis and makes an angle of about 60°. This inclination angle is somewhat higher than the inclination angle of 45° reported by Adrian (2007). Figure IV-3b also shows a portion of an inclined counter-clockwise rotating vortical structure near the top-right edge of the field-of-view with its center seems to be located farther downstream. This structure causes a relatively strong backward flow near the free surface and a forward flow (combined with the flow from the near-bed structure) in the middle region of the velocity field ($0.3 < y/d < 0.6$). Although this induced backward flow resembles the ejection event from the free surface (that is usually observed near solid walls), it is labeled Q3 in order to be consistent with the coordinate system adopted in this paper.

Figure IV-3c shows another example of large vortical structures in the open channel flow. The size of this structure appears to be larger compared to the previous figure. A strong ejection event (labeled Q2) can also be seen between the structure and the bed with a strong induced flow directed downward (labeled Q4) towards the bed. However, the sweep event that occurs near the bed is barely seen in this example because of the large size of the structure compared to the size of the field-of-view.

A third example of the vortical structures is shown in Figure IV-3d. The identified structure in this field appears to reside closer to the free surface and is elongated in the streamwise direction parallel to the x axis. This counter-clockwise rotating vortical structure induces a relatively strong backward flow above the structure and a forward flow below the structure. Since the existence of a hairpin head and neck is inferred from the local maximum of the flow speed (shown by the extracted velocity profile at $x/d = 0.32$), the strong induced backward flow suggests that this vortical structure represents a cross-section of the head of a hairpin structure with two legs extending upwards. It can be speculated that the free surface behaves like a weak solid wall, consistent with the observations of Nezu and Nakagawa (1993), and the mechanism of generating vortical structures near the free surface seems to be similar to the mechanism near the solid wall (Pan and Banerjee, 1995). Although the mechanism of this induced backward flow resembles the mechanism of the ejection event that is usually observed near solid walls, the backward flow in this case appears to move almost parallel to the free surface with a negligible vertical velocity component (labeled Q2). This behavior suggests that an ejection-like event could occur parallel to the free surface as shown in Figure IV-3d or slightly inclined downward as can be seen in Figure IV-3b (labeled Q3) by the vortical structure that resides near the top-right edge of the field-of-view. This behavior may be attributed to the different inclination angles of the vortical structures in the two examples.

More interesting features can be extracted by POD-reconstruction of the fluctuating velocity fields using POD modes 13 to 100 as shown in Figures IV–4a and 4b. The turbulent kinetic energy recovered in these fields is 33%. It should be noted that the features exposed by these modes are less energetic compared to the large-scale motion shown in Figure IV-3. Figure IV-4a shows three structures of different rotational sense (highlighted by circles); two counter-rotating structures exist near the bed, and one clockwise rotating structure resides in the mid region of the field-of-view. This field represents a POD reconstruction of the fluctuating velocity field shown in Figure IV-3a. Dark and light gray circles represent positive and negative rotational sense, respectively. This field does not resemble the POD-reconstructed velocity field using the first twelve modes shown in Figure IV-3b. However, it depicts the contribution of the less-energetic structures to the fluctuating velocity field that resembles Figure IV-3a near the solid wall ($y/d < 0.25$) that are not seen in Figure IV-3b.

Another example of the less-energetic vortical structures is shown in Figure IV-4b. This field reveals the existence of five small structures of alternating rotational sense (highlighted by circles). These structures are likely cross-sections of relatively less-energetic hairpin vortices that are known to have different sizes and strengths. The size of these structures increases in the vertical y direction away from the wall. These features conform to the description of hairpin vortex signatures in wall turbulence suggested by Adrian (2007) who argued that a group of hairpin vortices (a packet) may exist within the flow fields of larger packets. The interesting feature of the less-energetic structures is their shape which appear more circular compared to the elliptic shape of the large-scale energetic structures shown in Figure IV-3.

4.1.3. Vortex visualization and statistics

It is difficult to unambiguously define a turbulent eddy based on the definition proposed by Robinson (1991). One difficulty which has been addressed by several authors (Jeong and Hussain 1995, Adrian et al., 2000) is to find a reliable quantitative criterion corresponding to the Robinson eddy definition. Vorticity alone is not a reliable quantity for vortex identification since there is a significant amount of vorticity produced not only by eddy rotation but also by the shear layer developed near the wall. Thus, the problem is to find a criterion that unambiguously distinguishes between vorticity due to rotation and vorticity generated by the local shear layers.

One of the established techniques for vortex detection is based on the calculation of the swirling strength (Christensen and Adrian, 2001). Swirling strength is closely related to vorticity but it can discriminate between vorticity due to shear and vorticity resulting from rotation. The advantage of the swirling strength (λ) is that it is frame independent since it uses the velocity gradient to identify the local swirling motion. It is defined as the imaginary part of the complex eigenvalue of the local velocity gradient tensor (Zhou et al., 1999). The two-dimensional swirl calculated form the instantaneous in-plane velocity components is defined by

$$\begin{vmatrix} \dfrac{\partial u'}{\partial x} - \lambda_{ci} & \dfrac{\partial u'}{\partial y} \\ \dfrac{\partial v'}{\partial x} & \dfrac{\partial v'}{\partial y} - \lambda_{ci} \end{vmatrix} = 0 \qquad \text{(IV.11)}$$

Solutions for λ_{ci} can be obtained

$$\lambda_{ci} = \frac{1}{2}\left(\frac{\partial u'}{\partial x} + \frac{\partial v'}{\partial y}\right) \pm \frac{1}{2}\sqrt{\underbrace{\left(\frac{\partial u'}{\partial x} + \frac{\partial v'}{\partial y}\right)^2}_{b^2} - \underbrace{4\left(\frac{\partial u'}{\partial x}\frac{\partial v'}{\partial y} - \frac{\partial u'}{\partial y}\frac{\partial v'}{\partial x}\right)}_{4ac}} \tag{IV.12}$$

From the solution given in Eq. (IV.12), the swirl is defined as the imaginary part of the solution, in the regions where the solution is complex. In other words,

$$\lambda_{ci} = \frac{1}{2}\sqrt{\left|b^2 - 4ac\right|}\text{, where } 4ac > b^2\text{.} \tag{IV.13}$$

By definition, the unsigned swirling strength λ_{ci} is always ≥ 0, but a sign can be prescribed based of the value of the local vorticity to show the eddy sense of rotation. Thus, $\lambda = \lambda_{ci}\omega_z / |\omega_z|$ is formed to discriminate counter-clockwise rotating vortices ($\lambda > 0$) from the clockwise ones ($\lambda < 0$). According to Wu and Christensen (2006), vortices rotating in the clockwise direction ($\lambda < 0$) were also termed *prograde* while vortices rotating in the counter-clockwise ($\lambda > 0$) were termed *retrograde*. Here, signed swirling strength (or modified swirling strength) will be used in the (*x*-*y*) -plane to provide information for the heads of the hairpin vortices, their location and spatial distribution. In Figure IV–5, a sample of the fluctuating velocity map in the (*x*-*y*) plane is shown. Contours of the swirling strength λ are overlaid to highlight the eddy structures present in the flow. The swirling strength identifies only the location of the vortex cores and does not provide information about the actual size of the existing structures and therefore additional procedures need to be applied to calculate the size of the vortices and their circulation (Γ). In Figure IV–5, several spanwise vortices are identified residing in the region $y/d < 0.4$. The prograde structures appear to outnumber the retrograde structures, which is consistent with observations of Wu and Christensen (2006). These vortices appear aligned in the streamwise direction and form an interface inclined slightly away from the wall over the field-of-view beneath which exists a large-scale region of streamwise momentum deficit. The prograde vortices induce strong ejections of low-speed fluid just below and upstream of their cores and therefore they are consistent with the hairpin vortex signature introduced and developed by Adrian et al., (2000). It appears that near the bed, the prograde vortices associated with the hairpin heads are the most dominant features in the open channel flow which is similar to the turbulent boundary layers. In what follows, a more quantitative presentation of the swirling strength statistics will be made.

In Figure IV–6, the fraction of time with positive ($T_{\lambda+}$), negative ($T_{\lambda-}$) and non-zero ($T_{\lambda\neq0}$) modified swirling strength are shown as a function of *y/d*. These fractions are computed at every grid point of each snapshot and normalized with the total number of snapshots, i.e., 2000. The average swirling strength for every category was also computed. In Figure IV–6, the present results are compared with the recent data of Volino et al., (2007) for the case of a smooth turbulent boundary layer flow. One should note that the vertical locations for the data by Volino et al, (2007) are normalized by the thickness of the boundary layer (δ). The agreement between the two cases is very good near the smooth bed and some deviations are observed in the outer layer. Note that in Figure IV–6, only one profile in the middle of the field-of-view (*x/d* = 0.5) is shown rather than the spatial averaged value presented by Volino et al., (2007). At all locations, the swirling strength at any instant is non-zero 30% of the time. Near the bed, most of the non-zero swirl has a negative sense of rotation which is consistent with the location of the heads of the hairpin vortices. With increasing distance from the wall, the fraction of the negative swirl decreases and the fraction of the positive swirl increases at more-or-less a similar rate. For the turbulent boundary layer, the increase in positive swirl is more gradual in the region $0.15 < y/\delta < 0.55$, while in the open channel, the increase is at a greater rate. Beyond the edge of the boundary layer, at $y/\delta > 1.0$, the flow is characterized with equal probability of prograde and retrograde vortices. An equivalent region in the open channel flow corresponds to the location $y/d > 0.6$. The effect of the depth is clearly visible and less space is available for the detached eddies in open channel flow compared to the case of turbulent boundary layer flow. In open channel, near the free surface, an increase in the number of retrograde vortices is observed. One should note that the vortices with the positive swirl are equivalent to the vortices with the negative swirl in the reference frame of the free surface assuming that the *y*-coordinate is reflected at the free surface. Similar observations have been reported by Wu and Christensen (2006) for the population trends of vortices at the centreline in two-dimensional channel flows. To further examine the effect of the free surface on the vortex distribution, the probability density function (PDF) of the swirling strength is presented in Figure IV‒7. All PDF's are computed for every wall normal location from all 2000 PIV snapshots. The computational process eliminates the values of $\lambda = 0$ (which occurs about 70% of the time), as shown in Figure IV‒6. For comparison, the values of the swirling strength are normalized with u_τ / d. Near the wall, the negative peak of the PDF is larger than the positive which is in agreement with the fractions shown in Figure IV‒6. The shape of the positive and negative PDF's can be approximated by the gamma probability density function. Farther from the wall, at $y/d = 0.4$, the area of the negative PDF become narrower than the area enclosed by the negative PDF at $y/d = 0.1$. This indicates that prograde vortices with different swirling strength populate predominantly near the wall locations. As they grow away from the wall, they might undergo different merging mechanisms (Tomkins and Adrian 2003) attaining an equilibrium size. Above *y/d* = 0.4, the negative peak of the PDF remains unchanged, while the positive peak varies considerably. At *y/d* = 0.6, the two PDF peaks become equal which implies that at this location, vortices with both sense of rotation are equally probable. The influence of the free surface is visible at locations *y/d* = 0.7 where more retrograde vortices (positive sense of rotation) are identified. This number of retrograde vortices is slightly reduced at *y/d* = 0.8, due to the direct influence of the free surface.

4.2. Zones of the uniform momentum

This section illustrates the effect of the large-scale structures on the distribution of the momentum across the flow depth. Open channel flow can be partitioned into large time-varying, irregularly shaped zones with nearly constant streamwise momentum. Streamwise momentum is defined as constant if streamwise fluctuations within a zone are generally small and always less than the change in the momentum between adjacent zones. The zones of the uniform momentum are unsteady regions defined in terms of instantaneous vector field in contrast to the commonly used layers such as the logarithmic layer that are defined in terms of average quantities. The advantage of analysing the zones of the uniform momentum is that it can provide direct evidence for the outer layer organization of the flow into packets of hairpin vortices. Hurther et al., (2007) partitioned the outer layer of the rough open channel into three zones of uniform streamwise momentum following the concept proposed by Adrian et al., (2000). In the latter study it was found that the zones of the uniform momentum in rough bed open channel flow are similar to those found in the turbulent boundary layer experiments by Adrian et al., (2000) suggesting validity of the outer layer organisation concept based on the presence of the hairpin packets. By combining the results from the uniform momentum analysis with that of quadrant analysis, Hurther et al. (2007) was able to identify the possible relationship between the locations of the large-scale structures and the zones of the uniform momentum. In rough bed open channel flow it was observed that different inclination angles separate the large-scale structures in the various zones. For example, in Zone 3, a large inclination angle of about 80° of the stagnation region between the large-scale structures was noted while in Zone 2, a small inclination angle of about 45° was observed. In what follows, analysis of the uniform momentum zones is sought in order to examine the effect of the free surface in smooth bed open channel flow.

A more quantitative proof of the existence of the zones of the uniform momentum can be seen in the histogram of the instantaneous streamwise velocity (*u*) obtained over the entire flow depth, *d*. The probability density histogram of the streamwise velocity found by accumulating the data over the entire area of for the instantaneous realization is shown in Figure IV-8. Zones identified in Figure IV-8 manifest themselves clearly in the form of local maxima of the histogram, each maximum being associated with a relatively narrow distribution of streamwise momentum that occurs in each zone. The maximum velocity at any zone may also be interpreted as the velocity of a single packet of hairpins (Adrian at al., 2000).

In Figure IV-8, the first zone (Zone 1), which represents the most retarded zone, was identified as the beginning of the logarithmic layer where the mean streamwise velocity was about 50% of the maximum time-averaged velocity (U_0). The second zone (Zone 2) which represents the intermediate momentum zone is the largest ($0.2 < y/d < 0.65$), extended into the wake layer with the maximum velocity being about 79% of the U_0. The third zone (Zone 3) ($u/U_0 = 0.95$), filled the rest of the remaining layer near the free surface. It is worth while to notice that near the free surface there is also free surface (FS) influenced zone which in part overlaps with Zone 3. In the FS zone instantaneous velocities are at the same order and higher than U_0. Overlapping of two zones with uniform momentum is not unusual since the field-of-view is only 1d x 1d, and the packets of the hairpin vortices according to Adrian et al. (2000) are much longer. The existence of multiple zones of uniform momentum can be explained with the coexistence of the two hairpin packets: one hairpin packet to occur inside another in the limited field-of-view.

In Figure IV-9, the uniform momentum zones have been denoted by line contours and they are labelled as zones 1, 2 and 3. To visualize the vortices, filled contours of the swirling strength are also included. The prograde vortices are depicted by the shades of blue while the retrograde vortices are depicted by the shades of red. As expected, the momentum lines pass through the centres of the heads of the hairpin vortices. In Figure IV-9, the velocity vectors in Zone 3 are small because their streamwise velocities are nearly equal to $0.95U_0$ while the velocity vectors in Zones 3 and 2 have streamwise components of velocity that are significantly lower than $0.95U_0$. Line contours of the *u*-component in Figure IV-9 provide a direct way of visualizing the zones with the uniform momentum and to validate their boundaries with the velocity vector field.

Similar procedure was adopted to generate color maps of zones of the uniform momentum for the two instantaneous velocity fields shown in Figures IV−1b and 1c.

Figures IV–10a and 10b shows two maps representing the streamwise velocity defect defined as $(u - U_0)/u_\tau$ where U_0 is the maximum time-averaged velocity and u_τ is the friction velocity (= 9.5 mm/s). In these plots, three zones are shown; the black color corresponds to the values of $(u - U_0)/u_\tau$ less than –4, the gray color corresponds to the range from –4 to –1, and the white color indicates values greater than –1. Some interesting observations can be inferred from the uniform momentum zones in these plots. Figures IV–10a and 10b show that the thickness of Zone 1 appears to vary with the streamwise direction, but it never exceeded y/d = 0.2, which roughly represents the upper limit of the logarithmic layer. It is also noticed that contrary to the observation of Hurther et al. (2007), Zone 1 is continuous for all streamwise locations of $0 < x/d < 1$ examined in this study. It should be pointed out that a rough wall was used in the experiments of Hurther et al. (2007).

The momentum analysis results shown in Figures IV–10a and 10b were performed on the same instantaneous velocity fields that were previously analyzed by the POD technique shown in Figures IV–3b and 3d, respectively. Note that Figures IV–10a and 10b are labelled with the flow events (Q2, Q3, and Q4) that were identified in the POD results. Figure IV-10a shows that there is an increase in the fluid momentum in the region $0.75 < x/d < 0.9$ (labeled Q4) as manifested by the thinning of Zone 1 and enlargement of Zone 3. This can be explained by referring to Figure IV-3b which shows a strong forward flow (sweep event Q4) induced by the large-scale eddy (highlighted by an ellipse). This obviously adds momentum to the instantaneous flow field in this region. As well, the relatively thick layers of Zones 1 and 2 in the streamwise region $0.05 < x/d < 0.7$ may be explained by the same eddy that induces a relatively strong backward flow which retards the instantaneous streamwise velocity in that region. Similarly, the fluid flow was also retarded near the free surface (labeled Q3) by the structure shown in the top-right corner of the field-of-view. The mid region in Figure IV-10a (labeled Zone 3) represents the lowest retarded streamwise momentum zone where the instantaneous streamwise velocity is affected by the contributions from the forward flow induced by the two vortical structures shown in Figure IV-3b.

Similarly, the zones of the uniform momentum shown in Figure IV-10b reflect the presence of the large-scale structure identified by the POD shown in Figure IV-3d. At this instant, a strong backward flow with a very small positive wall-normal velocity component (labeled Q2) is induced near the free surface. This strong backward flow retards the upcoming velocity in that region which explains the momentum level (Zone 2) close to the free surface. In addition, Figure IV-10b shows that the lowest retarded zone (Zone 3) coincide with the forward flow induced by the structure in that region as shown in Figure IV-3d. As well, the low momentum levels represented by Zone 1 and Zone 2 close to the bed can be also explained by the backward flow near the bed shown in Figure IV-3d.

The differences between the momentum maps shown in the previous figures clearly highlight the turbulent activities. The role of the turbulent structures in the variation of the uniform momentum zones was explained with the help of the POD results. Accordingly, the POD results will be used in the next section as a reference to assess the performance of the instantaneous quadrant analysis in studying the flow events.

4.3. Conditional quadrant PIV analysis

The POD reconstructed velocity fields have documented existence of the hairpin vortices in the (*x*-*y*) plane of smooth open channel flow. These hairpins travel in groups that create a long uniform momentum zones. Also, individual or groups of angled hairpins are expected to generate large values of instantaneous Reynolds shear stress. Hence, in this chapter a conditional quadrant analysis is adopted to identify regions in which all of these events occur.

Conditional quadrant analysis is a commonly used statistical tool for investigating the Reynolds-stress-producing events in turbulent flows. The method decomposes the Reynolds shear stress outside of the hyperbolic hole region of size H into four distinct Reynolds-stress-producing events based on the quadrant in which they reside on the *u*-*v* plane. These events include outward interactions (Q1), ejections (Q2), inward interactions (Q3) and sweeps (Q4). The extreme events left after filtering with the highest contribution to the mean Reynolds stress ($-\overline{uv}$) are associated with the large coherent structures. In this study, the quadrant analysis was performed on selected instantaneous fluctuating velocity fields obtained by the PIV technique. The present analysis uses the concept of the hyperbolic threshold (H) as described by Lu and Willmarth (1973), where H is defined by $|uv| = Hu_{\mathrm{rms}}v_{\mathrm{rms}}$. Here $|uv|$ represents the absolute product of the fluctuating velocity components *u* and *v* at a certain instant of time *t*, u_{rms} and v_{rms} are the local root-mean-square values and H = 0, 1, or 2. Thus, the $(uv)_Q$ product for a particular quadrant can be calculated from a PIV instantaneous fluctuating velocity field at time *t* by

$$(uv)_{\mathrm{Q}} = u(t, x_i, y_j)v(t, x_i, y_j)I(t, x_i, y_j)\,, \quad i, j = 1, \ldots\ldots, N \tag{IV.1}$$

Here, Q represents the quadrant in the (*u*-*v*) plane (= 1, 2, 3, or 4), *N* is the number of velocity vectors and $I(t, x_i, y_j)$ is a sorting function defined by

$$I(t, x_i, y_j) = \begin{cases} 1 & when \quad |uv|_{\mathrm{Q}} \geq H u_{\mathrm{rms}} v_{\mathrm{rms}} \\ 0 & otherwise \end{cases} \tag{IV.2}$$

The threshold H is used to define the sorting function $I(t, x_i, y_j)$ in order to identify the Reynolds-stress-producing events relative to the product u_{rms} and v_{rms}. The instantaneous product of $(uv)_Q$ is sorted in the (*u*-*v*) plane and plotted as color maps in order to visualize the regions of the four different quadrants. In the case of H > 0, the random small-scale turbulence signals are removed while the extreme events from each quadrant are extracted.

Figure IV-11 and Figure IV-12 show instantaneous color maps of the regions of the ejection, sweep, inward, and outward events. Each figure consists of three plots a), b), and c) corresponding to H = 0, 1 and 2, respectively. In order to discuss the performance of the quadrant analysis in identifying the flow events, the fluctuating velocity fields that were previously analyzed by the POD technique (Figures IV−3a and 3d) are also used for the quadrant analysis.

Figures IV−11a and 12a illustrate the quadrant maps for a threshold H = 0. By comparing these figures with the corresponding POD results shown in Figures IV−3b and 3d, Figures IV−11a and 12a illustrate that four types of events are predicted by the quadrant analysis. In general, the regions of the flow events identified by the quadrant analysis coincide to some extent with the regions of the same events identified by the POD. However, the quadrant analysis results do not distinguish between the strength of the velocity fluctuations. In other words, the color maps of the quadrant results provide only a qualitative description of the four quadrants at this level (H = 0). For instance, the feature that is identified as a sweep event (labeled Q4) in Figure IV-11a not only represents this event which occurred close to the bed, but also the induced flow by the two identified structures as shown in Figure IV-3b. In addition, some spots in the color maps which represent certain events appear to be separated by other events. For example, it can be seen in Figure IV-11a that there are two spots representing Q2 event separated by Q3 event in the region $0.05 < x/d < 0.6$ and $y/d < 0.3$, although Figure IV-3b shows only an ejection event (labeled Q2) in this area. This is because the fluctuating velocity components used for the quadrant analysis include, in addition to large-scale motions, contributions from small-scale structures. Conversely, the flow events identified by POD are based only on the large scale structures that contain ~50% of the turbulent kinetic energy.

To identify the energetic events in the flow, larger thresholds (H = 1 and 2) were used to filter weaker fluctuations and the results are shown in Figures IV–11b, 11c and Figures IV–12b, 12c, respectively. Figure IV-11b still predicts most of the events in the same regions as the POD result (Figure IV-2b) although the spots that represent these events became much smaller. However, the spot that represents the Q2 event in the region $0.4 < x/d < 0.6$ and $0.1 < y/d < 0.25$ is not shown in Figure IV-3b. This difference may be explained with the assistance of Figure IV–4a which shows a strong upward flow occurring due to the presence of the counter-rotating structure (close to the bed). Moreover, the Q4 event identified close to the bed in Figure IV-3b is filtered out in Figure IV-11b except very small uncorrelated spots. This observation raises a question about the capability of this technique to identify the sweep events as the threshold level increases since the sweep events are relatively weaker than the ejection events (Adrian, 2007).

Figure IV-12b shows a spot in the bottom-left corner of the field-of-view which represents the Q4 event ($0.05 < x/d < 0.15$ and $y/d < 0.10$). This event is not seen in the POD results shown in Figure IV-3d. However, it matches the results shown in Figure IV−4b. This observation indicates the capability of the quadrant analysis to predict some events that cannot be revealed by the POD using only the energetic modes.

By increasing the threshold (H = 2) all Reynolds shear stress producing events weaker than $5.5\overline{uv}$ are removed. As the threshold level increases (H = 2), Figures IV−11c and 12c show that most of the shear stress events were filtered out and only few uncorrelated spots are retained. In addition, some of these spots do not necessarily represent the events as identified by POD. For instance, the uncorrelated spots shown in Figure IV-11c that represent the Q4 event (highlighted by an ellipse) are actually the induced flow by the two structures shown in Figure IV-3b. This behaviour may be attributed to the large threshold and the larger energy level of the fluctuating velocity in that region which was boosted by the induction of the two structures.

From the above discussion, quadrant analysis provides useful information for the instantaneous distribution of the extreme events based on the Reynolds shear stress criteria. The Reynolds shear stress events were related to the turbulent structures obtained from POD reconstructed velocity fields. At threshold H = 0, when contributions from all turbulent scales is included, the quadrant analysis are able to identify the same events as POD. By using larger thresholds (H ≥ 2) the location of the Reynolds shear stress events cannot always be linked to the individual POD large-scale structures. The distribution of the Reynolds shear stress is affected from the combined action of different scales. In addition, if the moderate threshold of H = 1 is used; the quadrant analysis results could be contaminated by the small-scale structures.

To discuss the effect of the flow structures on the mean flow, the contribution of each quadrant to the Reynolds shear stress $-\overline{uv}$ is plotted in Figure IV-13. This was done by extracting the quadrant profiles from the PIV data at a streamwise location *x/d* = 0.5. Since the ensemble size of the PIV data is two thousand velocity fields, three adjacent points at each vertical location *(y/d)* from each PIV snapshot were used in the calculation of the quadrant profiles in order to improve the conditional sampling of the extreme events. Thus, a total of 6000 data points were used in calculating the profile extracted from the PIV data while 10,000 data points were used for the LDV data presented in Chapter III. Following the definition of Krogstad et al., (2005), the stress fractional from each quadrant was calculated by

$$\mathrm{Q}_i = (uv)_{\mathrm{Q}_i} / (-\overline{uv}) \times 100\% \qquad \text{(IV.3)}$$

where $-(uv)_{\mathrm{Q}_i}$ is the Reynolds shear stress of a particular quadrant Q_i (i = 1, 2, 3, or 4) calculated by the following equation, and $-\overline{uv}$ represents the total Reynolds stress given by

$$(uv)_{Q_i} = \frac{1}{M}\sum_{j=1}^{M} u(t_j, x_s, y)v(t_j, x_s, y)I(t_j, x_s, y) \qquad \text{(IV.4)}$$

In Figure IV-13, the quadrant profiles of a smooth channel flow obtained from the LDV measurements are also plotted in the same graph for comparison purposes. It can be seen that all stress fractions obtained from the PIV data follow the same trend as the LDV data. The present data are further compared with the data of Krogstad et al., (2005) for the case of a two-dimensional channel flow. All PIV stress fractions for $y/d < 0.3$ agree well with the stress fractions obtained from the LDV experiments and with data by Krogstad et al., (2005). Ejections and sweeps are large contributors to the mean Reynolds shear stress. The inward and outward interactions generate stress fractions with magnitudes three times smaller than those of ejections and sweeps over the wall-normal extent. Farther away from the bed ($y/d > 0.3$), the effect of the free surface becomes more obvious. The increase of all PIV stress fractions is consistent with the LDV data, but differs significantly from the data of Krogstad et al., (2005).

4.4. Summary

PIV measurements have been conducted in a smooth open channel flow at a depth of 0.10 m with a maximum time-averaged streamwise velocity of 0.19 m/s. The corresponding Reynolds number based on flow depth was 21,000. A total of 2000 image pairs are acquired in the middle of the channel at a framing rate of 1.04 Hz. PIV measurements in the (*x*-*y*) plane are analysed with different techniques to study the organized turbulent motions. The techniques chosen for discussion were proper orthogonal decomposition (POD), swirling strength analysis, momentum analysis and conditional quadrant analysis. The POD results revealed the existence of large-scale vortices of different sizes and energy levels. In the outer layer, these large-scale vortices are likely to be signatures of the hairpin packets supporting the concept of Adrian et al., (2000). The shape of the large-scale eddies is elongated and inclined in the streamwise direction which make their identification unreliable with the existing vortex methods since most of the vortex identification algorithms search for a vortices with a circular shape. It was found, that not every POD reconstructed velocity field contains large-scale structure. In fact, large-scale structures were identified only from 50% of the reconstructed POD velocity fields (Modes 1-12). This is a shortcoming of the fixed plane of the PIV measurements which also limits the size of the large-scale eddies. For the current PIV setup, only large eddies that are smaller than the size of the field of view (= 0.1m) can be identified.

Close to the free surface, signatures of hairpin vortices with legs possibly attached upwards towards the free surface were obtained. The presence of these eddies caused the fluid particles to be displaced away from the free surface and into the flow, almost parallel or slightly inclined to the free surface. This observation suggests that the mechanism of generating vortical structures near the free surface seems to be similar to the mechanism near the solid wall. Analysis of the swirling strength revealed that the swirling strength is non-zero 30 % of time and most of the vortices that populate this layer are prograde. Away from the bed, the number of the retrograde vortices increases. In Figure IV‒7, the PDF distributions of the swirling strength show that at y/d = 0.6 there are equal probability for coexistence of prograde and retrograde vortices. Near the free surface, at y/d = 0.7, an increase of the PDF distributions of the swirling strength of the retrograde vortices was observed. This result is similar to the result of Wu and Christensen (2006) who also reported increase of the retrograde vortices at the centreline of the two-dimensional channel flow. This implies that the influence of the free surface at low Reynolds number could be similar to that of the solid wall as observed in two-dimensional channel. The flow depth contracts the outer layer compared to the turbulent boundary layer.

The PIV data revealed patterns of strong ejection and sweep events which are common features in all wall-bounded flows. The distribution of the uniform momentum zones was consistent with the location of the packets of the hairpin vortices. The distribution of the zones of the uniform momentum seems to validate the outer-layer flow organization concept based on the presence of the hairpin vortices. The quadrant analysis applied to the instantaneous PIV velocity field deals directly with the Reynolds shear stress and thus it provide information for the momentum transport. The quadrant analysis provides additional insight for the flow structures and their induced flow which generates the Reynolds stress events (ejections and sweeps). By comparing quadrant analysis with POD reconstructed velocity fields it is concluded that the quadrant analysis does identify several of the important flow features. However, at lower threshold, the quadrant results could be influenced by the small scale/weaker structures while at higher values of the threshold, there is significant loss of information due to the filtering effect.

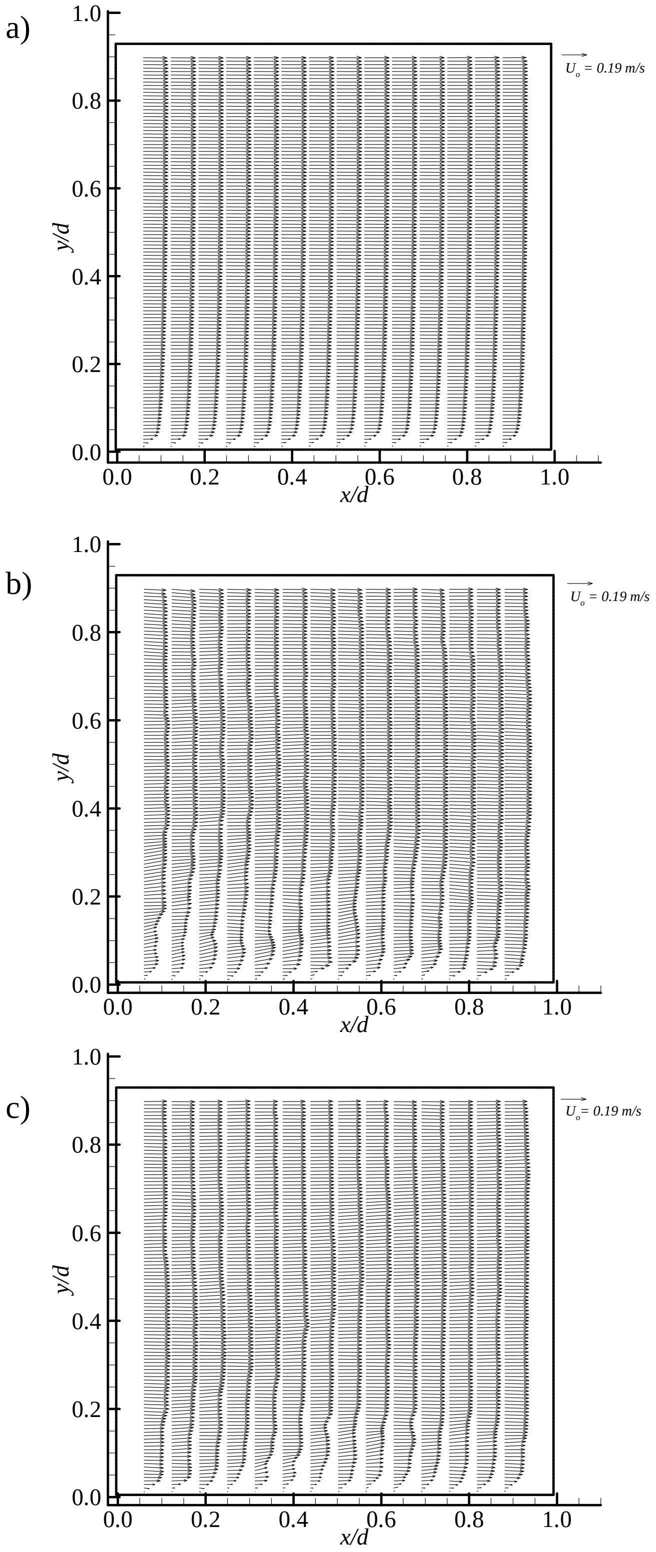

Figure IV-1. Velocity fields of smooth OCF at *d* = 0.10 m a) mean velocity field from 2000 images, b) instantaneous velocity field at *t* = 17.3 s and c) instantaneous velocity field at *t* = 28.1 s. The mean flow direction is from left to right.

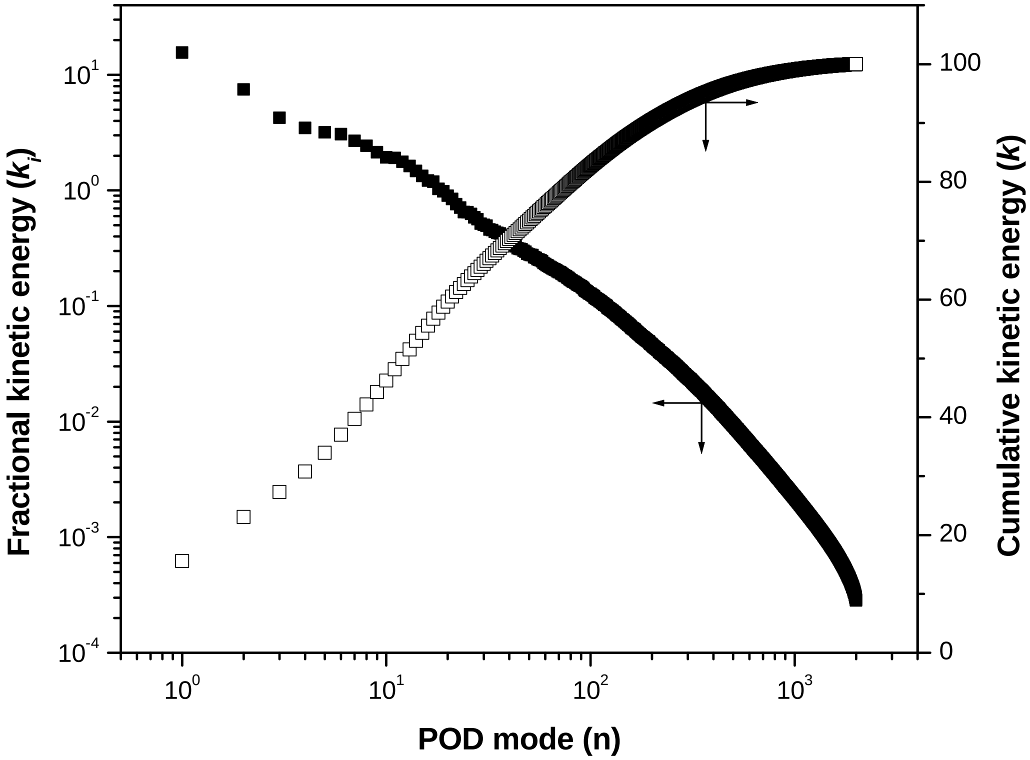

Figure IV-2. POD energy distributions of the smooth open channel flow in the (x-y) palne. Fractional (solid symbols) contribution of each POD mode and cumulative (open symbols) distribution.

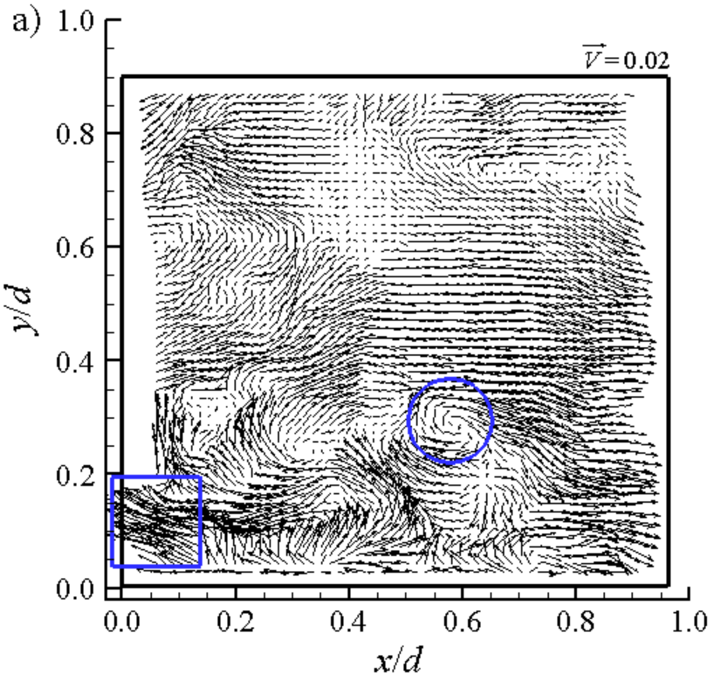
a)
$\vec{V} = 0.02$
y/d
x/d
0.0
0.2
0.4
0.6
0.8
1.0

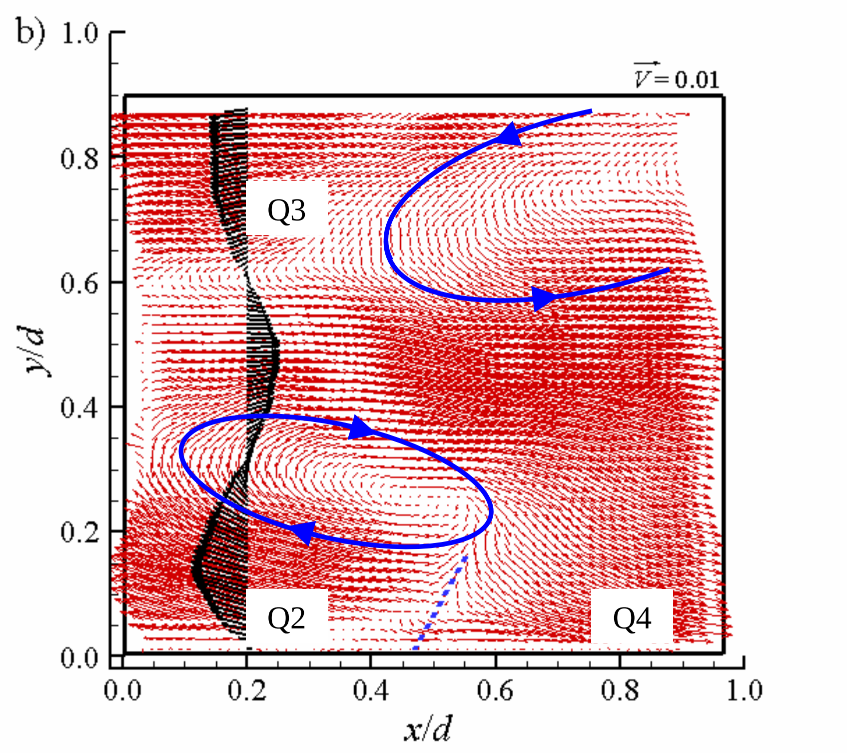
b)
$\vec{V} = 0.01$
Q3
Q2
Q4
y/d
x/d
0.0
0.2
0.4
0.6
0.8
1.0

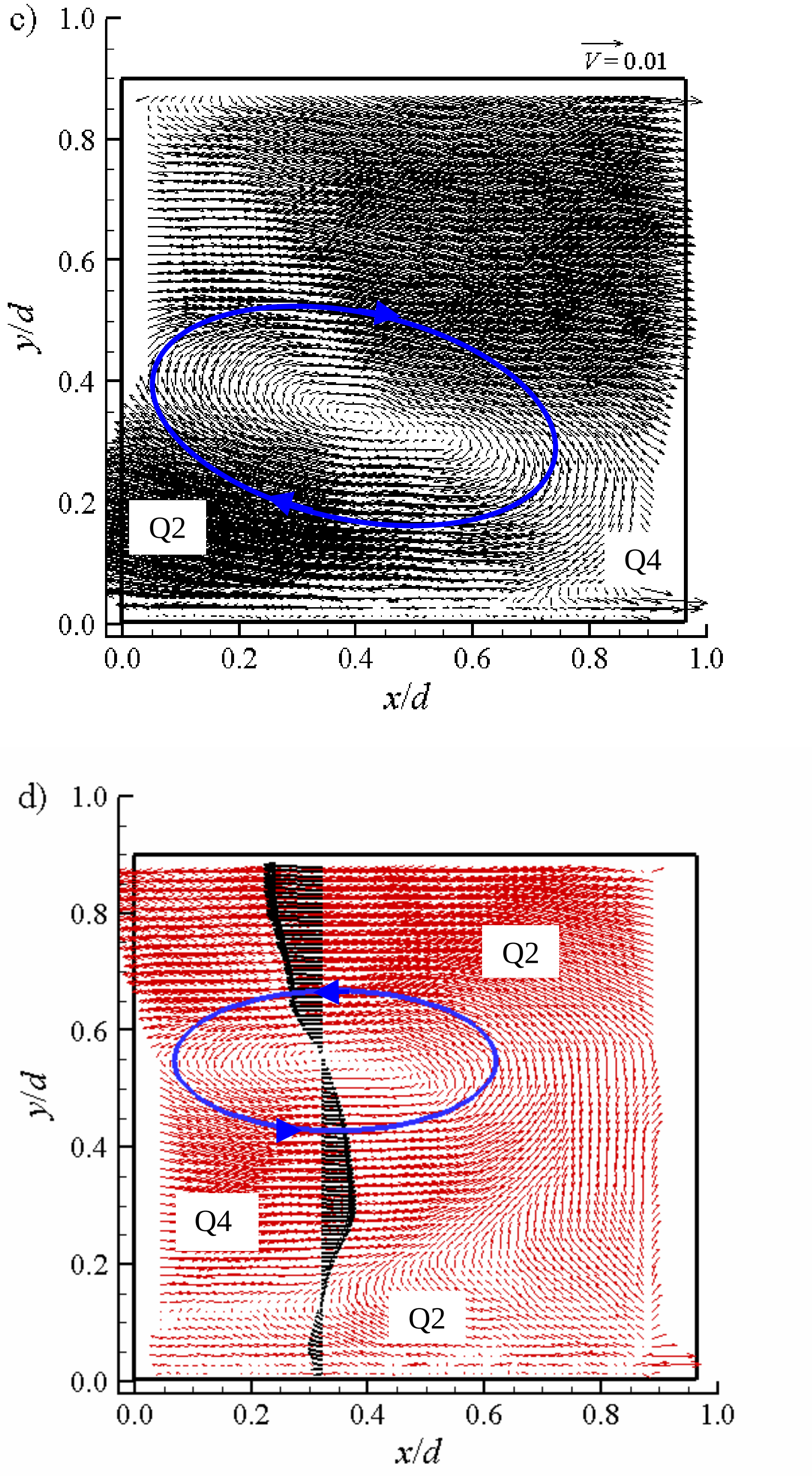

Figure IV-3. Examples of a) a fluctuating velocity field, and b), c), and d) POD-reconstructed fluctuating velocity fields using the first 12 modes. These modes recovered 50% of the turbulent kinetic energy. Note that only every second vector is shown to avoid cluttering.

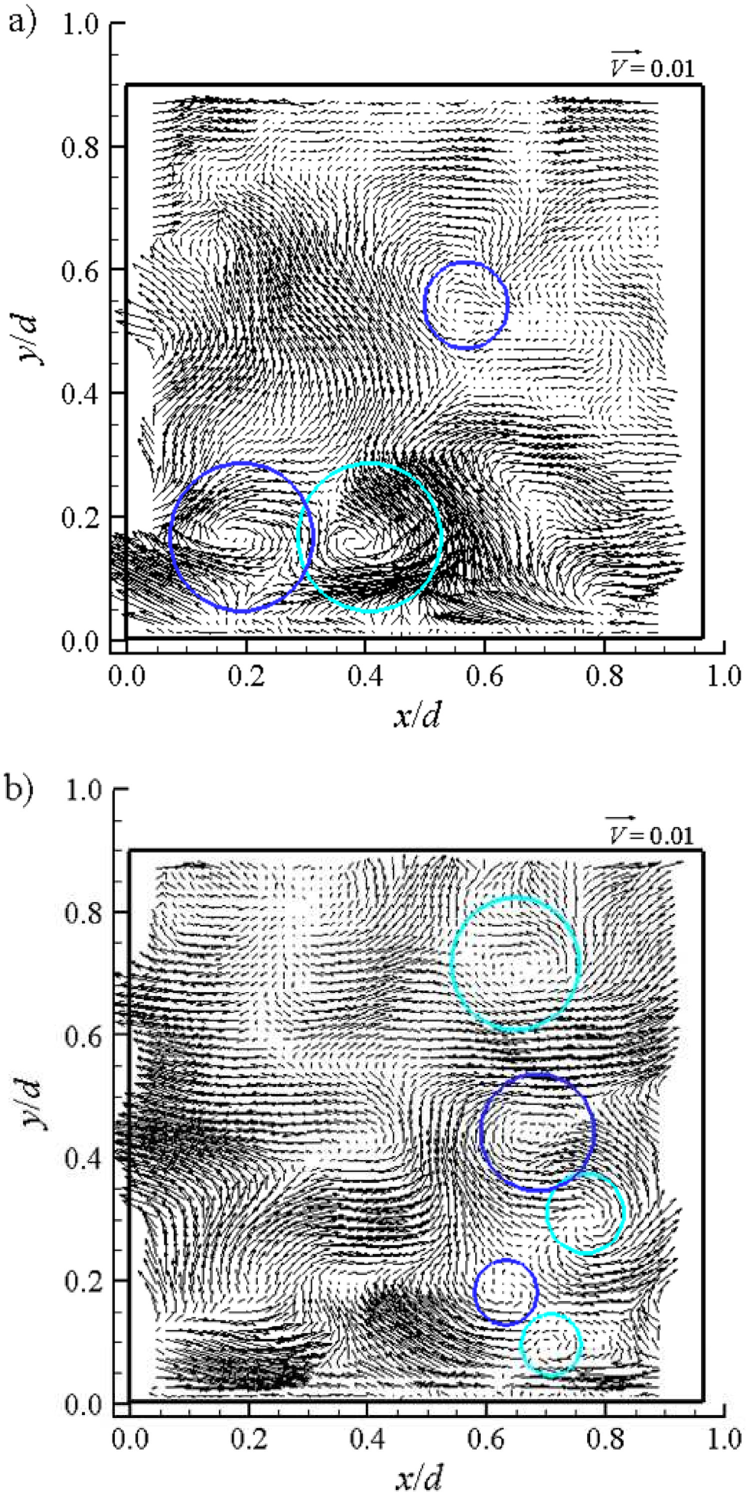

Figure IV-4. Two examples a) and b) of POD-reconstructed fluctuating velocity fields using modes 13 to 100. These modes recovered about 33% of the turbulent kinetic energy. Dark and light grey circles represent positive and negative rotational sense, respectively.

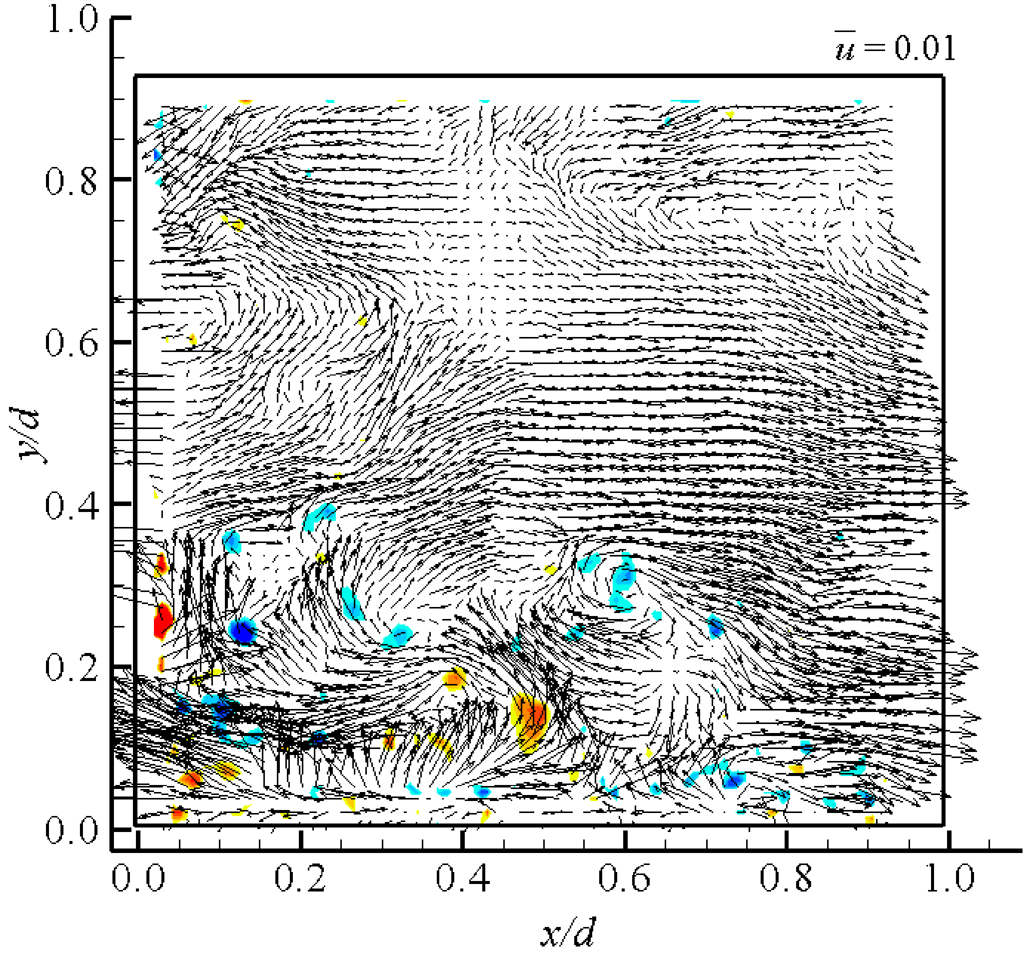

Figure IV-5. Example of the fluctuating velocity field in the (x-y)-plane with positive (retrograde) swirl (red shading) and negative (prograde) swirl (blue shading) superimposed.

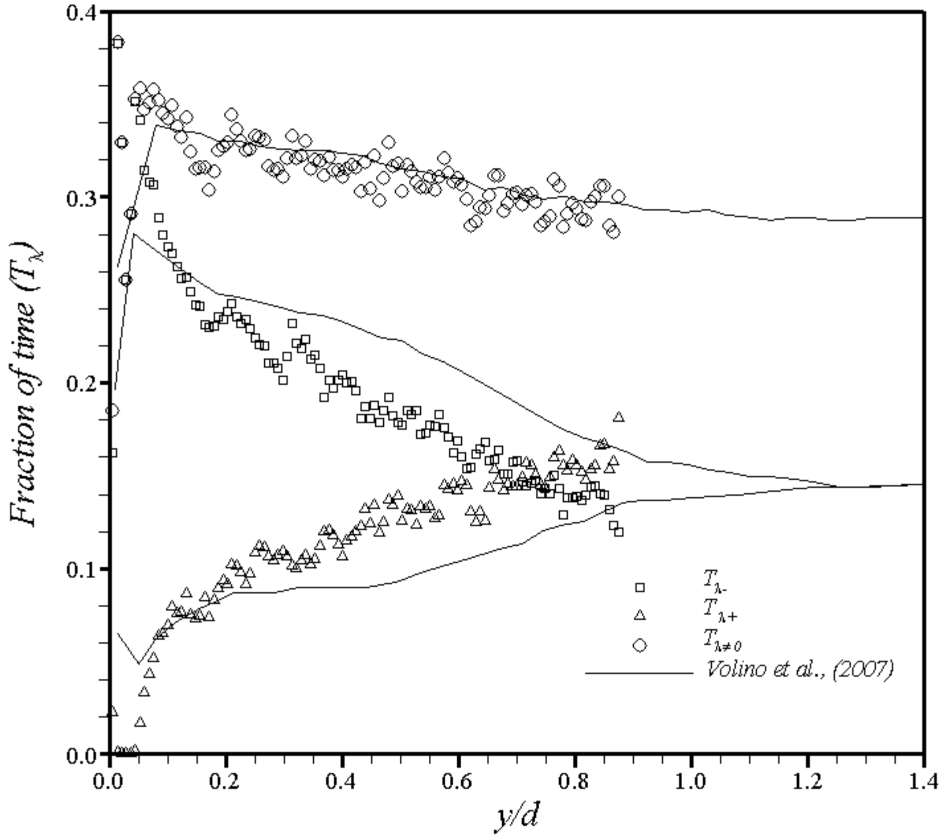

Figure IV-6. Statistics of the swirling strength in the (*x*-*y*) plane showing the fraction of time with positive($T_{\lambda +}$), negative ($T_{\lambda -}$) and non-zero ($T_{\lambda \neq 0}$) swirling strength.

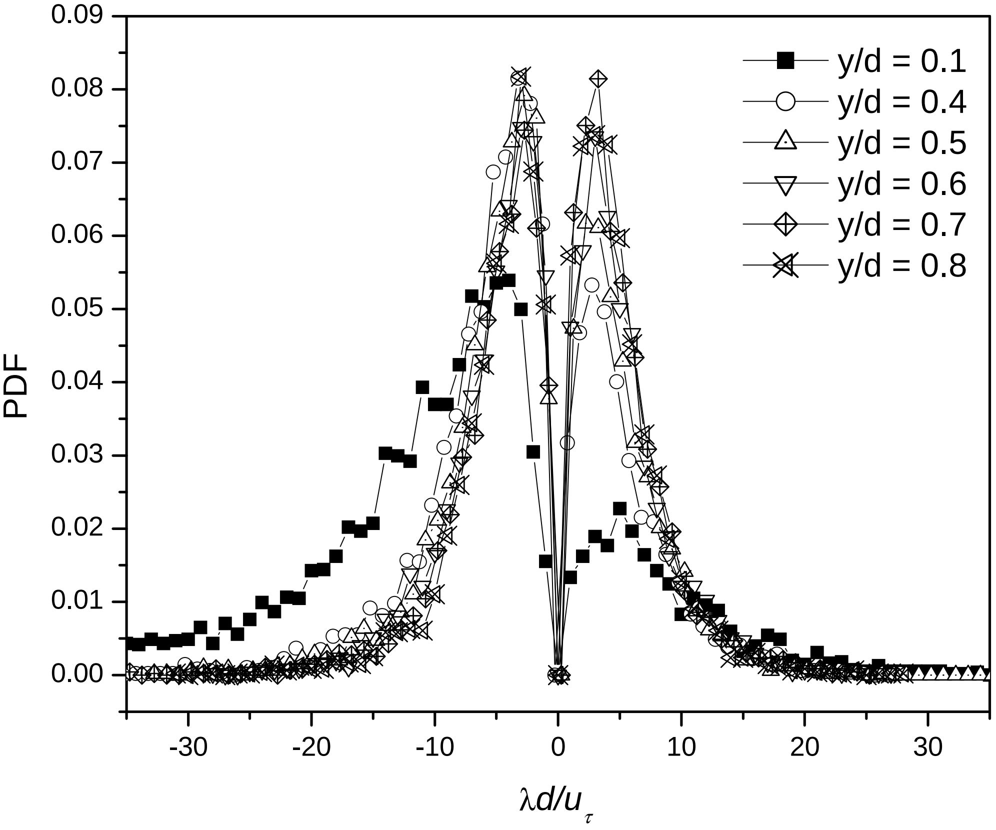

Figure IV-7. Probability density functions of the dimensionless swirling strength in the (x-y) plane at different wall-normal locations.

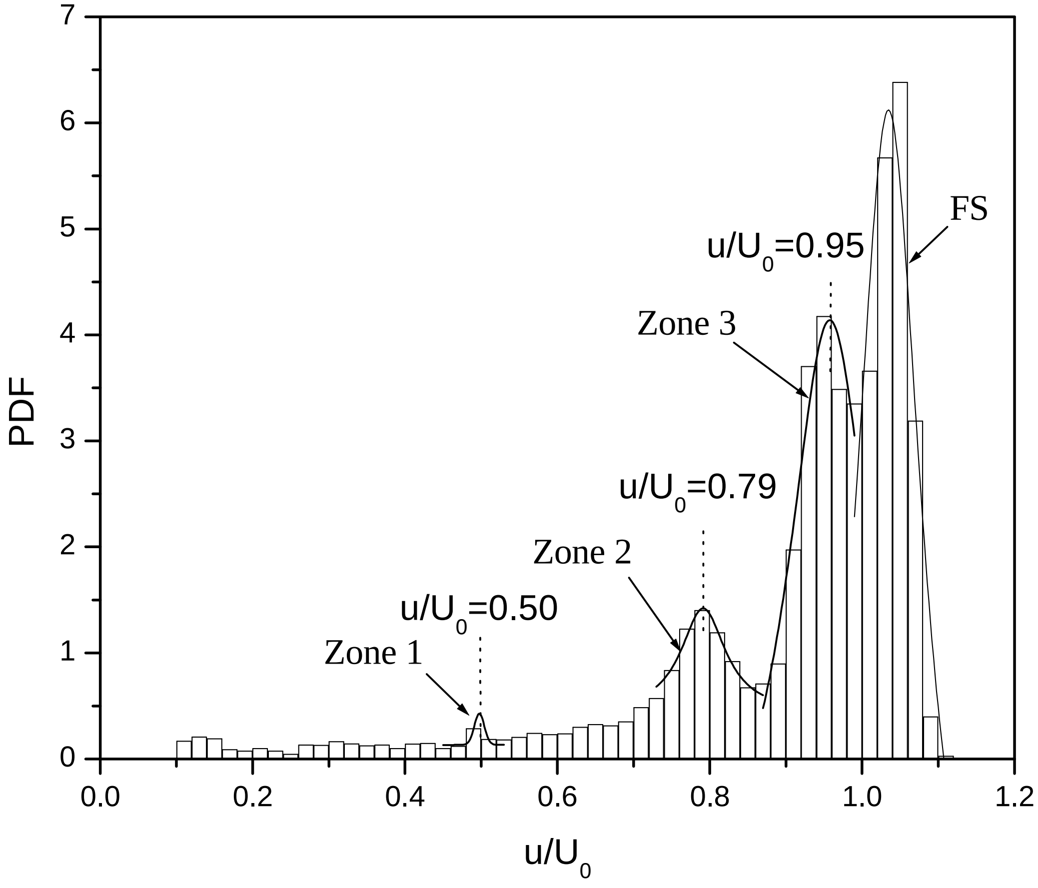

Figure IV-8. Histogram of the relative distribution of the instantaneous velocity field at t = 17.3 s showing the zones of the uniform momentum.

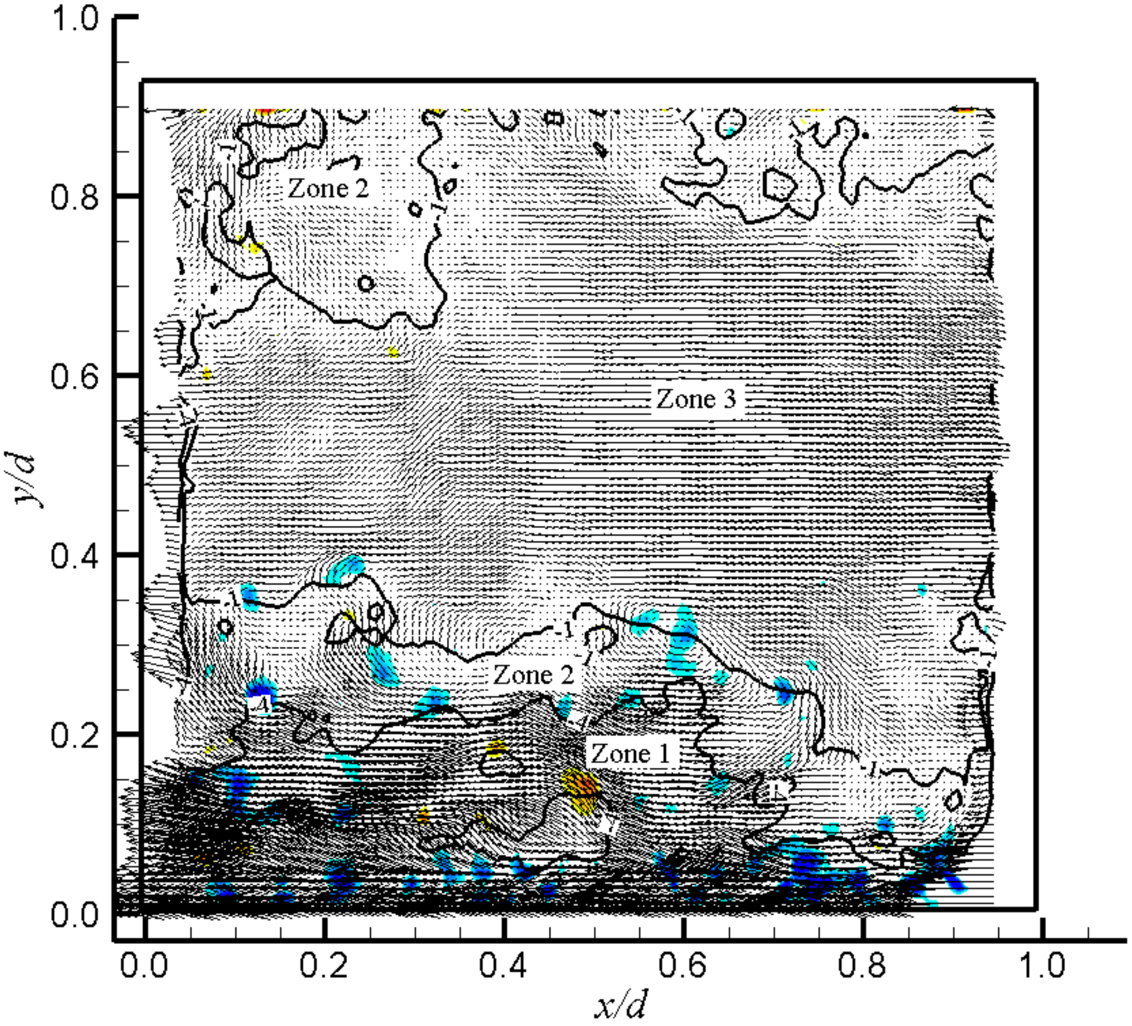

Figure IV-9. Vortices along the boundaries of the uniform-momentum zones. The vortices are identified with the swirling strength. The black lines separate the flow field into zones, labelled 1, 2 and 3 in which the streamwise momentum is nearly uniform. Instantaneous velocity vector map (t = 17.3 s) in a convection frame of reference $U_c = 0.95U_0$ is also shown.

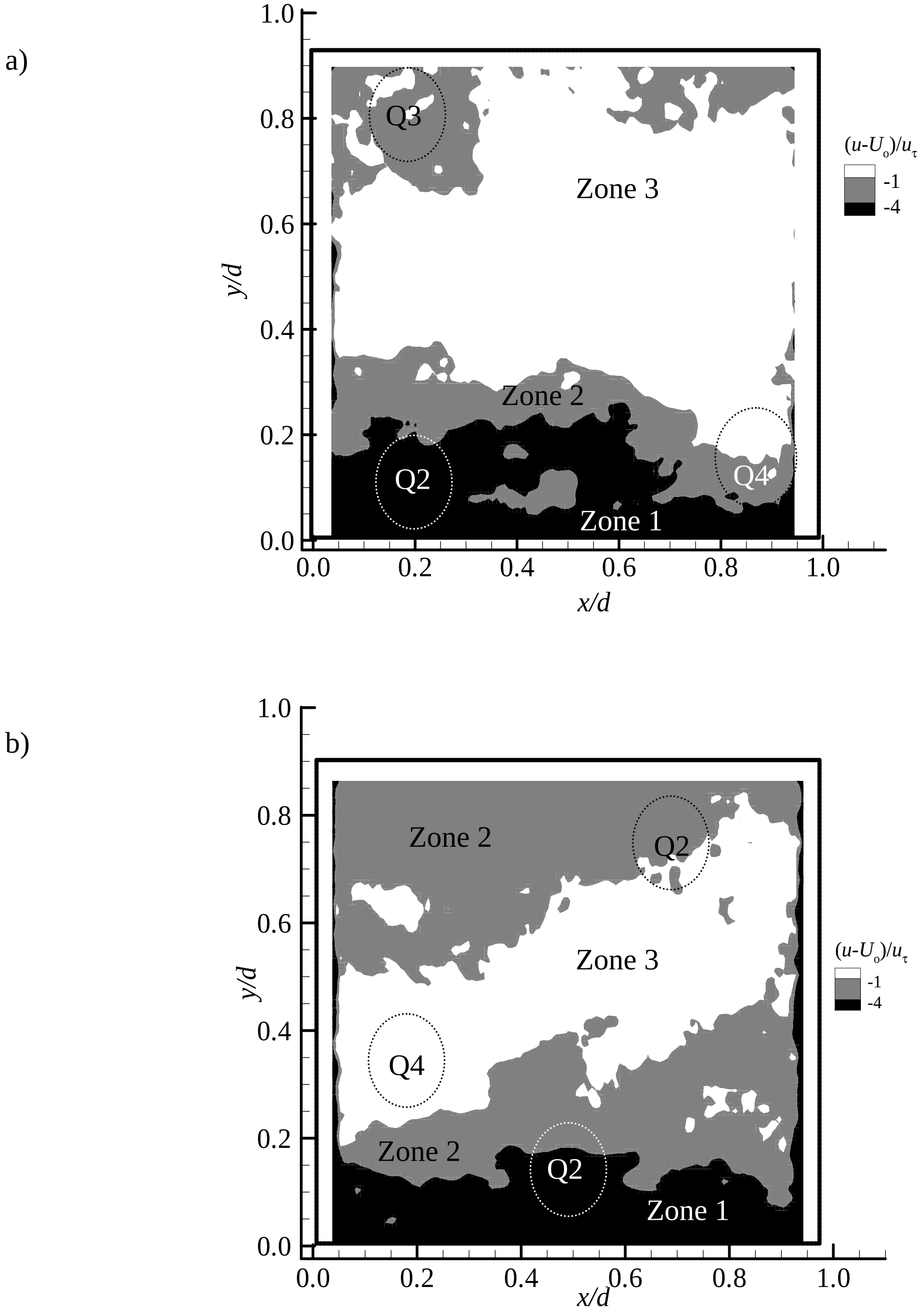

Figure IV-10. Zones of streamwise uniform momentum of the two velocity fields a) at t = 17.3 s and b) t = 28.1 s. The color map corresponds to $(u - U_0)/u_\tau$, where U_0 is time-averaged, maximum velocity and u_τ is the friction velocity.

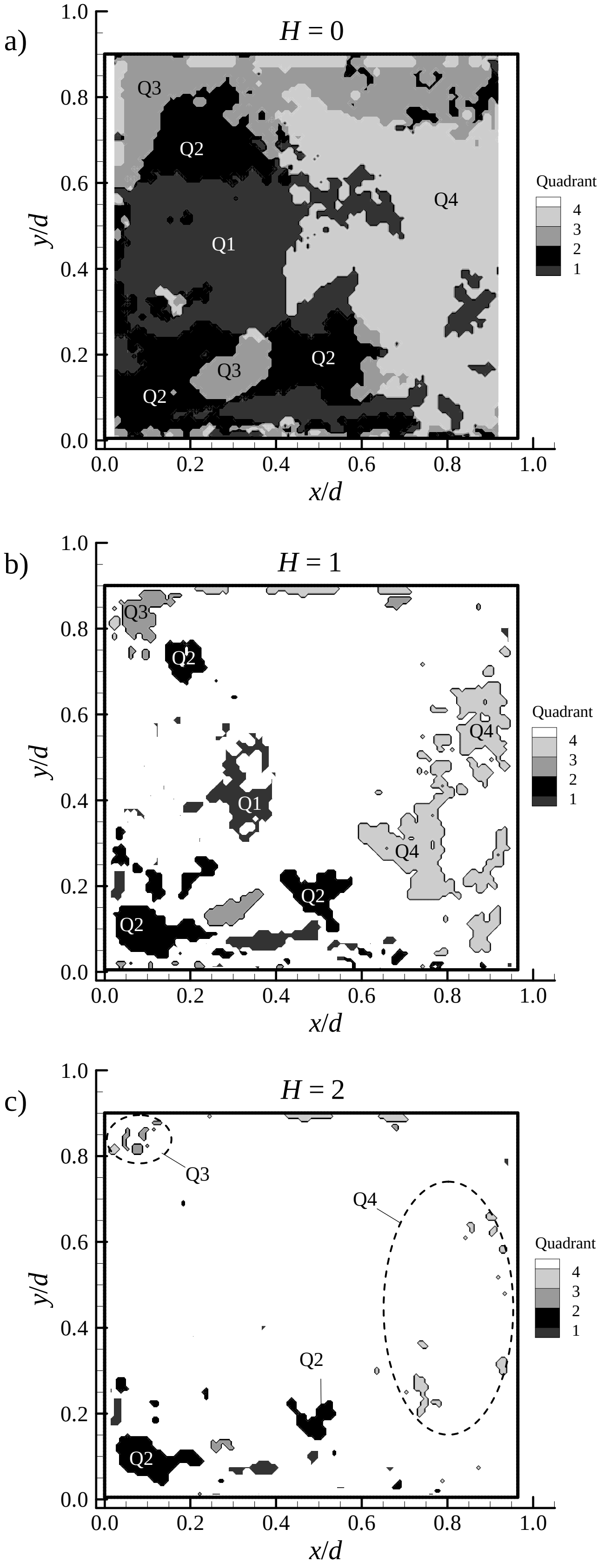

Figure IV-11. Color maps representing the quadrant analysis of instantaneous fluctuating velocity field shown in Figure IV-1b a) *H* = 0, b) *H* = 1 and c) *H* = 2.

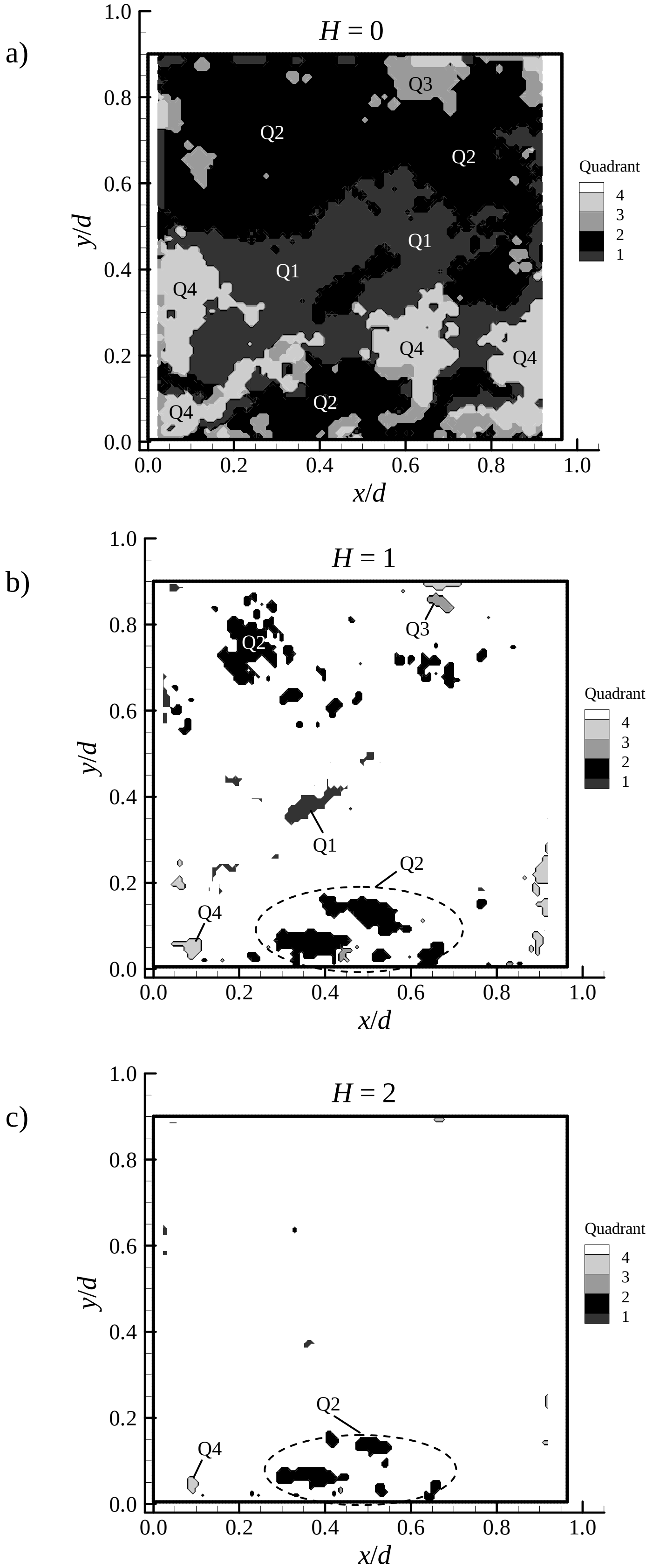

Figure IV-12. Color maps representing the quadrant analysis of instantaneous fluctuating velocity field shown in Figure IV-1c a) *H* = 0, b) *H* = 1 and c) *H* = 2.

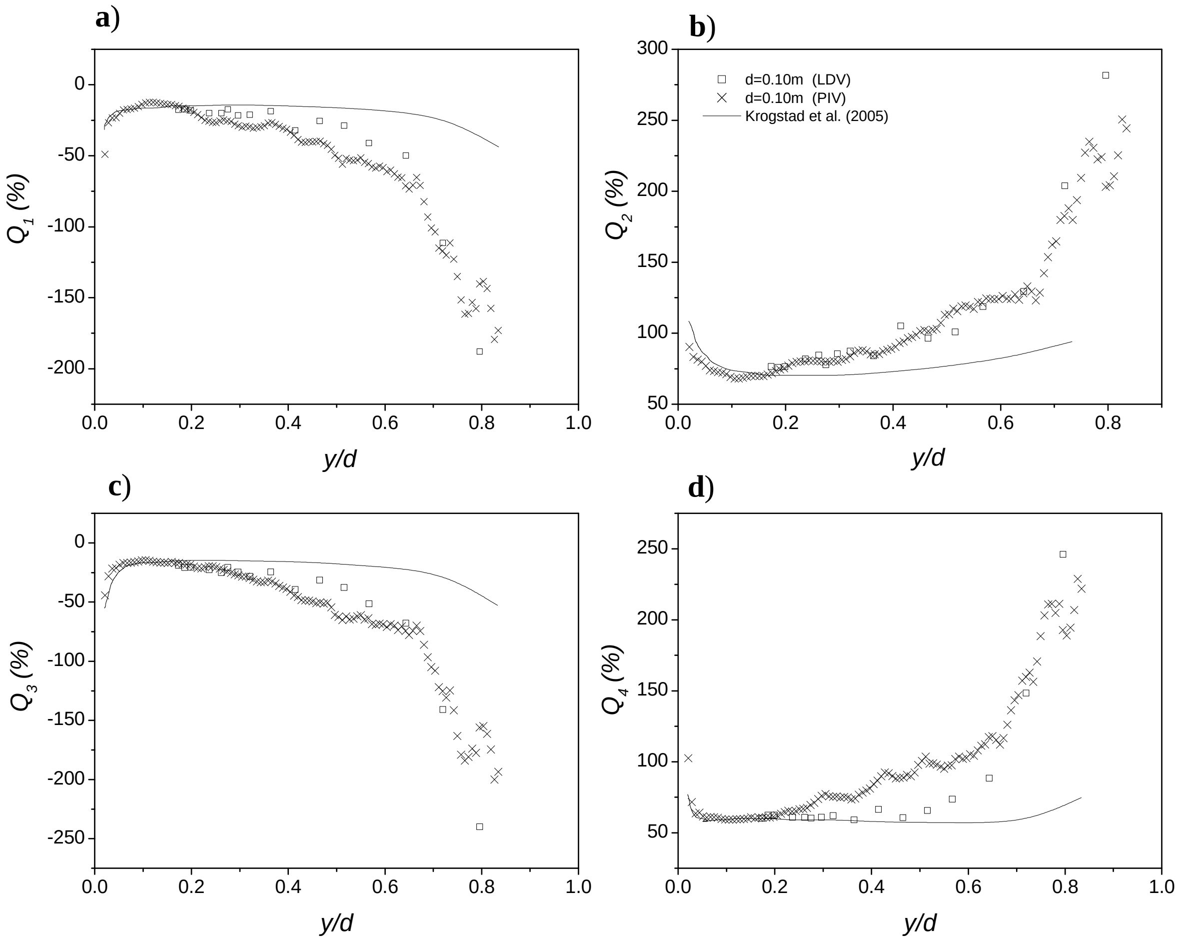

Figure IV-13. Stress fractions of each quadrant for *H* = 0: (a) Q1, (b) Q2, (c) Q3 and (d) Q4.

CHAPTER

V. EFFECT OF DEPTH ON FLOW PAST A TRAIN OF LARGE RIB ELEMENTS IN AN OPEN CHANNEL

In this chapter, the turbulent flow past a train of rib elements located in an open channel is examined at three depths of flow. The rib elements are composed of two-dimensional square rods spanning the width of the channel and are located throughout the length of the flume. The characteristics of the flow are examined at two different rib separations (p/k = 9 and 18; p is the pitch and k is the rib height) conforming to the classical definition of k-type roughness. The ratio of the rib height (k) to the depth of flow (d) varies from 0.10 to 0.15 and falls in the category of large roughness. For each of the six test conditions, two-dimensional laser Doppler velocimeter measurements were obtained at two locations, one on the top of the rib crests and one in the middle of the cavity formed between successive elements. An additional measurement location within the rib wavelength was also considered for p/k = 18 at $x = 4k$. From these measurements, information regarding the mean velocities, turbulent intensities, Reynolds shear stress and higher-order moments were obtained. Quadrant analysis was used to investigate the effect of flow depth on the turbulent structures in the outer layer.

5.1. Mean velocity profiles

In this section, the characteristics of the turbulent flow over the train of ribs at two locations: on top of the roughness element, (location x_A, see Figure II–1) and at the center of the roughness cavity (location x_B) are presented for p/k = 9 and 18. Results for the additional measurement location $x_C = 4k$ for p/k = 18 are also presented. This particular location is close to the point of reattachment and it matches geometrically with the location x_B for $p/k = 9$. In all of the forthcoming figures, measurements at location x_A are denoted by solid symbols while at x_B and x_C are denoted by open symbols. Mean velocities as well as various turbulence quantities are analyzed in order to understand the influence of the train of transverse ribs on the outer flow. An effort is also made to understand how the flow inside the cavity is perturbed when the depth of flow is reduced and how this affects the overlying flow in the case of large roughness of $k/d < 0.15$. The results are compared with similar flow conditions on a smooth bed as well as with the available experimental and DNS data.

When analyzing rough wall data, the zero-plane location or displacement height (d_1) is an unknown parameter which has to be determined (see Figure II–1). One of the solutions of this problem is to assume that a logarithmic layer exists and by fitting the velocity profiles, the value of the zero–plane location can be calculated along with the friction velocity, and velocity shift. Another solution has been recently proposed by Manes et al., (2007) which is applicable to the case of the flow with relatively small submergence.

In the present study, the profile matching Clauser technique was attempted but it was abandoned since the uncertainty in calculating the local friction velocity was much higher due to the uncertainty in the location of the surface origin. The fitting procedure was unsuccessful because only few points from the velocity profiles follow the logarithmic law. The method was also subjective as to where the boundaries of the logarithmic layer are chosen. Nikora et al., (2001) have shown that the zero-plane location depends not only on the roughness density but also on the energy of the large eddies. In general, the zero-plane is located farther from the wall with increasing roughness density and goes down with increase of the turbulent energy. Leonardi et al., (2003) calculated the zero origin for rib roughness from the DNS simulations and they showed that the location of zero origin depends on the pitch separation. The latter study predicted that for the rib separation $\lambda/k = 8$ the shift of the zero-plane is $d_1/k = 0.5$. This value becomes slightly smaller ($d_1/k = 0.45$) for large rib separation of $\lambda/k = 17$. In the present experiments, the zero-plane reference location was selected at the mean elevation of the roughness at $d_1/k = 0.5$. This choice of the zero origin is in accordance with the one suggested earlier by Jackson (1981) and later reproduced by the DNS simulations of Leonardi et al., (2003).

Figures V–1a-e show the mean velocity profiles for the two roughness conditions. In all forthcoming figures, the variables are plotted in outer scaling, where the total depth (d) of flow is selected as the characteristic length scale and maximum velocity (U_0) is chosen as the velocity scale. Further, y_1 is the vertical distance from the mid-plane of the ribs. Outer scaling presentation is more convenient since it uses measurable quantities and avoids using the friction velocity (u_τ) which is difficult to determine accurately in the case of the rough surfaces. In Table II-2, friction velocity u_τ, $u_\tau = (gRS)^{1/2}$, based on the experimentally measured slope (S) of the channel and the hydraulic radius (R) is listed. These values provide an average estimate of the friction velocity over the entire channel.

In Figures V–1a and 1c, mean velocity distributions on top of the rib are shown. Roughness has a profound effect on the shape of the mean velocity profiles. Unlike the smooth wall data, close to the rough surface, a kink in all velocity profiles is noticed. This is a direct effect of the formation of a small separation zone when the flow is deflected from the sharp leading edge of the rib. Enlargement of the velocity profiles for $y_1/d < 0.3$ (shown as insets in Figures V–1a and 1c), reveal that the vertical location of the kink depends on the depth of flow. For both p/k ratios, a maximum value of U/U_o is observed at the shallow depth $d = 0.065$ m. At $d = 0.065$ m, comparing the location of the maximum value of $U/U_o = 0.8$ between the two p/k values, one notes that the location is shifted slightly upwards at $p/k = 18$. One can also note that a thinner separation zone is formed on the top of the rib at the larger depths irrespective of the rib separation. For $p/k = 18$ and shallow water depth, the upcoming flow is deflected more in the wall-normal direction resulting in somewhat thicker separation zone. This is in agreement with the DNS simulations of Leonardi et al., (2006) who noted that for a pitch separation $\lambda/k = 59$, the mean streamline over the top of the rib extends to larger wall normal values than for $\lambda/k = 7$. Reduction of the flow depth could also further strengthen the waviness of the mean flow on the top of the rib. Since the flow separation is local phenomena, its effect is diminished with increasing distance from the bed. In both Figures V–1a and 1c, on top of the rib, at $y_1/d > 0.3$, velocity profiles at both p/k ratios are similar irrespective of the water depth.

The effect of the flow depth and the manner in which the flow inside the rib enclosure communicates with the outer flow was also considered and mean velocity distributions inside the cavity between adjacent ribs for $p/k = 9$ and 18 at locations x_B and x_C are shown in Figures V–1b, 1d and 1e. At these measurement locations, the shape of the velocity profiles is smoother and no effect of the local flow separation is noticed for both p/k ratios. Even though the local effect disappeared completely, the global effect due to the merging upstream shear layers is accumulated farther in the outer region. If the flow depth is large enough, these effects will be absorbed completely and no vertical separation between the velocity profiles will be noticed. For all *p/k* ratios, velocity profiles at shallow depths are shifted more to the left as shown in the Figures V‒1b, 1d and 1e. Generally, an increased roughness effect is indicated by the shift of the mean velocity profiles to the left which is consistent with experimental observations of Tachie et al., (2004) and numerical simulations of Leonardi et al., (2004). While Tachie et al., (2004) examined different rough beds, Roussinova et al., (2008) observed a similar shift of the velocity profiles on the smooth bed at three different water depths. In the present experiments, all rough velocity profiles are shifted more to the left compared to the velocity profiles on the smooth bed. This indicates an increased momentum deficit. In Figures V‒1b and 1d, near the rib crest, the flow is strongly sheared and inside the cavity the velocities are decreasing. At $y_1/d < 0.1$, the velocity profiles are more-or-less linear and independent of the water depth. Inside the cavity, a large recirculation region is formed with the point of reattachment located at about 4.0 times the rib height as shown by the LES simulation of Cui et al., (2003) and DNS simulations of Leonardi and Orlandi (2006). In Figures V‒1b and 1d, the velocity profiles in the outer region, show a vertical variation at different depths. This implies that the flow above the cavity is affected by the reduction of the depth. At *p/k* = 18, the flow inside the cavity tends to recover as indicated by the velocity profiles measured at 8.5k and shown in Figure V-1e. In the middle of the cavity, different rates of velocity attenuation are noticed for p/k = 9 (Figure V-1b) and *p/k* = 18 (Figure V-1e). In the present experiments, the rate of velocity attenuation is stronger for the case *p/k* = 18 (Figure V-1e) which indicates that the flow at this section is beyond the point of reattachment at all depths. This is also consistent with the observations of Coleman et al., (2007) and Raupach et al., (1991). While the mean velocities are not affected by the reduction of the flow depth inside the cavity, outside the separation region this influence results in a shift of the velocity profiles.

The present analysis of the mean velocity distributions for the two rib separations shows that on the top of the rib all profiles collapse on a single line in the outer region. Near the bed, local effect of the ribs result in the formation of a small recirculation zone associated with a shear layer. These local effects are absent at vertical locations beyond $y_1/d > 0.3$. In the cavity region, no effect of the local flow separation is noticed for both p/k ratios. While on the top of the rib, the velocity distributions in the outer layer do not depend on depth, in the mid-cavity section, a vertical variation is observed. Inside the rib enclosure, linear velocity profiles are obtained which is consistent with the observations of Coleman et al., (2007). In the middle of the cavity (locations x_B and x_C) and close to the ribs, the slope of the velocity profiles are independent of the flow depth but their slope depends on the roughness spacing.

5.2. Turbulence intensities and Reynolds shear stress

The distribution of the streamwise turbulence intensity, on top of the rib for $p/k = 9$ and $p/k = 18$ are shown in Figures V−2a and 2c. Higher turbulence intensities are obtained for all rough cases compared to the same flow conditions on the smooth wall. Unlike the observations of Okamoto et al., (1993), no self preservation of the turbulence intensities is noticed for $p/k = 9$ on top of the rib. This suggests that for this rib separation, the effect of the flow depth is not limited to the region close to the rib. Comparing Figures V−1a and 2a, one can note that the effect of depth is more significant in the turbulence intensity compared to the mean velocity profiles. Near the plane of the rib crests, a maximum value of the turbulence intensities is observed for all rough cases. This peak is due to the formation of the shear layer as the flow separates from the leading edge of the rib. A sharp decrease of the streamwise turbulence intensities is observed for both p/k ratios in the region $0.1 < y_1/d < 0.15$. In Figures V‒2a and 2b, the values of the turbulence intensities drop about three times from the maximum value for the $p/k = 9$ and five times from the maximum for $p/k = 18$. For $y_1/d < 0.2$, while for $p/k = 9$, the location of the minimum value of the turbulence intensity is shifted slightly upwards at shallow depths, no such variation with depth is observed for $p/k = 18$. With increasing vertical distance from the bed, it was observed that the turbulence intensities increase slightly attaining a secondary maximum for $p/k = 9$. In Figure V-2a, the location of this local maximum shifts upwards with reducing depth and it is located at $y_1/d = 0.30$ for the shallow depth. The local increase of the turbulence intensities is related to the shear layers originating from the upstream ribs and accumulation of the turbulence effects. At $p/k = 18$, there is no visible local maximum due to the fact that the shear layers have to travel longer distances and its cumulative effects are reduced prior to reaching the next rib (Figure V-2c). Figure V-2a clearly shows that reduction of the depth leads to increase of turbulence in the outer region. Higher turbulence intensities are obtained for $p/k = 9$ at all depths compared to the same cases at large $p/k = 18$. This is in agreement with the observations of Okamoto et al., (1993) who found that the $p/k = 9$ is optimal to augment the turbulent intensity. Near the free surface, the turbulence intensity profiles on the top of the rib flatten out and reach different constant values depending on the flow depth. A constant turbulence intensity of $\overline{u^2}/U_0^2 = 0.02$ is measured for the $d = 0.065$ m while this value drops by 50% ($\overline{u^2}/U_0^2 = 0.01$) at larger depth d = 0.105 m. At *p/k* = 18, a near constant turbulence intensity of $\overline{u^2}/U_0^2 = 0.01$ is attained near the free surface independent of the flow depth. At large rib separation *p/k* = 18, the effect of the depth is less obvious.

The profiles of turbulence intensity in the center of the cavity for *p/k* = 9 and *p/k* =18 are shown in Figures V–2b and 2e, respectively. In Figure V-2d, turbulence intensities near the reattachment point (x_C = 4k) are also presented for large *p/k* = 18. Just above the plane of the rib crest, all turbulence intensity profiles attain a maximum. Higher level of turbulence intensities is observed at *p/k* = 9 at all depths. In Figure V-2b, the maximum value of turbulence intensity ($\overline{u^2}/U_0^2 =$ 0.063) is obtained for *d* = 0.065 m at y_1/d = 0.1. In the middle of the cavity, the peak of the turbulence intensities is reduced compared to the peak observed on the top of the rib (Figure V-2a). The reduction of the turbulence intensities is due to the break-up of the streamwise vortices interacting with the strong outflows from the cavity. This has also been observed by other investigators (e.g., in the experiments of Grass, 1971 and Krogstad and Antonia, 1999). The $\overline{u^2}$ profiles suggest that the roughness effect is not local, and extends to the outer region beyond $y_1/d \approx 0.2$. Near the free surface, the value of $\overline{u^2}/U_0^2$ is 0.025 at shallow depth (*d* = 0.065 m) while for deep-flow case (*d* = 0.105 m) the value of $\overline{u^2}/U_0^2$ is 0.01. The present data does not conform to the wall similarity hypothesis. At *p/k* = 18, near the reattachment point (x_C = 4k), all profiles attain maximum value of $\overline{u^2}/U_0^2 =$ 0.055 independent of the flow depths. Further reduction of the maximum $\overline{u^2}/U_0^2$ value is noted in the middle of the cavity for *p/k* = 18 as indicated in Figure V-2e. In this figure, in the outer region, the turbulence intensities slowly decay and near the free surface attain constant values lower than these obtained at *p/k* = 9. The turbulence intensities at large *p/k* ratio, inside the cavity are less affected by the change of the flow depth compared to *p/k* = 9.

In Figures V–3a and 3c the distributions of the Reynolds shear stress on top of the rib are shown for *p/k* = 9 and 18. All Reynolds shear stress profiles attain maximum near $y_1/d \approx 0.2$ and then decay slowly towards the free surface. The highest maximum value of the Reynolds shear stress $-\overline{uv}/U_o^2 = 0.016$ is observed at *p/k* = 9 for *d* = 0.065 m. This value is similar to the value obtained in the LES calculations by Cui et al., (2003). The location of the peak is also consistent with the LES calculations for the k-type roughness. For the deepest case (*d* = 0.105 m), the maximum value of the Reynolds shear stress is $-\overline{uv}/U_o^2 = 0.010$. This shows that at lower depths, there is an increase of the Reynolds shear stress which can lead to increased friction. At large rib separation, the maximum value of Reynolds shear stress is lower $-\overline{uv}/U_o^2 = 0.008$ and the location of the maximum does not depend on the flow depth (Figure V-3c). In the outer region, higher values of the Reynolds shear stress are obtained at the shallow depth. Distributions of the Reynolds stress within the cavity are shown in Figures V–3b, 3d and 3e. In all rough profiles, the Reynolds shear stress attains maximum inside the rib enclosure. Further away, at the plane of the rib crests the shear stress profiles decay and depend on the flow depth.

5.3. Conditional quadrant analysis

The *u*-*v* sample space of the fluctuating velocities can be divided into four quadrants. Such representation has potential to reveal the relative contribution of the turbulent structures (events) from different quadrants to the total Reynolds shear stress from single point LDV measurements. Flow visualization studies on rough wall bounded flows by Grass (1971) documented a streak that migrates slowly away from the wall and at some point detaches from it completely. This process of upward lifting of low-speed fluid away from the solid wall is commonly referred to as *ejection*. During the ejection process, the instantaneous local velocity ($u_{\hat{i}}$) is lower than the time-averaged local velocity (U). Whenever ejection occurs, in order to satisfy continuity, high speed fluid moves towards the wall ($u'_i > 0$) from other regions and this event is called a *sweep*. It is only possible to detect ejection events when $u < 0$ and $v > 0$ are observed simultaneously. In the same way, sweep events can be detected by simultaneously observing a high-speed fluid parcel ($u > 0$), moving towards the bed ($v < 0$). There are two other events that also contribute to the total Reynolds shear stress. They are known as outward interactions ($u > 0, v > 0$) and inward interactions ($u < 0, v < 0$).

Information about the coherent structures can also be obtained from the analysis of the higher-order turbulent moments as they retain sign information of the velocity fluctuations. Raupach (1981) established a relation where the difference between the sweep and ejection events is related to the third-order moments (M_{ij}) defined as

$$M_{ij} = \frac{\overline{u^i v^j}}{u_{rms}^i v_{rms}^j} \tag{V.1}$$

where, $i+j = 3$, so that M_{30} and M_{03} are the skewness of u and v, respectively. In Figure V-4 distributions of M_{30} and M_{03} are shown for the present experiments. While for all cases, the M_{03} is always positive M_{30} is negative and only at locations near the roughness it becomes equal to zero. The effect of the depth is more visible from the vertical variation of the M_{30} profiles where the profiles do not collapse. By reducing the depth of flow, the values of the M_{30} are increased for both p/k ratios at all measurement locations. In the outer region, ejections events continued to be observed since $u < 0$ and $v > 0$. In the roughness cavity, M_{30} is positive in the vicinity of the mid-plane of the ribs and increases further as the bed is approached. At these locations, no information for the M_{03} is available due to the limitations in the present measurements.

Conditional quadrant decomposition is attempted at two locations: on the rib crest and in the middle of the cavity. For brevity, to examine the influence of the fluid interface on the turbulent structures, quadrant distributions only in the middle of the cavity are discussed. At every measurement location, the Reynolds shear stress is calculated and further decomposed as a sum of different events according to the procedure described by Lu and Willmarth (1973). By using the concept of a hyperbolic hole of size H, defined by $|uv| = Hu_{rms}v_{rms}$, the contribution from a particular quadrant can be written as

$$(uv)_{Q_i,H} = \lim_{T\to\infty}\frac{1}{T}\int_0^T u(t)v(t)I(t)dt \tag{V.2}$$

Here, I(t) is a detection function defined as:

$$I(t) = \begin{cases} 1 & when \quad |uv|_Q \geq Hu_{rms}v_{rms} \\ 0 & otherwise \end{cases} \tag{V.3}$$

It is assumed that the velocity used to compute $(uv)_{Q,H}$ is a function of time only. The parameter H defines a threshold value, which separates the extreme events from the random background turbulence. By increasing the value of H more extreme/strong events are identified. Quadrant decomposition yields three quantities of interest in assessing the overall contributions of ejections, sweeps and inward/outward interactions to the mean Reynolds shear stress:

1) the Reynolds stress contributed to each quadrant for a given H denoted as $(uv)_{Q_i}(y)$;

2) the stress fraction associated with each quadrant event for a given H:

$$S_{Q_i}(y) = \frac{(uv)_{Q_i}(y)}{\overline{uv}(y)}; \tag{V.4}$$

3) the occurrence probability for each quadrant for a given H:

$$P_{Q_i}(y) = \frac{\sum I(uv)_{Qi}}{\sum_{i=1}^{4}\left(I(uv)_{Qi}^{H=0}\right)}. \tag{V.5}$$

Note that the occurrence probability is computed over the total number of data at H = 0 as shown above. Two hole sizes, H = 0 and 2 are studied and represent contributions to the total mean Reynolds shear stress from all and strong events, respectively.

In Figures V–5 and 6 the stress fractions (S_{Qi}) for *p/k* = 9 and 18 are respectively shown. All rough wall data are compared with the smooth wall profiles at similar depths of flow. While little dependence on flow depth is observed near the roughness for both p/k cases at H = 0 (Figures V–5a-5c; Figures V–6a-6c), an increase of Reynolds-stress-producing events, particularly ejections and sweeps are observed near the free surface. The effect is somewhat more noticeable at larger depths *d* = 0.085 m and 0.105 m (Figures V–5b, 5c, 6b and 6c). Such rapid increase of the intensity of each event near the free surface was reported earlier by Nakagawa and Nezu (1977) where the contributions from ejections and sweeps are found to increase over 100%. In the present experiments, only for *p/k* = 9 at the shallow depth (Figure V-5a), the stress fractions for H = 0 near the free surface deviate from the smooth wall data. For this case, an increase in the contributions from ejections and sweeps are observed in the region $y_1/d > 0.6$. In Figure V-6a, no such increase of ejections and sweeps is visible near the free surface for H = 0. For large $p/k = 18$ and H = 0, no difference between the smooth and rough vertical distributions of all stress fractions is observed. For H = 0, the inward and outward interactions for smooth and rough beds (Figures V–5 and 6) generate stress fractions with magnitudes that are three times smaller than ejections and sweeps over the same wall-normal extent.

Using H = 2 ensures that only the stronger stress producing events (with instantaneous Reynolds shear stress higher than $5.5\overline{uv}$) are considered in the quadrant decomposition. In Figures V–5d-5f and 6d-6f, contributions from inward and outward interactions are close to zero while contributions from ejections and sweeps show dependence on the flow depth in the region $y_1/d > 0.5$. Contributions from strong ejections on the rough beds are found to be more affected by the flow depth not only near the free surface but also close to the bed. For example, in Figures V–5d, 5e, 6d and 6e, larger contribution of the ejections is visible in the region $y_1/d < 0.20$ compared to that for the smooth bed. Although all stress fractions for H = 0 are not very sensitive to the change of flow depth, the stress fractions associated with the strongest ejections (H = 2) are somewhat more affected by the reduction in depth.

Above $y_1/d = 0.2$ and for H = 0, the highest occurrence probabilities (P_{Qi}) are detected for sweep events followed by the ejection events as shown in Figures V–7a-7c and 8a-8c. The occurrence probabilities of sweep and ejection events are constant in the region $0.2 < y_1/d < 0.5$ and they tend to reduce as the free surface is approached for H = 0 (Figures V–7 and 8). While for $p/k = 9$ and H = 0, the probability of sweeps decrease towards the free surface at all depths; for large p/k = 18, a constant P_{Q4} is noted along the wall-normal direction for the shallow case. The other events, the outward and inward interactions have relatively small occurrence probability for H = 0. Similar results was obtained by Nezu and Nakagawa (1993) who found that the strongest events are ejections while the most frequent events are sweeps when all turbulence is considered (H = 0).

Increasing the hole–size value to H = 2 and eliminating the weaker events results in an overall reduction of all probabilities. For H = 2, the occurrence probabilities of ejections and sweeps are much larger than the probability of inward and outward interactions. For H = 2 the highest probability of occurrence is obtained for the ejections events (second row of Figures V–7 and 8). By increasing the hole size to H = 2, the dominance shifts from sweeps to ejections. Similar shift was also reported by Cellino and Lemmin (2004) for the case of the clear water over a rough gravel bed. The highest probability of occurrence of ejections and sweeps are observed near the bed at $y_1/d \approx 0.1$ for H = 2. At $y_1/d > 0.2$ the distributions of the ejections at larger depths on both rough beds tend to become similar to those on the smooth bed. For p/k =9, less sweeps are generated in the vicinity of the roughness at all depths compared to the smooth wall case as shown in Figures V–7d-7f. For p/k = 18 better collapse between the rough and smooth wall profiles of P_{Q4} are obtained only for d = 0.105 m (Figure V-8f). Further away from the roughness at $0.2 < y_1/d < 0.6$, near constant values of occurrence probability of sweeps is noted only for the shallow depth at both p/k ratios. For larger depths, the probability of occurrence of sweeps tend to decrease near the free surface as indicated in Figures V–7e, 7f, 8e and 8f. At H = 2 and shallow depth, the occurrence probability of ejections and sweeps for *p/k* =9 and 18 consistently deviate from the occurrence probability obtained on the smooth wall.

Finally, in Figure V-9, the ratios between the contributions from sweep and ejection events for *p/k* = 9 and 18 calculated in the middle of the cavity are shown. At H = 0, when all turbulent events are included, the larger deviations from the smooth wall data are noticed at shallow depths (Figures V–9a and 9b). At d = 0.105 m the $(uv)_{Q_4}/(uv)_{Q_2}$ ratios on rough and smooth beds are similar in the region $y_1/d > 0.4$. This is expected since for the deep-flow case, the stress fractions of ejections and sweeps on smooth and rough beds are found to be similar (Figures V–5c and 6c) irrespective of the p/k ratio. In Figure V-9c, the effect of the rib separation is also visible and similarity between $(uv)_{Q_4}/(uv)_{Q_2}$ at *p/k* = 18 and on the smooth bed is noticed beyond $y_1/d > 0.2$. For H = 0 and deep-flow case, the ratio of $(uv)_{Q_4}/(uv)_{Q_2}$ attains a minima located at $y_1/d = 0.5$ (Figure V-9c) whereas for a shallow depth the distributions on the rough beds are constant along the vertical axis. When all turbulent events are included, higher values of $(uv)_{Q_4}/(uv)_{Q_2}$ are obtained at d = 0.065 m for both rib separations. In Figures V–9a and 9b, the trend of $(uv)_{Q_4}/(uv)_{Q_2}$ ratios for rough walls at H = 0 and shallow depths are constant, showing increasing importance of ejection events throughout the depth. These trends are consistent with the stress fractions shown in Figures V–5a-5c and 6a-6c. For H = 0, the most frequent events are sweeps however they contribution to the total Reynolds shear stress is less important as shown in Figures V–7a-7c and 8a-8c. The direct influence of the large roughness is seen close to the roughness (y_1/d < 0.2), where all $(uv)_{Q_4}/(uv)_{Q_2}$ ratios deviate from the ones calculated on the smooth wall. Overall, it is concluded that the distributions of $(uv)_{Q_4}/(uv)_{Q_2}$ for H = 0 depends on depth as large roughness control the turbulent events at shallow depths.

The use of H = 2 further emphasizes the differences in $(uv)_{Q_4}/(uv)_{Q_2}$ in the outer region for the different depths as shown in Figure V-9. By removing some of the turbulence events, the trends of the distributions remain similar to the unfiltered ones although the values are about 50% lower. At intermediate depth (d = 0.085 m), somewhat better collapse between the smooth and rough $(uv)_{Q_4}/(uv)_{Q_2}$ ratios are obtained in the region $y_1/d > 0.5$. Increasing turbulence level is clearly visible in Figure V-9a where the highest value of $(uv)_{Q_4}/(uv)_{Q_2} = 0.4$ is obtained for d = 0.065m in the outer region $y_1/d > 0.4$. The values of $(uv)_{Q_4}/(uv)_{Q_2}$ are always less than 0.4 for large and intermediate depths at the same vertical region ($0.4 < y_1/d < 0.8$) as seen from the Figures V–9b and 9c. This confirms that ejections dominate over sweeps at all measured vertical locations. For H = 2, the values of $(uv)_{Q_4}/(uv)_{Q_2}$ never exceeds 1, which is in contrast with the observations of Schultz and Flack (2005) and Wu and Christensen (2006) where the roughness heights were smaller. Larger values of $(uv)_{Q_4}/(uv)_{Q_2}$ on the smooth bed are obtained near the roughness.

The present quadrant analysis complements previous research published by other investigators (Nakagawa and Nezu 1977 and Raupach 1981) by emphasizing the effect of depth on flow past a train of large ribs. The turbulence structures are affected by both the large roughness and flow depth. The effect of the roughness on the turbulent structures becomes less obvious in the deep-flow case whereas at the shallow depth, large roughness control the flow. For H = 0, stress fractions from ejections and sweeps contribute the most to the total Reynolds shear stress and they increase near the free surface. At shallow depth this increase seems to depend on the *p/k* ratio. The space fractions show a shift from sweep to ejection dominated flow at H = 2. Similar probability of occurrence of strong ejections and sweeps are noticed between the smooth and rough data at larger depths. At shallow depth, the stress fractions and the probability of occurrence of strong ejections and sweeps consistently deviate from the ones obtained on the smooth bed. For the rough shallow case the values of $(uv)_{Q_4}/(uv)_{Q_2}$ are very different from these obtained on the smooth bed, while for the large depth this difference diminishes in the outer region where the turbulent structures becomes similar to those on the smooth bed.

5.4. Anisotropy analysis

Open channel flow over a train of large rib roughness (*k/d* > 0.10) is examined with two objectives: first, to investigate the effect of the rib separation (*p/k*) on turbulence anisotropy at fixed depth and second to study the effect of flow depth for two k-type rough configurations. For the first set of experiments, the spacing between the roughness elements was varied to reproduce the conditions of d- and k-types roughness at fixed flow depth of *d* = 0.10 m. Three rib separations (*p/k*) of 4.5, 9 and 18 are examined. For the second set of experiments, three flow depths (*d* = 0.065m, 0.085 m and 0.10 m) were examined at two rib separations of *p/k* = 9 and *p/k* =18. Detailed LDV measurements of streamwise and wall normal velocity components were obtained above the rib crest for all cases, and therefore in the forthcoming figures zero wall normal location (*y/d* = 0) is considered at the rib crests.

5.4.1. Effect of the p/k at constant flow depth *d* = 0.1 m

In Figures V–10a and 10b, profiles of the stress ratios $\overline{v^2}/\overline{u^2}$ are shown on the top of the rib and in the middle of the cavity, respectively, for the three rough separations. The present rough wall data are also compared with the smooth wall data at similar depth (*d* = 0.10 m) as well as with the rough wall data by Krogstad et al., (2005) and Leonardi (2002). One should note, that the data set by Krogstad et al., (2005) is obtained in a 2-D rough channel with *p/k* = 8 and roughness height of *k/h* = 0.034 (*h* is the half-height of the channel) which is smaller than the roughness used in the present study.

For the k-type roughness, $\overline{v^2}/\overline{u^2}$ profiles attain a local maximum near the plane of the rib crests as shown in Figure V-10a. This corresponds to the wall normal location where the vertical fluctuations are nearly the same order of magnitude as the streamwise fluctuations. It is interesting to note that the highest peak of $\overline{v^2}/\overline{u^2}$ ratio is obtained at large rib separation of *p/k* = 18 at *y/d* = 0.075. At this rib separation, the turbulence tends to be more isotropic. A similar, but smaller peak in the stress ratio can be noted for *p/k* = 9. The same trend was also observed by Djenidi et al., (2007) who show that close to the wall, the data for *p/k* = 8 were consistently lower than those of *p/k* = 16. Near the rib crest, with decreasing rib separation the stress ratio becomes reduced and no peak is found for the d-type roughness. The d-type roughness data approach the smooth wall data. In the outer region (*y/d* > 0.2), higher values of $\overline{v^2}/\overline{u^2}$ are obtained for the large separation of *p/k* = 18, while moderate increase is observed for *p/k* = 9 and 4.5. All rough wall data indicate higher stress ratios than the smooth wall data over a significant part of the outer region. This suggests that the effect of the roughness is not localized and the strongest interaction between the roughness sublayer and the outer layer is obtained at *p/k* = 18. While the blockage of the roughness was only 3% for the data set of Krogstad et al., (2005), the blockage of the ribs for the present open channel flow is 10%. This will explain the different behavior of the stress ratios particularly near the roughness. In Figures V–10a and 10b, an additional DNS data by Leonardi (2002) are provided with the roughness that occupies 20% of the half-height of the channel. Both DNS simulations and present rough wall open channel data show similar trends of the stress ratios at the plane of the ribs.

Inside the cavity between successive ribs (Figure V-10b), near the plane of the crests, a peak of $\overline{v^2}/\overline{u^2}$ is visible in both x = 4k and 8.5k profiles at $p/k = 18$, with a magnitude smaller than that observed on the top of the rib. At x = 4k, higher values of $\overline{v^2}/\overline{u^2}$ are shifted outwards in the region $0.15 < y/d < 0.4$. This suggests that for $0.15 < y_1/d < 0.4$, the wall normal fluctuations are larger and strong ejections are generated near the reattachment point. The flow tends to be more isotropic in this location. In Figure V-10b, at wall normal locations $y_1/d > 0.4$, similar values for the stress ratios are obtained for both profiles at $p/k = 18$. At x = 4k, strong outward motions penetrate deeper into the outer layer. Similar values of the stress ratios were obtained for $p/k = 4.5$ and 9 which suggests that in the middle of the cavity, the flow is independent of the of the roughness density. However, at $p/k = 18$ the flow is still sensitive to the upstream roughness density and its effect is felt well into the outer layer.

In Figure V-10c and 10d the correlation coefficient $\rho_{uv} = -\overline{uv}/(\overline{u^2}\,\overline{v^2})^{1/2}$ are shown on the top of the rib and in the middle of the cavity for p/k = 4.5, 9 and 18. The correlation coefficient, ρ_{uv} is larger for $p/k = 18$ than for $p/k = 9$ and 4.5, near the plane of the rib crest and it decreases monotonically towards the free surface (Figure V-10c). Only a very small portion of the profiles near the rib plane attain constant values between 0.4 and 0.5. Nezu and Nakagawa (1993) have shown that these are typical values of ρ_{uv} for boundary layers and pipes, and an universal correlation was established that is independent of the mean flow conditions and wall roughness. The present data show that ρ_{uv} depends on the wall roughness. In Figure V-10d, ρ_{uv} is maximum near the plane of the rib crests where the values of $-\overline{uv}$, $\overline{u^2}$ and $\overline{v^2}$ fluctuations are higher for k-type roughness. The same trend is observed above the cavity where $-\overline{uv}$, $\overline{u^2}$ and $\overline{v^2}$ values are even higher (close to the plane of the rib). The effect of these vortices appear to be stronger for p/k = 18. While in the outer region ($0.2 < y/d < 0.6$), the rough wall correlation for p/k = 9 become similar to that on the smooth wall ρ_{uv} for p/k = 4.5 seems to deviate from the smooth wall data. The present roughness does not show reduction of ρ_{uv} as reported by Djenidi et al. (1999).

The components of the Reynolds anisotropy tensor, b_{ij}, on the top of the rib, are plotted in Figure V-11a. For p/k = 18, b_{11} and b_{22} profiles indicate that the flow near the roughness tends to be more isotropic. This result is somewhat different from the predictions of Leonardi et al., (2006) who noticed that as the roughness separation increased the flow anisotropy also increased and in the limit of large p/k the flow eventually attains features similar to the flow over a smooth bed. The simulations of Leonardi et al., (2006) also show that maximum isotropy is achieved with p/k = 8 for h/k = 10, where h is the half-height of the channel. With decreasing p/k, the present results in open channels show a slow return to the smooth wall condition. For comparison, the DNS results at p/k = 8 denoted by the solid lines are also shown in Figure V-11a. Inside the roughness sub-layer ($y/d < 0.2$) the flow tends to be more isotropic for k-type roughness than for d-type roughness. While for $p/k = 18$ at $y/d = 0.07$ and for $p/k = 9$ at $y/d = 0.05$ a strong reduction for the b_{11} and b_{22} components of the anisotropy tensor is observed, for $p/k = 4.5$ an increase of the two anisotropy components is obtained. The different trends of b_{11} and b_{22} for d- and k-type roughness in the roughness sublayer are expected since the mechanism of turbulent production is different. A good collapse between the rough wall data of $p/k = 4.5$ and 9 is noticed in the outer region ($0.2 < y/d < 0.8$). The overall anisotropy for $p/k = 18$ is smaller and it extends throughout the entire outer layer. Generally, the b_{11} and b_{22} components on the rough wall tend to be more isotropic than the smooth wall a result consistent with the previous boundary layer studies.

In Figure V-11b, components of the Reynolds stress anisotropy tensor within the cavity are shown. For both rib separation of $p/k = 4.5$ and 9, similar levels of anisotropy are observed throughout the depth of flow suggesting that at this measurement location the turbulence is independent of the roughness density. For $y/d < 0.2$, different trends in of the b_{11} and b_{22} profiles are noticed for $p/k = 18$ compared to the other conditions. Close to the plane of the rib crest ($y/d < 0.2$), the flow tends to be more isotropic not only at location of reattachment ($x = 4$k) but also in the post reattachment zone at $x = 8.5$k as shown in Figure V-11b. Outside the roughness sub-layer at $0.2 < y/d < 0.5$, there are some differences between the anisotropy components of k- and d- type roughness. For example, more isotropic turbulence is attained for $p/k = 18$ at the location of reattachment at $x = 4$k. Less anisotropy is attained in the post-reattachment region of $p/k = 18$, compared to the $p/k = 4.5$ and 9. At $y/d > 0.5$, all components of the anisotropy tensor are independent of the roughness separation, and, in this region, the anisotropy on the rough wall is generally smaller than for a smooth wall.

Within the roughness cavity, the $-b_{12}$ components attain maximum near the plane of the rib crests. Very small portion ($0.1 < y/d < 0.5$) of the $-b_{12}$ values (so-called structure parameter Townsend, 1961) are constant of about 0.14. Near the free surface, the values of the $-b_{12}$ are approaching zero irrespective of the bed roughness.

The results obtained from the Reynolds stress anisotropy tensor are similar to the results of the previous discussion on the stress ratios. One should note that in calculation of the components of the Reynolds stress anisotropy tensor, b_{ij}, an approximation for the spanwise component ($\overline{w^2}$) is adopted due to the experimental difficulties of measuring the three velocity components simultaneously. Further studies should be carried out to measure the three velocity components simultaneously near the rough wall.

5.4.2. Effect of the flow depth

A rough guide to large-scale anisotropy effects can be obtained by investigating the ratios between various Reynolds stresses. In Figure V-12, stress ratios ($\overline{v^2}/\overline{u^2}$) at different flow depths are presented at two streamwise locations: on the rib crest and in the middle of the cavity for $p/k = 9$ and $p/k = 18$, respectively. An additional location near the reattachment point at $x_c = 4k$ is also probed for large $p/k = 18$. At shallow depth ($d = 0.65$m), the stress ratio increases near the rib crest for both rib separations and for $p/k = 18$ attains maximum value $\overline{v^2}/\overline{u^2} = 0.90$ at $y/d = 0.1$. A slightly depressed value of $\overline{v^2}/\overline{u^2}$ is noted for $p/k = 9$. Near the rib crest $\overline{v^2}$ increases (Figure V-2) due to the formation of the shear layer originating from the upstream rib. It appears that this shear layer is affected not only by the roughness but also by the reduction of depth. For the shallow rough flow case at *p/k* = 18, the turbulence tends to be more isotropic and the interaction between the outer layer and the roughness sublayer is the strongest. While in Figure V-12a the value of $\overline{v^2}/\overline{u^2}$ is affected only near the roughness (*y/d* < 0.2), in Figure V-12d at p/k = 18, almost half of the flow depth is affected. This shows that above roughness elements with large p/k = 18 the flow is strongly influenced the depth. With increasing flow depth only the effect of the roughness remains which is localized near the roughness. Completely different trends of the stress ratio profiles are observed in the middle of the roughness cavity as shown in Figures V−12b, 12d and 12e. In these locations no effect of the depth is observed in the outer region for both *p/k*. The flow in the middle of the cavity accelerates towards the downstream rib, causing equal distribution between $\overline{u^2}$ and $\overline{v^2}$ components. Again slightly higher values of $\overline{v^2}/\overline{u^2}$ are observed for the large rib separation (*p/k* = 18).

In Figure V-13, distributions of the correlation coefficient ($\rho_{uv} = -\overline{uv}/(\overline{u^2}\,\overline{v^2})^{1/2}$) at different depths are shown on top of the rib and in the middle of the cavity for *p/k* = 9 and 18, respectively. On top of the rib (Figures V−13a and c) a maximum of ρ_{uv} is observed at y/d < 0.2 which coincide with the maximum of the Reynolds shear stress profiles shown in Figures V–3a and 3c. With increasing distance from the roughness (*y/d* > 0.2), ρ_{uv} decays without apparent dependence on the flow depth. In the middle of the cavity (Figures V−13b 13d and 13e) a higher values of ρ_{uv} are obtained near the rib crests. The correlation coefficient is reduced in the most of the outer layer due to the proportionately larger increase of the $\overline{u^2}^{1/2}$ and $\overline{v^2}^{1/2}$ as seen from Figures V−12b, 12d and 12e. In Figure V-13, profiles of ρ_{uv} do not depend on the depth of flow.

Finally, in Figure V-14 the component of the Reynolds stress anisotropy tensor b_{ij} are documented at different flow depths for p/k =9 and 18, respectively. For comparison the DNS data by Leonardi (2002) at p/k = 8 are also included. In Figures V−14a and 14c, b_{11} and b_{22} components are affected at the shallow depth. At large p/k = 18, the effect of the depth is the strongest on the top of the roughness and affects most of the outer layer. The results obtained from the Reynolds stress anisotropy tensor are similar to the results of the previous discussion on the stress ratios.

5.5. Summary

The chapter presents a new set of data on turbulent flow over a long train of 2-D rectangular ribs of varying spacing in an open channel. The roughness height is $k/d < 0.15$ and it is outside the limit ($k/d \approx 0.025$) suggested by Jimenez (2004) and tested by other researchers (Schultz et al., 2005 and Flack et al, 2007). In hydraulic engineering, this is equivalent to the rough open channel flow with intermediate submergence ($6 < d/k < 10$) as defined by Nikora et al., (2001). Three depths of flow at two different rib separations of 9 and 18, under the classification of k-type roughness were examined. Mean velocities and various turbulent quantities were measured using the 2-D LDV system at normalized streamwise distance of x^+ = 356 x 10^3 and x^+ = 340 x 10^3 for p/k = 9 and *18*, respectively. The measurement stations provide for x^+ values which are significantly greater than that used in previous studies. The experiments reported in this chapter, complement previous research on open channel flow and are particularly important since they fall in the transitional category between the narrow and wide channels with aspect ratio of $6 < b/d < 10$ with large distributed bed roughness with intermediate submergence of $6 < d/k < 10$. Information herein is particularly significant for modeling purposes since it presents local variations of the turbulent quantities without any spatial averaging.

The mean velocity distributions for the two rib separations shows that on the top of the rib all profiles collapse on to a single line in the outer region. Near the bed, local effect of the ribs result in the formation of a small recirculation zone associated with a separating shear layer. On top of the rib, these local effects are absent at vertical locations $y_1/d > 0.3$. On the section between consecutive ribs, no effect of the local flow separation is noticed for both p/k ratios. While on the top of the rib, the velocity distributions in the outer layer do not depend on depth, in the mid-cavity section, a vertical variation is observed with no apparent trend with depth. Inside the rib enclosure, linear velocity profiles are obtained and their slopes depend on the roughness spacing. This is consistent with the observations of Coleman et al., (2007).

Turbulence intensities do not conform to the wall similarity hypothesis and are found to depend on the depth of flow and p/k ratio. On the top of the rib, the highest turbulent intensity is obtained for all cases near the rib crests in the region where the shear layer develops. Outside the shear layer, the turbulent intensities are small. Inside the cavity, the peak of the turbulence intensity still remains near the rib crests but it is less intensive. While at large $p/k = 18$, inside the cavity, all profiles attain maximum value independent of the flow depths, for $p/k = 9$ the maximum value depends on the depth of flow. In the outer region, the turbulent intensities slowly decay and near the free surface attain constant values. The magnitude of the constant value is more dependent on the flow depth for *p/k* = 9. For p/k = 9, higher turbulent intensities are obtained at the shallow depth in the outer region. The turbulent intensities at large p/k ratio are less affected by the change of the flow depth.

Inspection of the Reynolds shear stress shows that at lower depths, there is an increased levels of turbulence and higher values of Reynolds shear stress are noted for *p/k* = 9. For all rough profiles, the Reynolds stress attain maximum inside the rib enclosure. Further away, at the plane of the rib crests the Reynolds shear stress profiles decay and depend on the flow depth.

Conditional quadrant analysis also reveals the effect of depth on the flow over a train of ribs. Based on the present data, the turbulence structures are affected by both the large roughness and flow depth. The effect of the roughness on the turbulent structures becomes less obvious in the deep-flow case whereas at the shallow depth, large roughness control the flow. For the threshold value H = 0, stress fractions from ejections and sweeps contribute the most to the total Reynolds shear stress and they increase near the free surface. At shallow depth this increase seems to depend on the *p/k* ratio. The probability of occurrence show a shift from sweep to ejection dominated flow at H = 2. At H = 2, the similarity between the rough and smooth wall data is high at larger depths. At shallow depth, the stress fractions and the probability of occurrence of strong ejections and sweeps consistently deviate from the ones obtained on the smooth bed. For the rough shallow case the values of $(uv)_{Q_4}/(uv)_{Q_2}$ are very different from those obtained on the smooth bed, while for the large depth this difference diminishes in the outer region where the turbulent structures becomes similar to those on the smooth bed.

The components of the Reynolds stress anisotropy tensor of rough wall open channel flow at fixed depth of d = 0.10m are in line with the previous experimental study on turbulent boundary layers of Shafi and Antonia (1995), Djenidi et al., (2007) and the numerical simulations of Leonardi et al., (2006). For the case of the present large, distributed roughness, the roughness separation (p/k) does influence the turbulence characteristics outside the roughness sublayer. Generally, a lower level of anisotropy is attained for d- and k- type roughness conditions compared to the smooth case. Structural differences are observed in the turbulence anisotropy between the p/k = 9 and 18. At y_1/d < 0.2, higher level of isotropic turbulence is noticed for p/k = 18, than that noted for p/k = 9. This tendency persists not only on top of the rib but also within the roughness cavity. Inside the cavity, similar level of turbulence anisotropy is observed for p/k = 9 and 4.5, which suggests that the flow is independent of the roughness density. As the rib separation increases, fewer ribs are present upstream and their effect is felt not only on the top of the roughness but also above the roughness cavity. The effect of the roughness density becomes important at large p/k = 18 which implies that at this roughness conditions the mechanism of energy transfer between the individual components of turbulent kinetic energy is different from that of p/k = 9, 4.5 and the smooth wall.

The effect of the flow depth is more noticeable at large p/k =18 on the top of the roughness where the stress ratios and the components of the Reynolds stress tensor (b_{ij}) show that turbulence tends to be more isotropic at shallow depth. At large p/k = 18 and at shallow depth, combined effect of the roughness (*p/k*) and the submergence (*d/k*) become important.

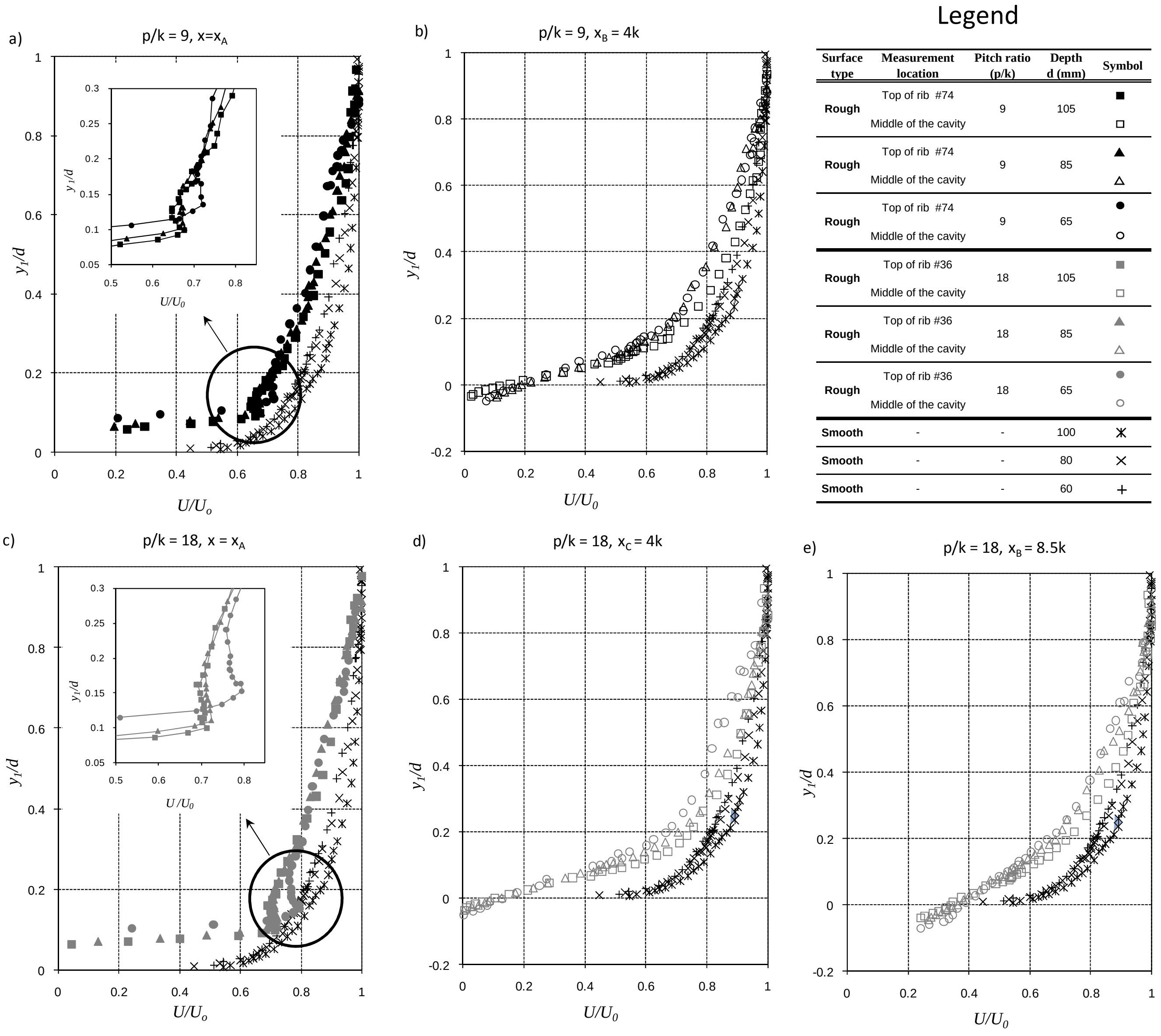

Legend

Surface type	Measurement location	Pitch ratio (p/k)	Depth d (mm)	Symbol
Rough	Top of rib #74 Middle of the cavity	9	105	■ □
Rough	Top of rib #74 Middle of the cavity	9	85	▲ △
Rough	Top of rib #74 Middle of the cavity	9	65	● ○
Rough	Top of rib #36 Middle of the cavity	18	105	■ □
Rough	Top of rib #36 Middle of the cavity	18	85	▲ △
Rough	Top of rib #36 Middle of the cavity	18	65	● ○
Smooth	-	-	100	✳
Smooth	-	-	80	×
Smooth	-	-	60	+

Figure V-1. Outer scaling of the mean velocity: (a) and (c) *at the rib crest*[1]; (b) and (e) *in the middle of the cavity* for *p/k* = 9 and *p/k* = 18; (d) is located at *x = 4k* from the back edge of the rib for *p/k* = 18.

---

[1] In all figures, reference location y_1 is taken at the mean elevation of the roughness.

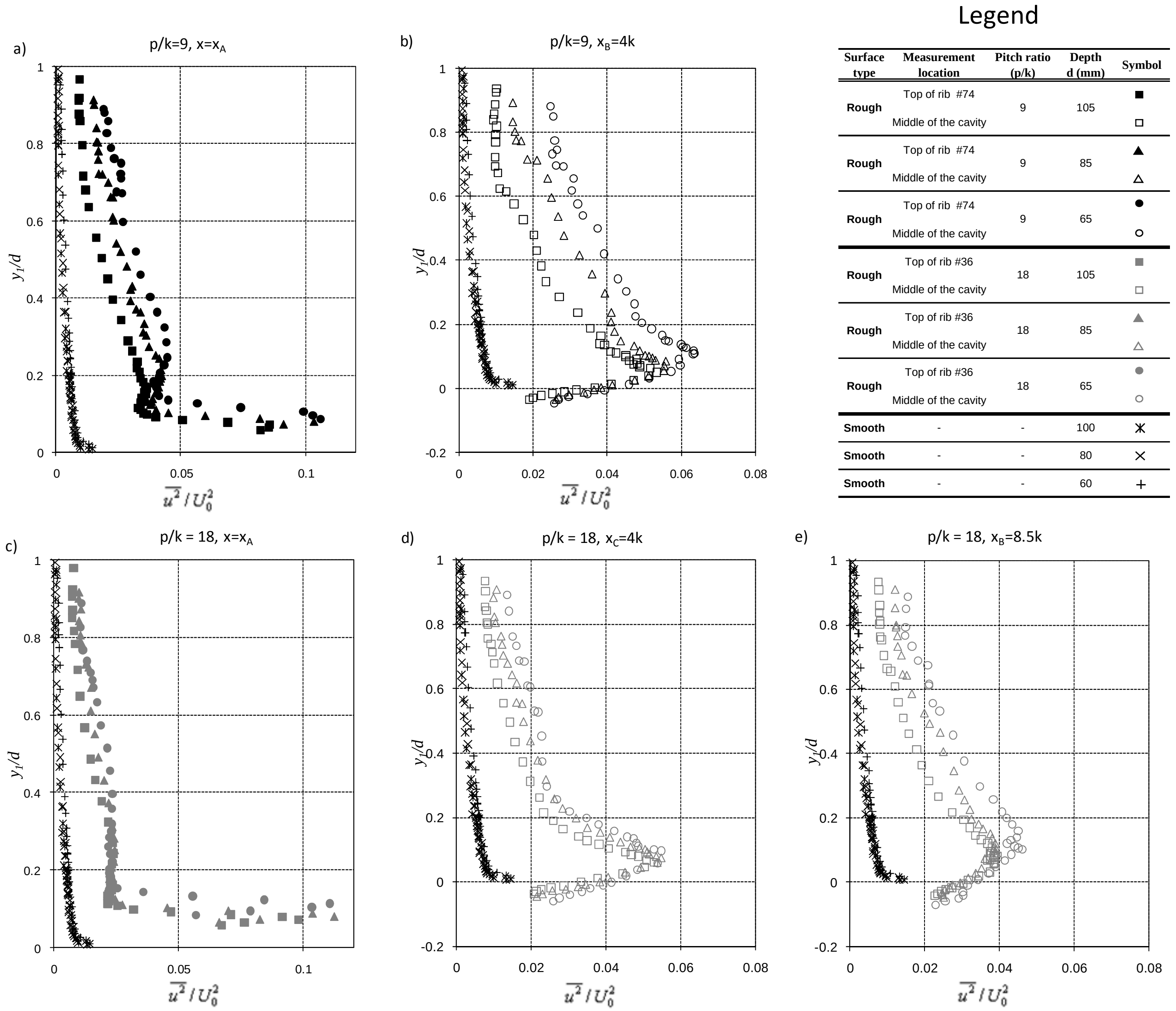

Figure V-2. Outer scaling of the streamwise turbulent intensity ($\overline{u^2}$): (a) and (c) *at the rib crest*; (b) and (e) *in the middle of the cavity* for *p/k* = 9 and *p/k* = 18; (d) is located at *x* = *4k* from the trailing edge of the rib for *p/k* = 18.

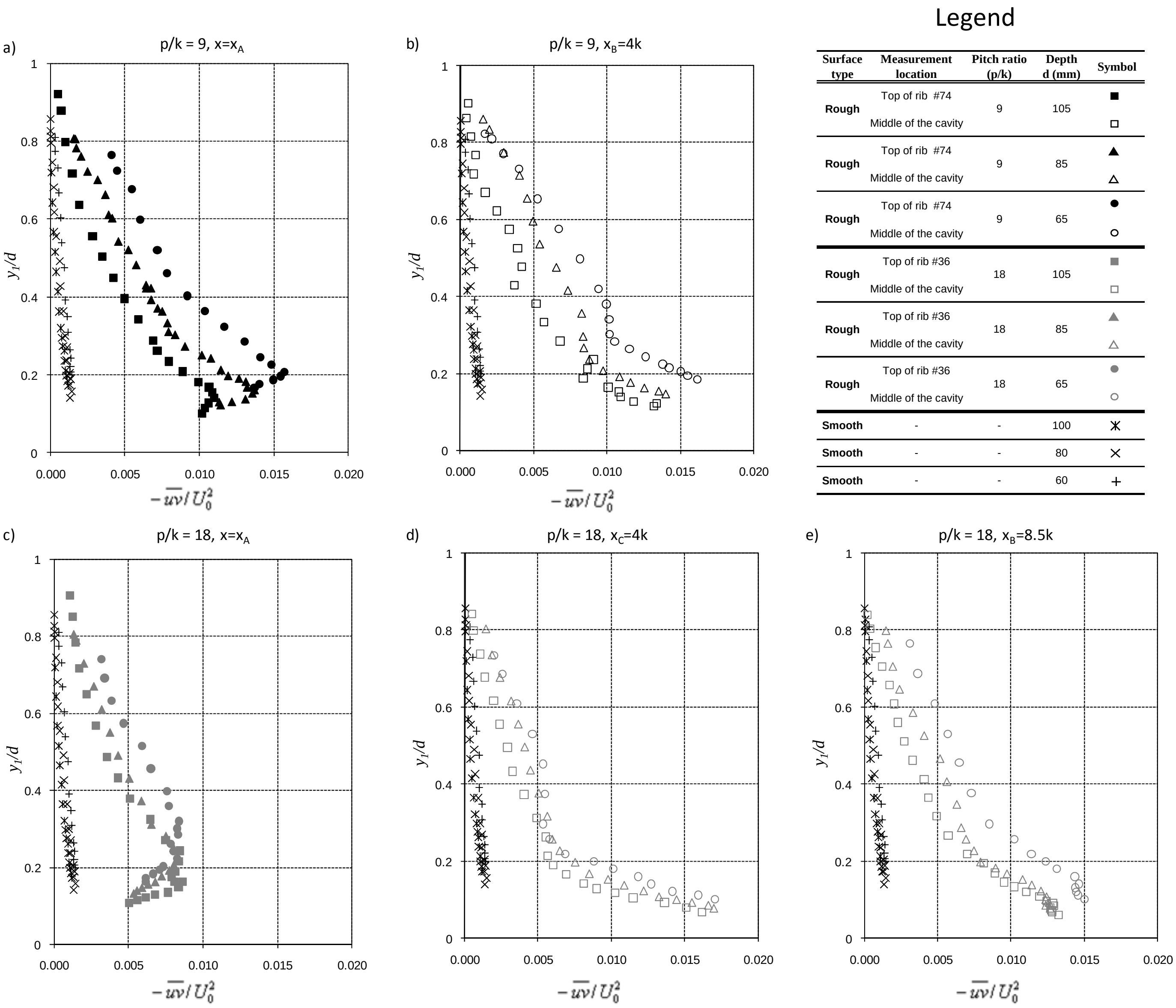

Figure V-3. Outer scaling of the Reynolds shear stress ($-\overline{uv}$): (a) and (c) *at the rib crest;* and (b), (d) and (e) *in the middle of the cavity* for *p/k*=9 and *p/k*=18; (d) is located at *x = 4k* from the trailing edge of the rib for *p/k* = 18.

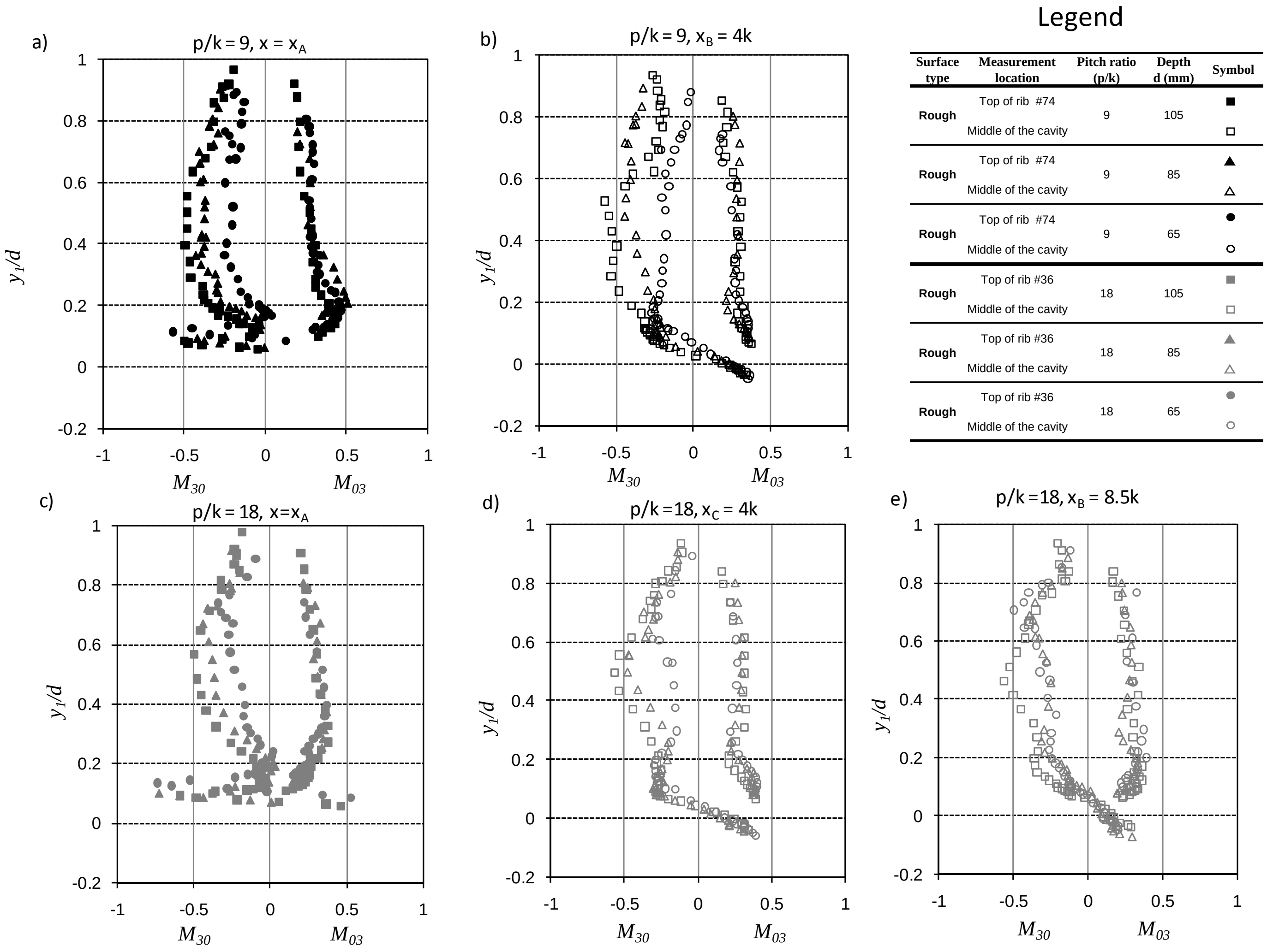

Surface type	Measurement location	Pitch ratio (p/k)	Depth d (mm)	Symbol
Rough	Top of rib #74	9	105	■
	Middle of the cavity			□
Rough	Top of rib #74	9	85	▲
	Middle of the cavity			△
Rough	Top of rib #74	9	65	●
	Middle of the cavity			○
Rough	Top of rib #36	18	105	■
	Middle of the cavity			□
Rough	Top of rib #36	18	85	▲
	Middle of the cavity			△
Rough	Top of rib #36	18	65	●
	Middle of the cavity			○

Figure V-4. Skewness factors $M_{30} = \overline{u^3} / u_{rms}{}^3$ and $M_{03} = \overline{v^3} / v_{rms}{}^3$: (a) and (c) *at the rib crest* and (b), (d) and (e) *in the middle of the cavity* for *p/k* = 9 and *p/k* = 18.

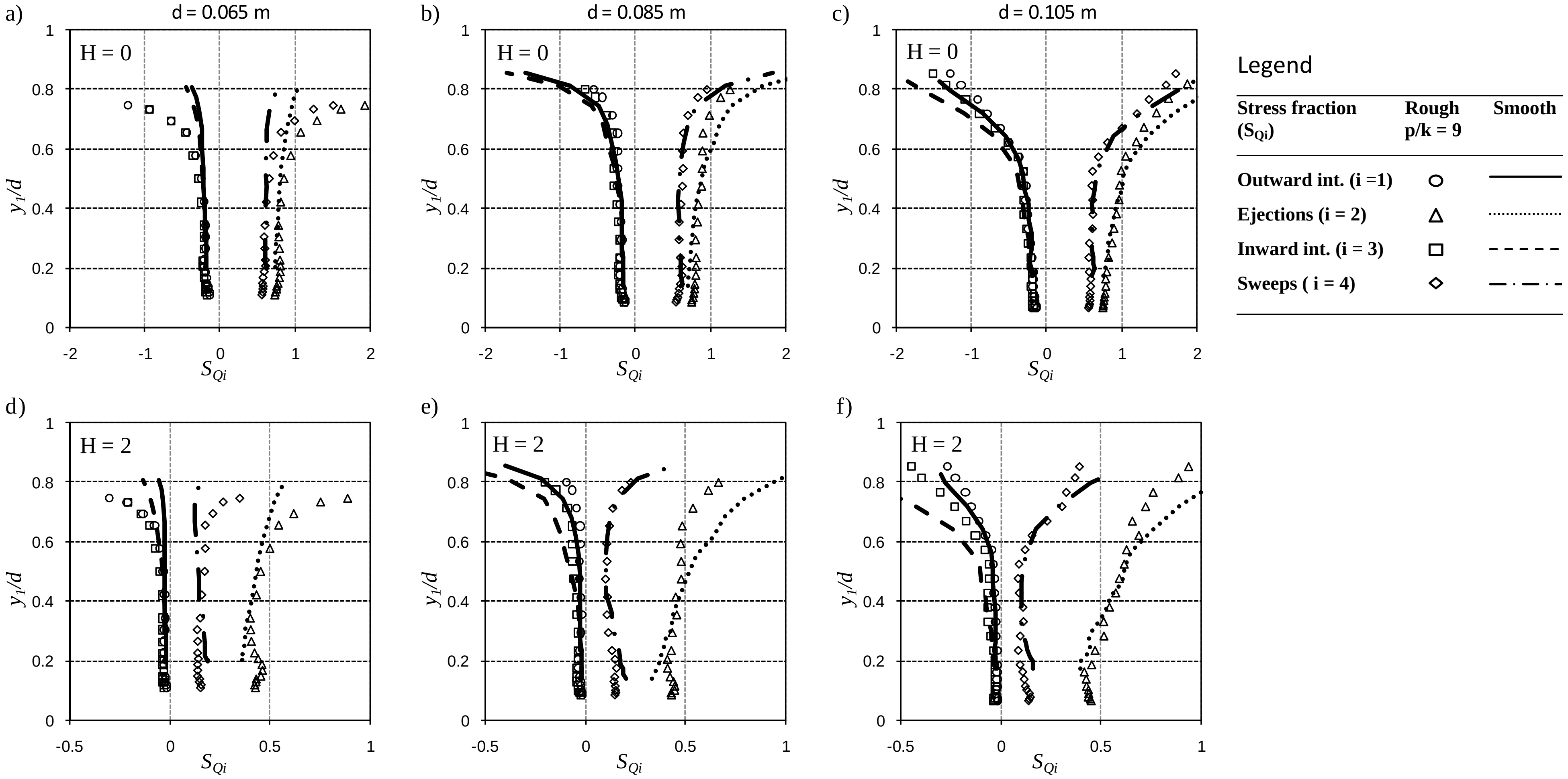

Figure V-5. Stress fractions vs. wall normal position for *p/k* = 9 at d = 0.065 m, 0.085 m and 0.105 m for H = 0 (first row) and H = 2 (second row) measured *in the middle of the cavity*.

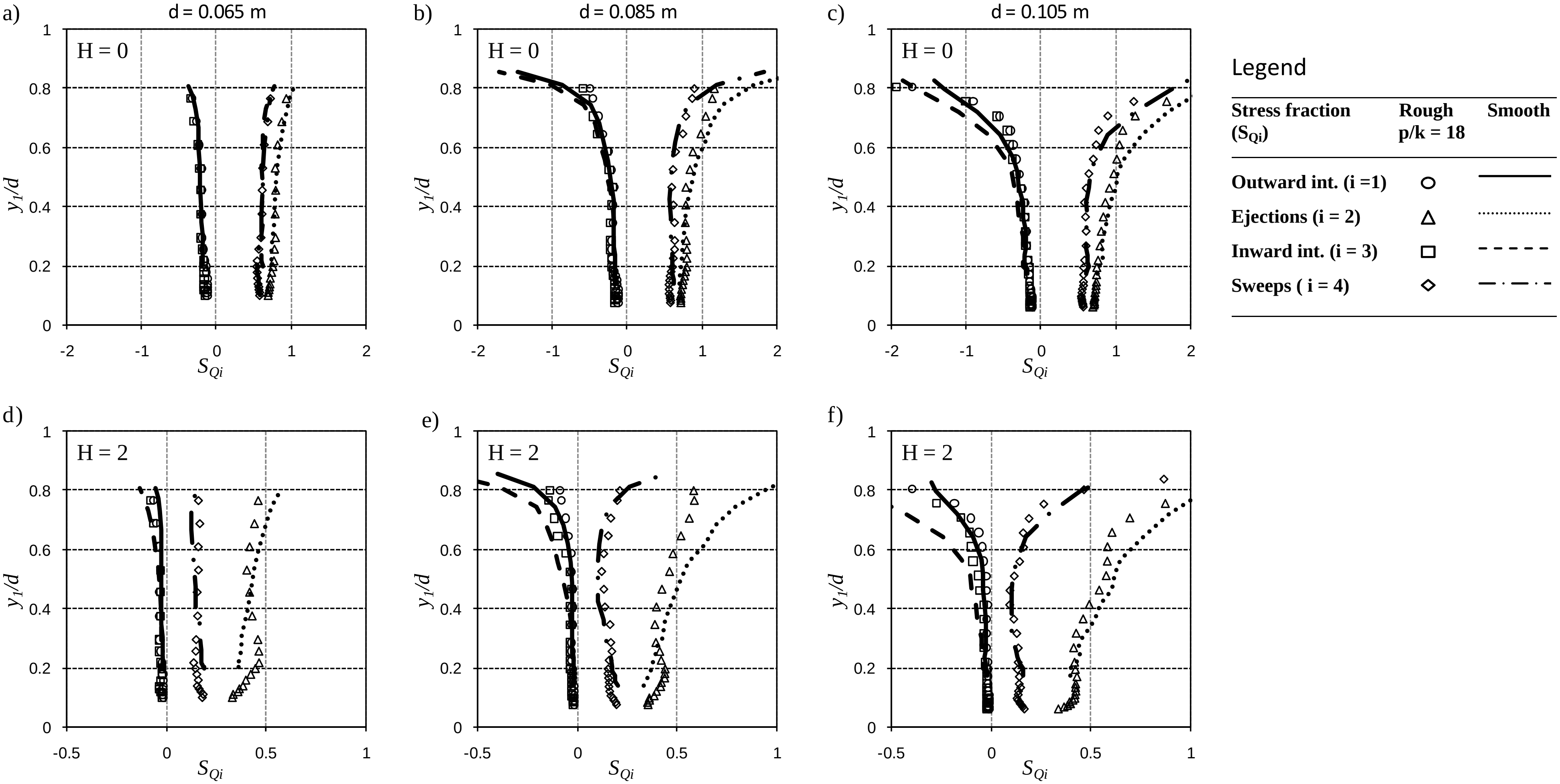

Figure V-6. Stress fractions vs. wall normal position for *p/k* = 18 at *d* = 0.065 m, 0.085 m and 0.105 m for H = 0 (first row) and H = 2 (second row) measured *in the middle of the cavity*.

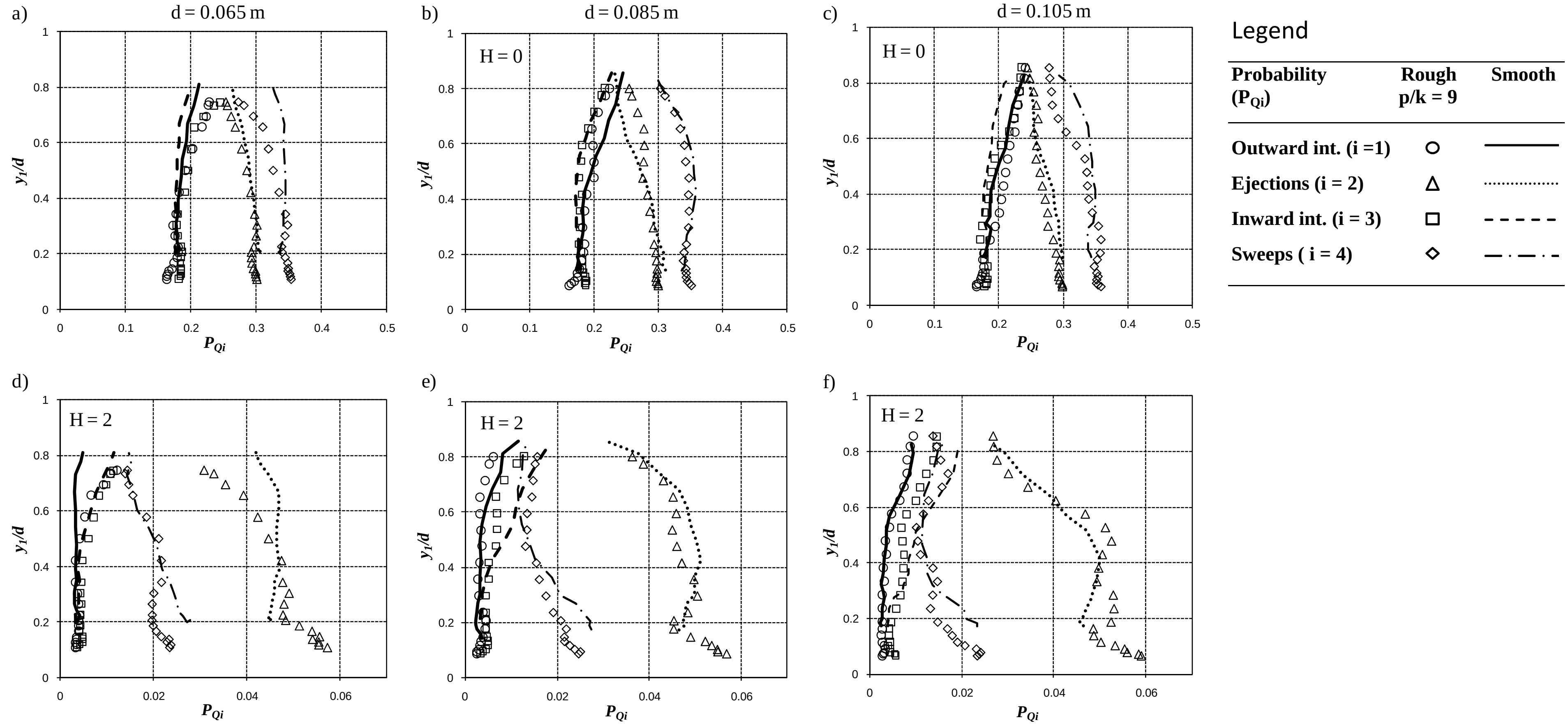

Figure V-7. Occurrence probability (P_{Qi}) of event types in each quadrant for *p/k* = 9 at d = 0.065, 0.085 and 0.105 m for H = 0 (first row) and H = 2 (second row) measured *in the middle of the cavity*.

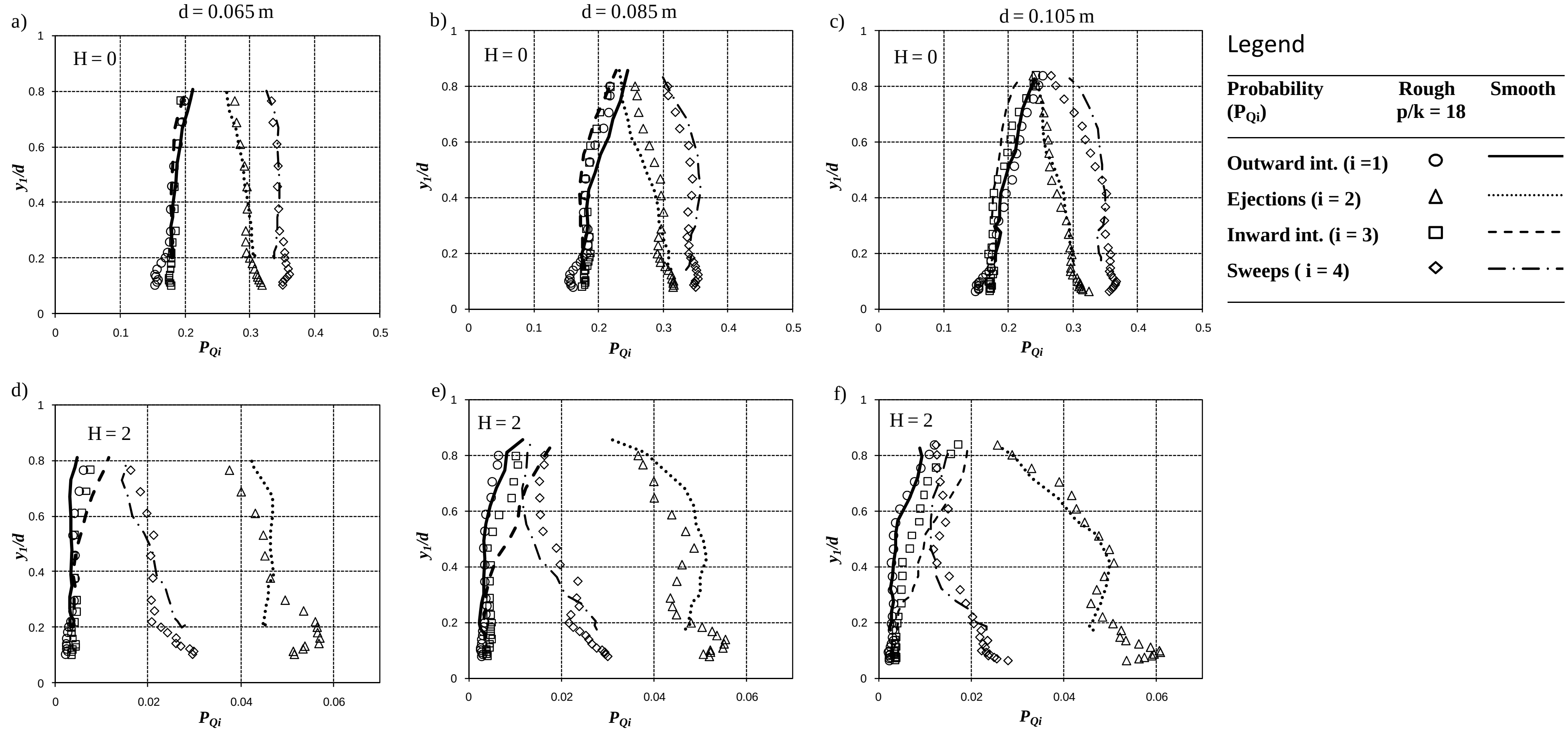

Figure V-8. Occurrence probability (P_{Qi}) of event types in each quadrant for *p/k* = 18 at *d* = 0.065 m, 0.085 m and 0.105 m for H = 0 (first row) and H = 2 (second row) measured *in the middle of the cavity*.

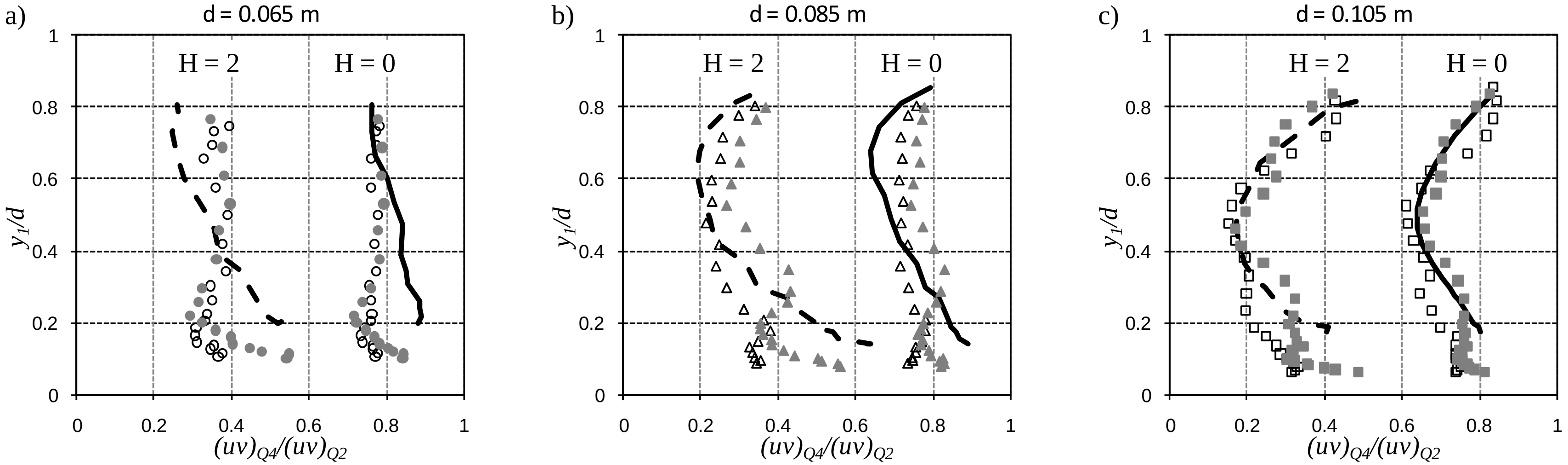

Figure V-9. Ratio between the sweep and ejection events for H = 0 and H = 2 calculated *in the middle of the cavity* for *p/k*=9 (open symbols) and *p/k*=18 (solid symbols). Lines represent *$(uv)_{Q4}/(uv)_{Q2}$* ratios for the smooth wall data.

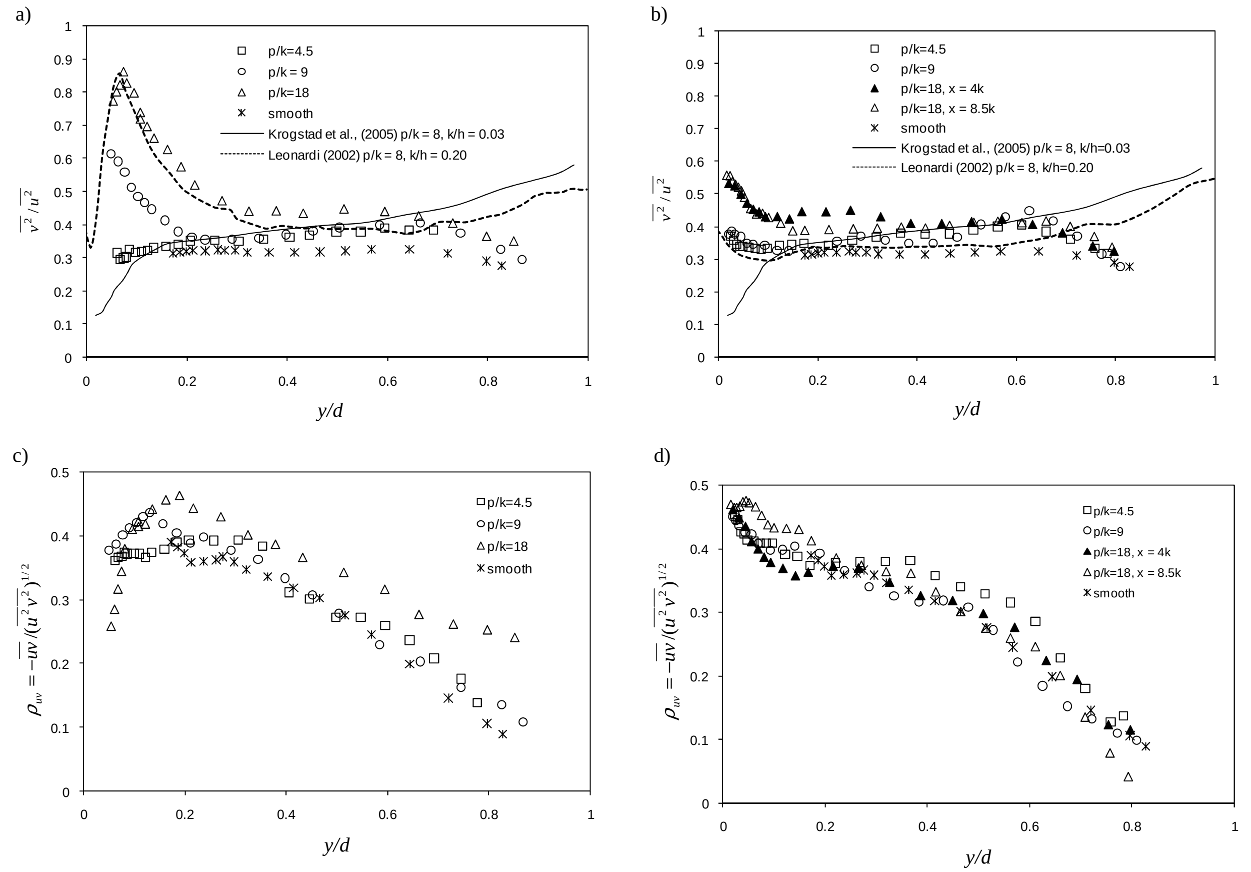

Figure V-10. Stress ratio $\overline{v^2}/\overline{u^2}$, (a) and coefficient of correlation $\rho_{uv} = -\overline{uv}/(\overline{u^2}\,\overline{v^2})^{1/2}$, (c) on the top of the rib and (b) and (d) in the middle of the roughness cavity, respectively.

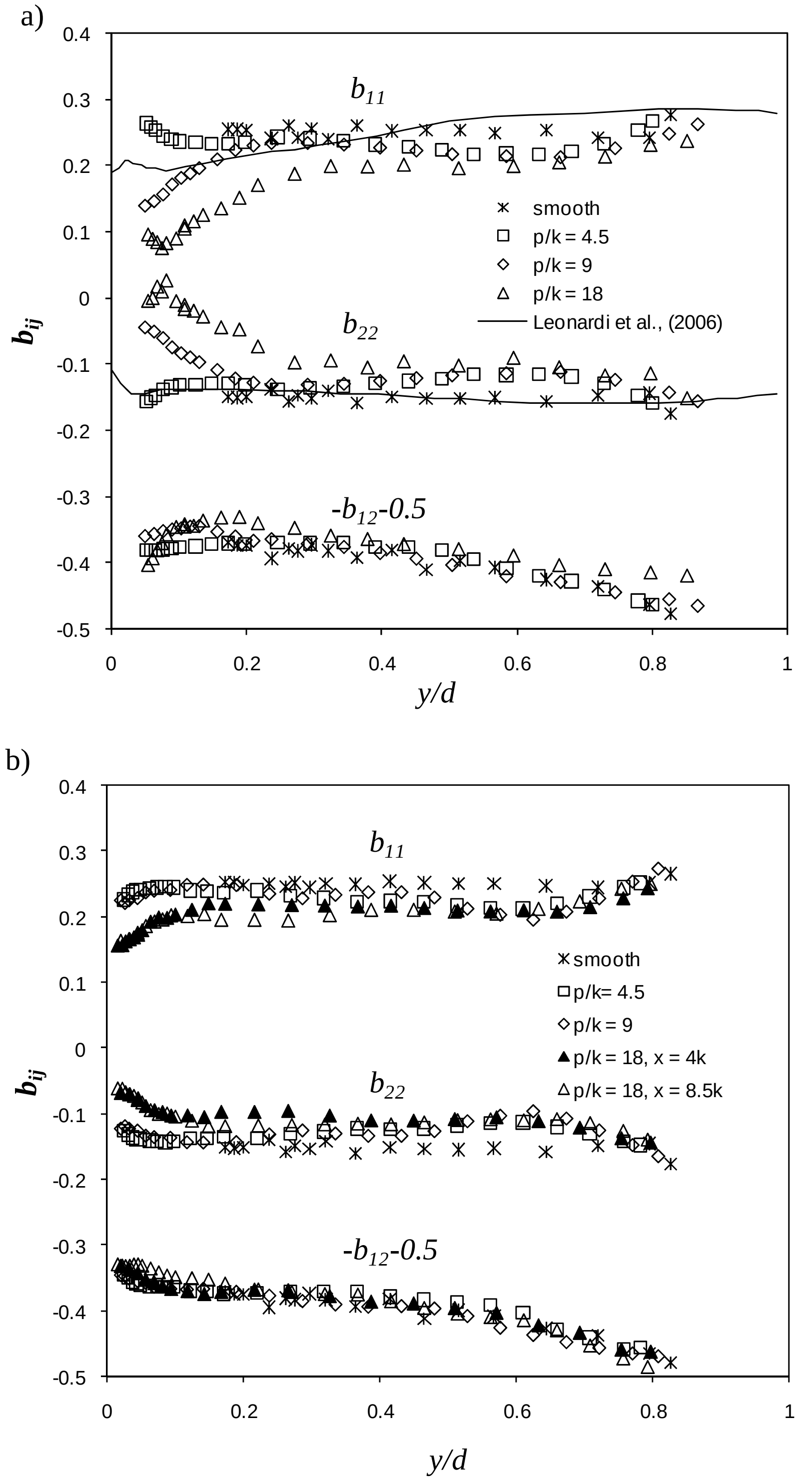

Figure V-11. Components of the Reynolds stress anisotropy tensor (b_{ij}): (a) on the top of the rib and (b) in the middle of the roughness cavity. The solid lines represent the DNS calculations by Leonardi et al., (2006) for *p/k* = 8.

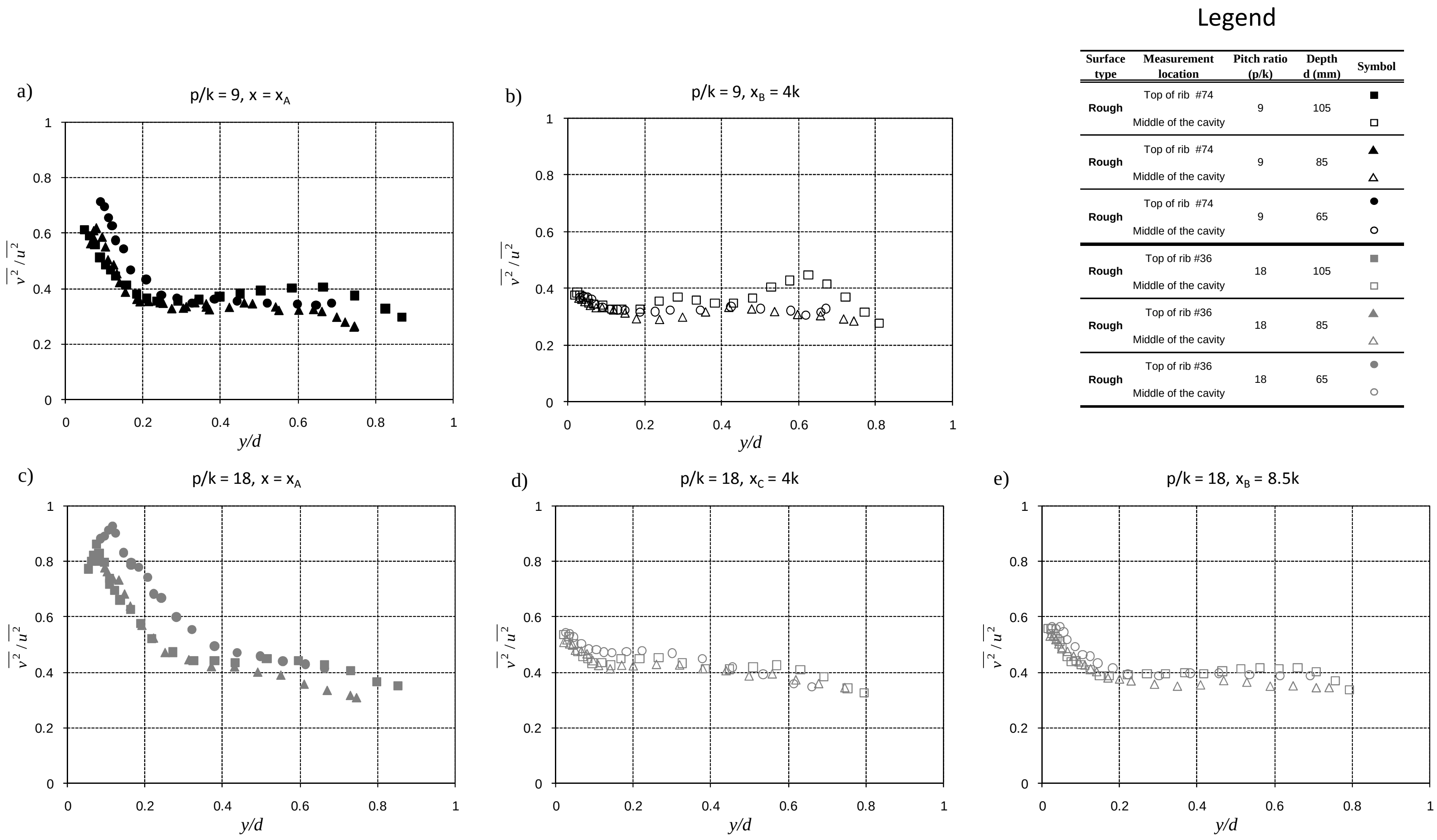

Figure V-12. Stress ratios $\overline{v^2}/\overline{u^2}$ (a) and (c) *at the rib crest* and (b), (d) and (e) *in the middle of the cavity* for p/k = 9 and p/k = 18.

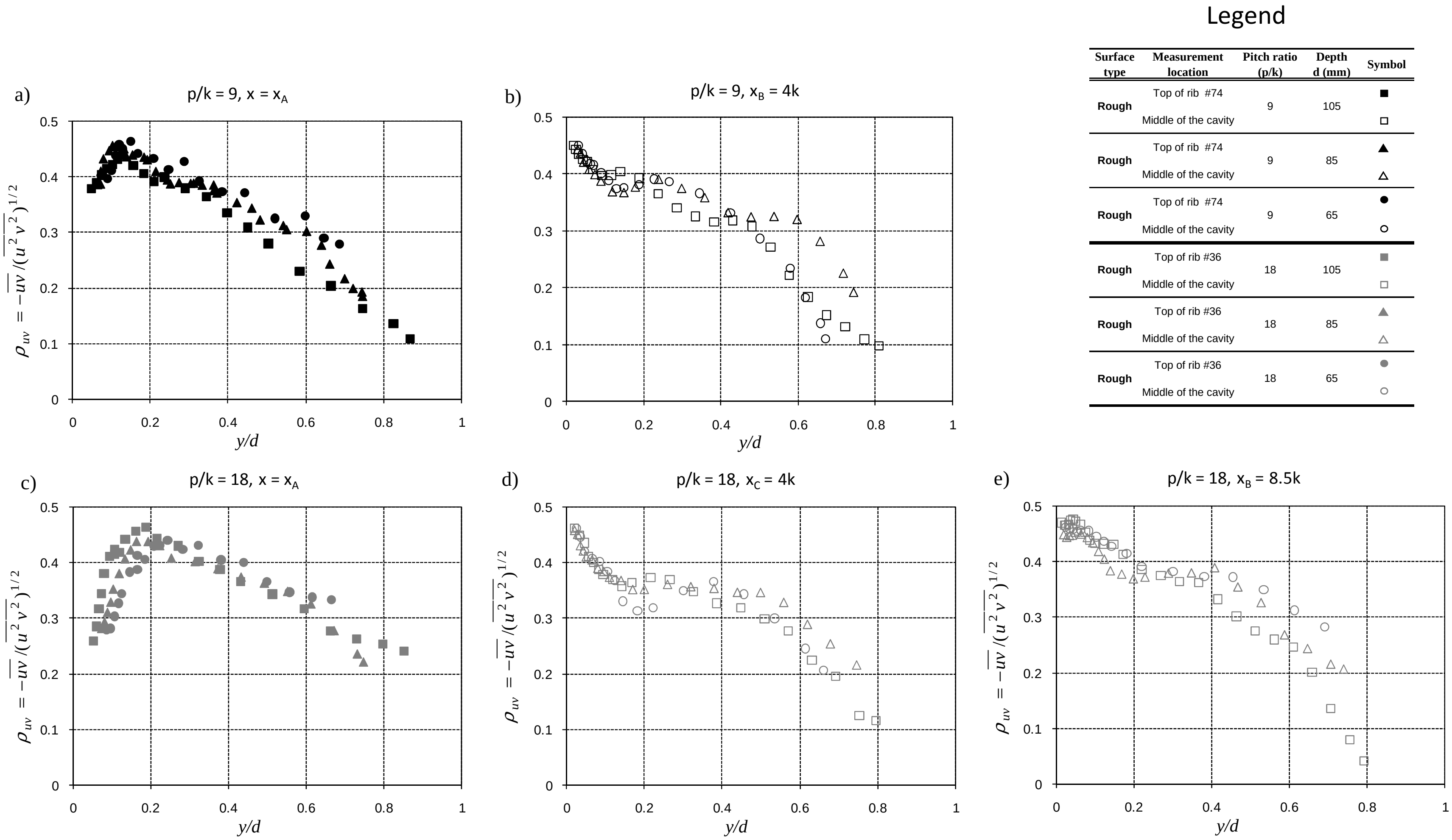

Surface type	Measurement location	Pitch ratio (p/k)	Depth d (mm)	Symbol
Rough	Top of rib #74	9	105	■
	Middle of the cavity			□
Rough	Top of rib #74	9	85	▲
	Middle of the cavity			△
Rough	Top of rib #74	9	65	●
	Middle of the cavity			○
Rough	Top of rib #36	18	105	■
	Middle of the cavity			□
Rough	Top of rib #36	18	85	▲
	Middle of the cavity			△
Rough	Top of rib #36	18	65	●
	Middle of the cavity			○

Figure V-13. Correlation coefficients $\rho_{uv} = -\overline{uv}/(\overline{u^2}\,\overline{v^2})^{1/2}$ (a) and (c) *at the rib crest* and (b), (d) and (e) *in the middle of the cavity* for *p/k* = 9 and *p/k* = 18.

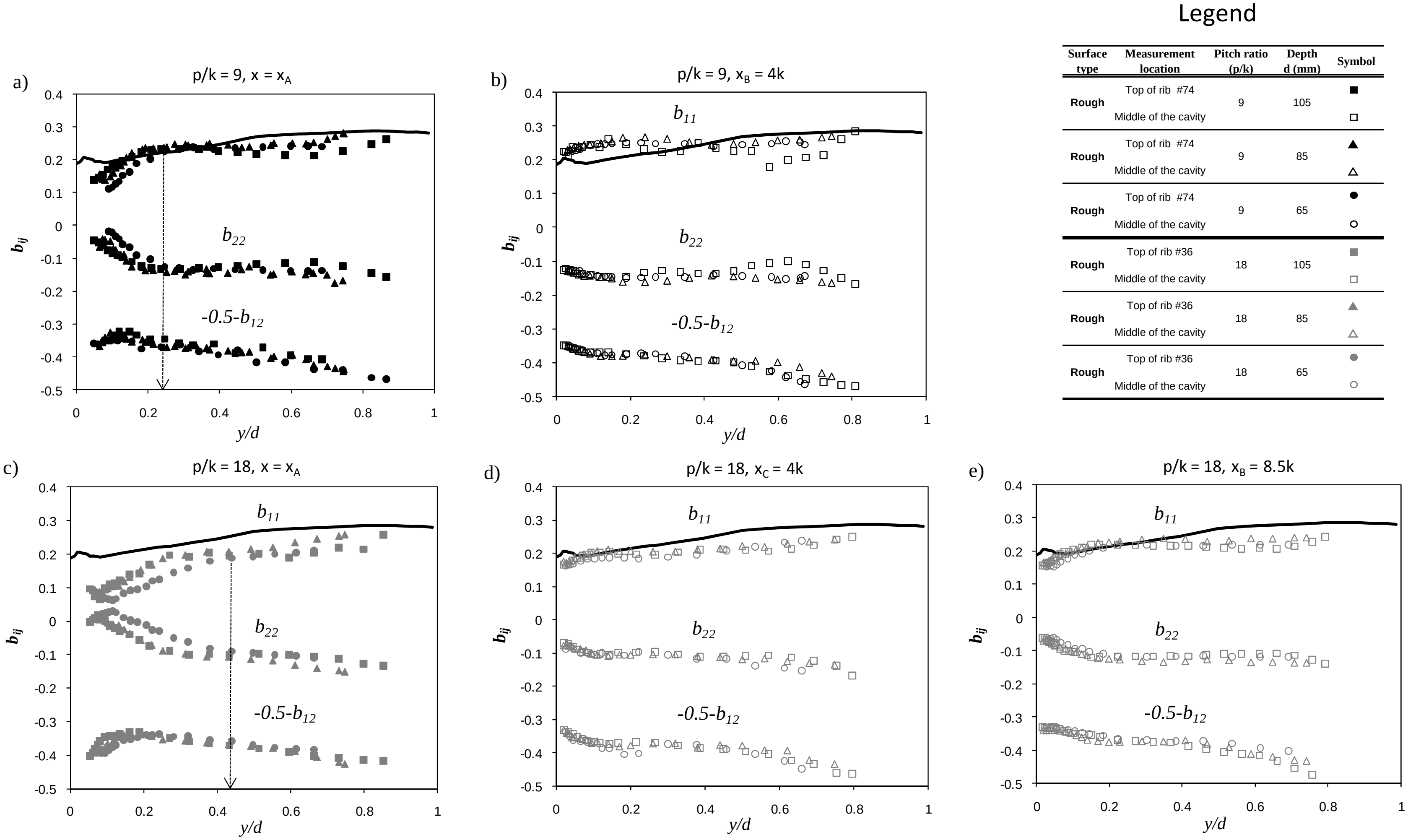

Surface type	Measurement location	Pitch ratio (p/k)	Depth d (mm)	Symbol
Rough	Top of rib #74 Middle of the cavity	9	105	■ □
Rough	Top of rib #74 Middle of the cavity	9	85	▲ △
Rough	Top of rib #74 Middle of the cavity	9	65	● ○
Rough	Top of rib #36 Middle of the cavity	18	105	■ □
Rough	Top of rib #36 Middle of the cavity	18	85	▲ △
Rough	Top of rib #36 Middle of the cavity	18	65	● ○

Figure V-14. Components of the Reynolds stress anisotropy tensor (b_{ij}) (a) and (c) *at the rib crest* and (b), (d) and (e) *in the middle of the cavity* for *p/k* = 9 and *p/k* = 18.

CHAPTER

VI. CONCLUSIONS, CONTRIBUTIONS AND FURURE RECOMENDATIONS

The conclusions from the present research are enumerated in detail within the individual chapters (Chapters III, IV and V). Here, the main conclusions are briefly reviewed and suggestions for the future research are also presented.

6.1. Smooth open channel flow

In the present thesis, an attempt has been made to gain an understanding of the nature and characteristics of the turbulent structures in open channel flow, and in particular, the effect of the flow depth. Open channel flows are unique because they are bounded by side walls and by the free surface. While shallow flows are entirely dominated by the wall turbulence, deep open channel flows in many respects could be similar to the turbulent boundary layers since they are developing in an unbound domain. There is no a clear quantitative demarcation between shallow and deep open channel flows. In general, open channels flows are classified by inspecting the channel aspect ratio (= b/d) which accounts for the effect of the side walls. Smooth open channels are classified as narrow if *b/d* < 5 and wide if *b/d* > 10 (Nezu and Nakagawa 1993). The boundary of this classification is rather arbitrary since shallow flow conditions can exists in narrow channels and conversely deep flow conditions can exist in wide channels. To study the effect of the flow depth, the approach used in this thesis was to keep the Reynolds number ($Re_d = \frac{dU_0}{\nu}$) above 20,000 to avoid any low-Reynolds number effects. Due to the limitation of the water flume, all experiments were conducted in a channel with fixed width (*b*) while the depth of flow and the flow velocities were adjusted by tilting the slope of the flume. One of the recommendations for future experiments will be to design a flexible water flume in which it will be is possible to adjust the width of the channel while keeping the depth of flow and the Reynolds number constant. All smooth and rough experiments analysed in this thesis were conducted at intermediate channel aspect ratios $6 < b/d < 10$ where the link between the near-wall turbulence and the free–surface turbulence is particularly important.

Measurements were obtained with laser Doppler velocimetrey (LDV) and particle image velocimetry (PIV) techniques throughout the depth. While LDV provides a point measurement, the PIV generates 2-D velocity maps in a plane. Here, the PIV velocity fields at the streamwise-wall normal (x-y) plane are analysed.

Careful inspection of the velocity scaling in the outer layer of smooth open channel flow at three different flow depths revealed a combined effect of the free surface and channel geometry. An increase of streamwise turbulent intensities near the free surface was observed for the deep flow cases (at small aspect ratios $b/d < 7.5$) and negative values for the wake parameter were calculated. At larger depths, the free surface behaves as a “weak wall” affecting the normal turbulent fluctuations and it can drive the secondary recirculation. To correct for this effect, a modified length scale has been proposed based on the region of constant turbulent intensity observed near the free surface. It was verified that the new length scale provides a better description not only for the mean velocity profiles but also for the higher-order turbulent statistics and correlation coefficient. With the use of this new length scale, the estimation of the wake parameter becomes positive and provides for a more accurate estimate of the friction velocity.

The quadrant analysis shows that when all turbulent events are included (H = 0), the turbulence structure in the outer layer of open channel flow is similar to that of turbulent boundary layers and two-dimensional channels. Very different results are obtained at higher threshold values where near the free surface an increase in Q1 and Q3 events are observed which are responsible for the negative production. At the shallow depth, the distribution of the ratio of Q2/Q4 is more spread out and the turbulence kinetic energy is more evenly distributed among the three components implying that turbulence tends to be more isotropic. This was further confirmed from the analysis of the components of the Reynolds stress anisotropy tensor. Conversely, at larger depths, the turbulence conditions become anisotropic which could affect the momentum transfer. An increase in the value of correlation coefficient was observed at shallow depth which shows an increase of the turbulence level that might affect the flow resistance.

More insights related to the organization of the turbulent structures in smooth open channel at d = 0.10 m (deep flow case) and Re = 21,000 are revealed from the PIV measurements in the (x-y) plane. The techniques chosen for analysis of the instantaneous velocity fields include proper orthogonal decomposition (POD), swirling strength analysis, momentum analysis and conditional quadrant analysis. POD and swirling strength techniques revealed the existence of vortices of different sizes and energy levels. In the outer layer, large-scale vortices similar to the signatures of the hairpin packets (Adrian et al., 2000) are found. The large-scale energy containing structures obtained from the POD reconstructed velocity fields are elongated and inclined in the streamwise direction. These large scale structures contained 50% of the kinetic energy since they are obtained from the inclusion of the first 12 POD modes in the velocity reconstruction.

Only large-scale eddies that are smaller than the size of the field-of-view (= 0.1 m) are identified. In some instances, close to the free surface ($y/d > 0.7$), signatures of hairpin vortices with legs possibly attached to the free surface are obtained. This implies that the free surface behaves as a "weak wall" at d = 0.10 m. The presence of these large-scale structures near the free surface caused the fluid particles to be displaced into the fluid, creating nearly parallel flow patterns with long negative u- fluctuations identified from the zones of the uniform momentum. The boundaries of the uniform momentum zones overlap well with the locations of the heads of the hairpin vortices identified from the swirling strength. This validates the existence of the organized aligned packets of hairpin vortices in the outer-layer of open channel flow similarly to the one observed in boundary layers flow. It was also observed that some of the momentum zones reappeared near the free surface. The PDF distributions of the swirling strength show that more prograde vortices are observed near the bed. This result is again consistent with the vortex population trends observed in the turbulent boundary layers (Wu and Christensen, 2006). Near the free surface, an increase of the retrograde vortices is observed highlighting the influence of the free surface. This implies that the interaction between the free surface and the turbulent structures is rather weak and some of the turbulent structures are returned back into the flow. Perhaps, this mechanism could explain the increase of the Q3 and Q1 events observed near the free surface. For the deep flow case, open channel flow near the bed in many respects can be considered similar to the turbulent boundary layers. Analysis of the instantaneous Reynolds shear stress revealed patterns of strong ejection and sweep events which are common features of all wall-bounded flows.

6.2. Rough open channel flow

Nearly all flows in hydraulic engineering are rough, i.e., roughness elements protrude through the viscous sublayer into the turbulent region. Vertical distributions of the velocity and other turbulence statistics differ significantly from those over a smooth bed since the nature of the drag is significantly different when roughness elements are present. The relationship between the roughness geometry and the effect of the roughness on mean velocity and turbulence is still to be found.

A new set of data on turbulent flow over a long train of 2-D rectangular ribs of varying spacing in an open channel has been analysed. The roughness height was large $k/d < 0.15$ and it is outside the limit for valid wall similarity suggested by Jimenez (2004) and tested by other researchers (Schultz et al., 2005 and Flack et al., 2007). In hydraulic engineering, this is equivalent to the rough open channel flow with intermediate submergence ($6 < d/k < 10$) as defined by Nikora et al., (2001). Three depths of flow at three different rib separations of 4.5, 9 and 18, under the classification of d- and k-types roughness were examined. The present results provide detailed evidence that both roughness and flow depth can have an effect on the turbulent structures at shallow flow conditions. While the direct effect of the roughness on the mean velocity is only seen locally (in the vicinity of the roughness) turbulence intensities, Reynolds shear stress and higher order moments do not conform to the established wall similarity hypothesis and are affected throughout the outer layer. Compared to the smooth wall data, magnitudes of all turbulence quantities are much higher which is a direct result from the presence of rough wall.

Based on the results from the quadrant analysis, turbulent structures are also affected by both the roughness and flow depth. For the shallow rough bed case, the ratio of the shear contribution of sweep to ejection events is very different from that obtained on the smooth bed. For the deep flow cases, this difference diminishes in the outer region. Thus, the effect of the roughness on the turbulent structures becomes less obvious in the deep-flow case whereas at the shallow depth, large roughness control the flow.

The components of the Reynolds stress anisotropy tensor on rough wall open channel flow are in line with the previous experimental study on turbulent boundary layers of Shafi and Antonia (1995), Djenidi et al., (2007) and the numerical simulations of Leonardi et al., (2006). Generally, a lower level of anisotropy is attained for d- and k-type roughness conditions at the fixed d = 0.10 m compared to the smooth case. Structural differences are observed in the Reynolds stress anisotropy between p/k = 9 and 18. At large p/k = 18 the effect of the roughness density becomes important which suggests that the mechanism of energy transfer between the individual components of turbulent kinetic energy is different from that of p/k = 9, 4.5 and the smooth wall.

At shallow depth, both stress ratios and components of the Reynolds stress tensor (b_{ij}) show that turbulence tends to be more isotropic on the top of the rib. While at p/k = 9, the effect of the flow depth is localized in the vicinity of the roughness, at large p/k =18, this effect extends to half of the flow depth.

The rough open channel flow data presented in this thesis show that large roughness can have a global influence on the outer layer due to the wakes created by the ribs, which can be considered as bluff bodies embedded in the flow direction. Since every rib creates a local turbulent heterogeneity, the accumulation of these effects further downstream can result in flow which no longer retains the character of the classical rough turbulent boundary layer. This is especially important in the case of the sparse large roughness where many elements need to be considered. The change of the flow depth adds another dimension to the complexity of the rough flow and thus the classification of the transverse rib roughness based only on the *p/k* needs to be complemented with appropriate parameter accounting for the change of the flow depth, *d*.

6.3. Future work

Results presented in this thesis show that rough open channel flow is more complicated than the smooth wall-counterpart due to the large number of parameters associated with the roughness height, roughness density, roughness separation, roughness Reynolds number, flow depth and submergence (*d/k*). More experimental and theoretical work is needed to better understand the shallow flows developed in open channels. Recently, Nikora et al., (2001) promoted the concept of double averaging (in time and in the small volume parallel to the bed) the hydrodynamic equations. Even though this concept appears to be useful it needs to be further validated against extensive experimental data. PIV measurements seem to be more appropriate choice for applying the double averaging concept since they provide 2-D velocity fields in the plane. In addition, experiments needs to be performed over other more realistic 3-D roughness such as natural vegetation in order to create better models. Stereo PIV experiments that provide information for the three velocity components complemented with higher temporal resolution will further aid in understanding these complex flows. Particular, it will be possible to study the interaction of the free surface with the large-scale vortices at shallow flows not only in the streamwise-wall normal plane but also in the plane parallel of the flow direction.

CHAPTER

VII. REFERENCES

Adrian, R. J. (2007). “Hairpin vortex organization in wall turbulence.” *Phys. Fluids*, 19, 041301.

Adrian, R. J., Meinhart, C. D. and Tomkins, C. D. (2000). “Vortex organization in the outer region of the turbulent boundary layer.” *J. Fluid. Mech*., 422, 1-54.

Afzal, B., Faruque, MdA. A. and Balachandar, R. (2009). “Effect of Reynolds number, near-wall perturbation and turbulence on smooth open-channel flows.” *J. Hyd. Res*., 47 (1), 66-81.

Agelinchaab, M. and Tachie, M. F. (2006). ”Open channel turbulent flow over hemispherical ribs“, *Int. J. Heat Fluid Flow*, 27(6): 1010-1027.

Bakken, O.M. and Krogstad, P.-A. (2001). “Channel Flow with Surface Roughness” Proceedings of 2nd International Symposium on Turbulent Shear Flows Phenomena, Stockholm, Sweden.

Bakken, O.M., Krogstad, P.-A., Alireza, A. and Andersson, H.I. (2005). “Reynolds Number Effects in the Outer Layer of the Turbulent Flow in a Channel with Rough Walls”. *Phys. Fluids* 17(6), 1–16.

Balachandar, R. and Patel, V. C. (2005). “Velocity measurements in a developed open channel flow in the presence of an upstream perturbation”, *J. Hyd.* Res., *ASCE* 43 (3), 258-266.

Balachandar, R. and Patel, V.C. (2002). “Rough Wall Boundary Layer on a Plate in an Open Channel”. *J. Hydr. Engrg.*, ASCE 128(10), 947–951.

Bandyopadhyay, P. R., and Watson, R. D. (1988). “Structure of rough-wall turbulent boundary layers”, *Phys. Fluids,* 31 (7), 1877-1883.

Benedict, L. H., and Gould, R. D. (1996). “Towards better uncertainty estimates for turbulence statistics”. *Exp. fluids* 22 (2), 129-136.

Bergstrom, D. J., Tachie, M. F. and Balachandar, R. (2001). “Application of power laws to low Reynolds number boundary layers on smooth and rough surfaces.” *Phys. Fluids,* 13(11), 3277-3284.

Cardoso, A.H., Graf, W. H. and Gust, G. (1989). “Uniform Flow in a Smooth Open Channel.” *J. Hydr. Res*. 27(5), 603–616.

Carlier, J. and Stanislas, M. (2005). “Experimental study of eddy structures in a turbulent boundary layer using particle image velocimetry” *J. Fluid Mech.,* 535, 143–188.

Cellino, M. and Lemmin, U. (2004) “Influence of coherent flow structures on the dynamics of suspended sediment transport in open-channel flow” *J. Hydr. Engrg.,*130 (11): 1077-1088.

Christensen, K.T., and Adrian, R. J. (2001) “Statistical evidence of hairpin vortex packets in wall turbulence”. *J. Fluid Mech.,* 431 433–43

Chow, V.T. (1959). Open-Channel Hydraulics, McGraw–Hill, NewYork.

Clauser, F.H. (1956). “The Turbulent Boundary Layer”. *Adv. Appl. Mech*. 4, 1–51.

Coleman, S. E., Nikora, V. I., McLean, S. R., and Schlicke, E. (2007), “Spatially averaged turbulent flow over square ribs.” *J. Eng. Mech. ASCE,* 133 (2), 194-204.

Coles, D.E. (1956). “The Law of theWake in the Turbulent Boundary Layer”. *J. Fluid. Mech.,* 1, 191–226.

Connelly, J. S., Schultz, M. P., and Flack, K. A. (2006). “Velocity-defect scaling for turbulent boundary layers with a range of relative roughness”, *Exp. Fluids* 40 (2), 188-195.

Cordier, L. and Bergmann, M. (2002) “Proper orthogonal decomposition: an overview, Von Kármán Institute for Fluid Dynamics.” Lecture Series 2002-04 on Post-Processing of Experimental and Numerical Data, 22–26 April 2002.

Cui, J., Patel, V.C. and Lin, C.-L. (2003), “Large-eddy simulation of turbulent flow in a channel with rib roughness”, *Int. J. Heat Fluid Flow*, 24, 372-388.

DeGraaff, D. B. and Eaton, J. K. (2000) Reynolds-number scaling of the flat plate turbulent boundary layer. *J. Fluid Mech.,* 422, 319–346

DeGraaff, D. B. and Eaton, J. K. (2001). “A high-resolution laser Doppler anemometer: design, qualification, and uncertainty” *Exp. Fluids* 30 (5), 522-530.

Djenidi, L., Elavarasan, R. and Antonia, R. A. (1999). The turbulent boundary layer over transverse square cavities, *J. Fluid Mech*., 395, 271-294.

Djenidi, L., Antonia, R. A., Amielh, M. and Anselmet, F. (2007). “A turbulent boundary layer over a two-dimensional rough wall”, *Exp. Fluids*, DOI 10.1007/s00348-007-0372-5.

Durst, F., Melling, A. and Whitelaw, H., J. (1981). Principles and practice of laser Doppler anemometry, second edition, Academic Press Inc., New York.

Efron, B. (1979). “Computer and the theory of statistics: thinking the unthinkable”, *Soc. Ind. Appl Math Rev*., 21(4), 460-469.

Falco, R. H. (1977). “Coherent motions in the outer region of turbulent boundary layers.” *Phys. Fluids* 20, 124.

Flack, K. A., Schultz, M. P., and Connelly, J. S. (2007). “Examination of a critical roughness height for outer layer similarity”, *Phys. Fluids* 19 DOI:10.1063/1.2757708.

Forliti, D.J., Strykowski, P. J., and Debatin K. (2000) “Bias and precision errors of digital particle image velocimetry”. *Exp. Fluids* 28, 436-447.

Granville, P.S. (1976) “A modified law of the wake for turbulent shear layers”. *Trans. ASME I: J. Fluids Engg*. 98, 578–580.

Grass, A. J. (1971) “Structural features of turbulent flow over smooth and rough boundaries” *J. Fluid Mech*., 50, 233-255.

Guo, J., Julien, P.Y. and Meroney, R.N. (2005). “Modified log–wake law for zero-pressure-gradient turbulent boundary layers”. *J. Hydr. Res*., IAHR 43(4), 421–430.

Hinze, J. O. (1959). Turbulence: an introduction to its mechanism and theory, McGraw-Hill, NewYork.

Handler, R. A., Swean, Jr. T. F., Leighton, R. I. and Swearinngen, J. D. (1993). “Length scales and the energy balance for turbulence near a free surface” *AIAA J.,* 31(11), 1998-2007.

Hurther, D., Lemmin, U., and Terray, A. (2007). “Turbulent transport in the outer region of rough-wall open-channel flows: the contribution of large coherent shear stress structures (LC3S).” *J. Fluid Mech*., 574, 465-493.

Holmes, P., Lumley, J.L., and Berkooz, G. (1996). *Turbulence, coherent structures, dynamical systems and symmetry*, Cambridge University Press, NY, USA.

Ikeda, T. and Durbin, P. (2007). "Direct simulations of a rough –wall channel flow". *J. Fluid Mech.*, 571, 235-263.

Jackson, P. S. (1981). "On the displacement height in the logarithmic velocity profile." *J. Fluid Mech.*, 111, 15–25.

Jeong, J. and Hussain, F. (1995) "On the identification of a vortex". *J. Fluid Mech.* 285, 69–94.

Jiminez, J. (2004). Turbulent flows over rough walls, *Annu. Rev. Fluid Mech.*, 36: 173-196.

Jirka, G. H. (2001). "Large scale flow structures and mixing processes in shallow flows." *J. Hydr.* Res, 39(6), 567-573.

Jirka, G. H. and Uijttewaal, W. S. J. (2004) "Shallow flows", Taylor & Francis Group, London, ISBN 90 5809 700 5.

Kirkgoz, M. S. and Ardichoglu, M. (1997). "Velocity Profiles of Developing and Developed Open Channel Flow". *J. Hydrl. Engrg.*, 123(12), 1099–1105.

Kline, S. J., Reynolds, W C., Schraub, R.A. and Runstadler, P.W. (1967). "The structure of turbulent boundary layers." *J. Fluid Mech.*, 30, 741.

Klewicki, J. C. (1989). "On the interactions between the inner and outer region motions in turbulent boundary layers." PhD dissertation, Michigan State University, East Lansing, Michigan, USA.

Komori, S., Nagaosa R., Murakami Y., Chiba S., Ishii, K. and Kuwahara, K. (1993). "Direct numerical simulation of three-dimensional open-channel flow with zero-shear gas–liquid interface", *Phys. Fluids A* 5, 115-125.

Krogstad, P.-A., Bakken, O. M. and Ashrafian, A. (2005). “An experimental and numerical study of channel flow with rough walls.” *J. Fluid Mech.*, 530, 327–352.

Krogstad, P-A., Antonia, R. A. and Browne, L. (1992). “Comparison between rough-and-smooth-walled turbulent boundary layers”. *J. Fluid Mech*., 245, 599–617.

Krogstad, P-A. and Antonia, R. A. (1999). “Surface roughness effects in turbulent boundary layers” *Exp. Fluids*, 27, pp. 450-460.

Leonardi, S. (2002) “Turbulent channel flow with roughness: Direct Numerical Simulations” PhD thesis, Universita di Roma “La Sapienza”

Leonardi, S., Orlandi, P., Smalley, R. J., Djenidi, L. and Antonia, R. A. (2003) “Direct numerical simulations of turbulent channel flow with transverse square bars on the wall”. *J. Fluid Mech.*, 491, 229–238.

Leonardi, S., Orlandi, P., Djenidi, L. and Antonia, R. A. (2004). “Structure of turbulent channel flow with square bars on one wall.” *Int. J. Heat Fluid Flow*, 25, 384–392.

Leonardi, S., Orlandi, P., Djenidi, L. and Antonia, R. A. (2006). “Guidelines for modeling a 2D rough wall channel flow.” *Flow, Turbulence and combustion*, 77(1-4), 41-57.

Lee, S.-H., and Sung, H. J. (2007). “Direct numerical simulation of the turbulent boundary layer over a rod-roughened wall” *J. Fluid Mech.*, 584, 125-146.

Libby, P. (1996). An Introduction to Turbulence. Taylor and Francis Incorporated,Washington DC.

Liu, Z., Adrian, R. J., and Hanratty, T. J. (2001). “Large–scale modes of turbulent channel flow: transport and structure.” *J. Fluid Mech*., 448, 53-80.

Lumley, J. L. (1967) “The structures of inhomogeneous flow” In Proceddings of international colloquium on the fine scale structure of the atmosphere and its influence on radio wave propagation (ed. A. M. Yaglom and V.I. Tararsky), 166-178 Nauka, Moscow.

Lu, S. S., and Willmarth, W. W. (1973). “Measurements of the structures of the Reynolds stress in a turbulent boundary layer.” *J. Fluid Mech.*, 60, 481–571.

Mazouz, A., Labraga, L., and Tournier, C. (1998). “Anisotropy invariants of Reynolds stress tensor in a duct flow and turbulent boundary layer.” *ASME J. Fluids Engg.*, 120, 280–284.

Manes, C., Pokrajac, D. and McEwan, I. (2007). “Double-averaged open channel flows with small relative submergence”, *J. Hydr. Engrg., ASCE* 133(8): 896-904.

Meinhart, C. D. and Adrian, R. J. (1995) “On the existence of uniform momentum zones in a turbulent boundary layer.” *Phys. Fluids*, **7**, 694-696.

Nagano, Y., Hattori, H. and Houra, T. (2004),”DNS of velocity and thermal fields in turbulent channel flow with transverse-rib roughness” *Int. J. Heat Fluid Flow*, 25, 393-403.

Nakagawa, H. and Nezu, I. (1977). “Prediction of the contributions to the Reynolds Stress from Bursting Events in Open-Channel Flows”. *J. Fluid Mech*. 80(1), 99–128.

Nakagawa, S., and Hanratty, T. J. (2001). “Particle image velocimetry measurements of flow over a wavy wall.” *Phys. Fluids* ,13 , 3504-3507.

Nakagawa, H., and Nezu, I. (1977). “Prediction of the contributions to the Reynolds stress from bursting events in open-channel flow.” *J. Fluid Mech.*, 80, 99-128.

Naot, D. (1984) “ Response of the channel flow to roughness heterogeneity”, *J. Hydr. Engrg*., *ASCE* 110, 1568-1578.

Nezu, I. (2005). “Open-Channel Flow Turbulence and Its Research Prospect in the 21st Century”. *J. Hydr. Engrg*., 131(4), 229–246.

Nezu, I. and Nakagawa, H. (1993). Turbulence in Open Channel Flows. IAHR Monograph, A. A. Balkema, Rotterdam, The Netherlands.

Nezu, I. and Rodi, W. (1985)” Experimental study on secondary currents in open channel flow.” *Proc. of 21^{-st} IAHR Congress Melbourne*, 2, 115-119.

Nezu, I. and Rodi, W. (1986). “Open channel flow measurements with a laser Doppler anemometer.” *J. Hydr. Engrg.,* 112(5), 335-355.

Nikora, V., Goring, D., McEwan, I. and Griffiths, G. (2001). “Spatially averaged open-channel flow over rough bed” *J. Hydr. Engrg. ASCE* 127:123–133.

Nikora, V., Nokes, R., Veale, W., Davidson, M. and Jirka, G. H., “Large scale turbulent structure of uniform shallow free-surface flows”, *Env. Fluid Mech*., 7,159-172, 2007.

Okamoto, S., Seo, S., Nakaso, K. and Kawai, I. (1993). “Turbulent shear flow and heat transfer over the repeated two-dimensional square ribs on ground plane.” *J. Fluids Engg*., 115, 621-637.

Osterlund, J. (1999) “Experimental Studies of Zero Pressure-Gradient Turbulent Boundary Layer Flow”. PhD Thesis, Royal Institute of Technology Department of Mechanics, Stockholm.

Pan, Y. and Banerjee, S. (1995). ”A numerical study of free-surface turbulence in channel flow.” *Phys. Fluids*, 7(7), 1649-1664.

Panton, R. L. (2001). “Overview of the Self-Sustaining Mechanisms of Wall Turbulence”, *Prog. Aerospace Sci.*, 37, (4), 341-383.

Perry, A. E., Schofield, W. H. and Joubert, P. N. (1969).”Rough-wall turbulent boundary layers” *J. Fluid Mech*., 37, 383-413.

Poggi, D., Porporato, A., and Ridolfi, L. (2003). “Analysis of the small-scale structure of turbulence on smooth and rough walls. “ *Phys. Fluids*, 15(1), 35-46.

Pokrajac, D., Campbell, L.J., Nikora, V., Manes, C., and McEwan, I. (2007). “Quadrant analysis of persistent spatial velocity perturbations over square-bar roughness.” *Exps. Fluids*, 42, 413-423.

Pope, S. (2000). Turbulent flow, Cambridge University Press.

Prasad, A. K., Adrian, R. J., Landreth, C. C. ,and Offutt P.W., (1992). “Effect of resolution on the speed and accuracy of particle image velocimetry interrogation.” *Exps. Fluids*, 13, 105-116.

Rashidi, M. and Banerjee, S. (1990). “The Effect of Boundary Conditions and Shear Rate on Streak Formation and Breakdown in Turbulent Channel Flows.” *Phys. Fluids* 2(10), 1827–1838.

Raupach, M. R. (1981). ”Conditional statistics of Reynolds stress in rough-wall turbulent boundary layers” *J. Fluid Mech*., 108, 363-382.

Raupach, M. R., Antonia, R. A., and Rajagopalan, S., (1991), “Rough-Wall Turbulent Boundary Layers”, *Appl. Mechs. Revs*. 44, 1-25.

Robinson, S. K. (1991). “Coherent motions in the turbulent boundary layer.” *Annul. Rev. Fluid Mech.*, 23, 601-639.

Roussinova, V., Biswas, N. and Balachandar, R. (2008). “Revisiting turbulence in smooth uniform open channel flow.” *J. Hydr. Res.*, 46, 1, 36-48.

Schultz, M. P., and Flack, K. A. (2005). “Outer layer similarity in fully rough turbulent boundary layers”. *Exp. Fluids* 38, 328–340.

Shafi, H. S. and Antonia, R. A. (1995). “Anisotropy of the Reynolds stresses in a turbulent boundary layer on a rough wall.” *Exps. Fluids*, 18, 213-215.

Shinneeb, A.M., Bugg, J. D. and Balachandar R., (2004). “Variable threshold outlier identification in PIV data”, *Meas. Sci. Tech.*, 15, 1722-1732.

Shinneeb, A. M. (2006). “Confinement effects in shallow water jets.” PhD thesis, Univ. of Saskatchewan, Saskatoon, Canada.

Shinneeb, A. M., Balachandar, R. and Bugg, J. D. (2008).”Analysis of coherent structures in the far-field region on an axisymmetric free jet. ” to appear in *ASME J. Fluids Engg.*

Sirovich, L. (1987). “Turbulence and the dynamics of coherent structures. Part I: Coherent structures.” *Quar. Applied Math.*, 45(3), 561-571.

Singha, A., Shinneeb, A. M., and Balachandar, R. (2009). “PIV-POD investigation of the wake of a sharp-edged flat bluff body immersed in a shallow channel flow”, *J. Fluids Eng., ASME* 131 (2) DOI:10.1115/1.3054283.

Smalley, R. J., Leonardi, S., Antonia, R. A., Djenidi, L. and Orlandi, P. (2002). “Reynolds stress anisotropy of turbulent rough wall layers” *Exps. Fluids*, 33, 31-37.

Spalart, P. R. (1988). “Direct simulation of a turbulent boundary layer up to Re_θ = 1410.” *J. Fluid Mech.*, 187, 61-98.

Steffler, P.M., Rajaratnam, N. and Peterson, A.W. (1985). “LDA measurements in open channel”. *J. Hydr. Engrg.*, 111(1), 119–130.

Tachie, M.F. (2001). “Open channel turbulent boundary layers and wall jets on rough surfaces”. PhD Thesis, University of Saskatchewan, Saskatoon.

Tachie, M.F., Bergstrom, D.J. and Balachandar, R.(2003). “Roughness effects in low-Re_θ open-channel turbulent boundary layers”. *Exp. Fluids* 35(4), 338–346.

Tachie, M.F., Balachandar R., Bergstrom D.J., (2004) “Roughness effects on turbulent plane wall jets in an open channel“, *Exp. Fluids*, 37 (2), 281-292.

Tachie, M. F. and Adane, K. K. (2007). “PIV study of shallow open channel flow over d- and k-type transverse ribs.” *ASME J. Fluids. Engg.*, 129, 1058–1072.

Tachie. M. F., Bergstrom, D. J. and Balachandar, R. (2000). “Rough wall turbulent boundary layers in shallow open channel flow.” *ASME J. Fluids. Engg.*, 122, 533–541.

Theodorsen, T. (1955). “The structure of turbulence.” in 50 Jahre Grenzschictforschung, edited by H. Gortler and W. Tollmein (Friedrich Vieweg & Sohn, Braunschweig).

Tominaga, A., Nezu, I., Ezaki, K. and Nakagawa, H. (1989) “Three-Dimensional Turbulent Structure in Straight Open Channel Flows. “ *J. Hydr. Res.* 27 (1), 149-173.

Tomkins, S. D. and Adrian, R. J. (2003) “Spanwise structure and scale growth in turbulent boundary layers”. *J. Fluid Mech.*, 490, 37-74.

Townsend, A. A. (1976). The structure of turbulent shear flow. Cambridge: Cambridge University Press.

Volino, R. J., Schultz, M. P. and Flack, A. K. (2007).”Turbulence structure in rough- and smooth- wall boundary layers”. *J. Fluid Mech*., 592, 263-293.

Williams, J. J. R. (2005). “Curvilinear turbulence modeling of open channel flow”. *J. Hydr. Res*., *ASCE* 43(2), 158–164.

Wu, Y., and Christensen K. T., (2006) “Population trends of spanwise vortices in wall turbulence.” *J. Fluid Mech.*, 568, 55-76.

Zhou J., Adrian, R. J., Balachandar, S. and Kendall, T. M. (1999). “Mechanisms for generating coherent packets of hairpin vortices in channel flow.” *J. Fluid Mech*., 387, 353-396

APPENDIX A

UNCERTAINTY ESTIMATES AND VELOCITY VALIDATION

In this section, the uncertainty estimates in the velocity measurements are presented for both LDV and PIV measurements. The common sources of errors that deserve particular considerations are quantified and presented for both techniques. Validation of the present PIV measurements is also reported.

A.1. LDV measurements

The total uncertainty of the measured velocity consists of a bias component and a precision component. While the bias component of the uncertainty in the velocity measurements is related to the LDV instrument, the precision error can be caused by a number of factors. The five most important are: statistical uncertainty, data filtering, velocity bias, velocity gradient bias and errors due to noise. All of these errors have to be quantified and the square root of their sum of squares will determine the total uncertainty.

The statistical uncertainty is a random error and its influence on the measurements can be reduced with increasing number of samples. DeGraaff and Eaton (2001) have shown that statistical uncertainty has the largest contribution to the total uncertainty in calculating Reynolds shear stress and other higher-order moments in turbulent boundary layers. They reported that up to 70% of the local errors in the normal stresses ($\overline{u^2}, \overline{v^2}$) and Reynolds shear stress ($-\overline{uv}$) are due to the statistical uncertainty in the data reduction step. In the present LDV measurements 10,000 samples are acquired at every wall-normal location. The raw data were filtered by eliminating all samples outside the three standard deviations from the calculated mean value to avoid errors due to spurious samples. Removing these samples generates slightly depressed but more reliable higher-order statistics. To account for this, all turbulence statistics were calculated for both filtered and unfiltered data, and the entire difference between the two data sets was defined as the data filtering uncertainty. It was found that this contributes negligibly to the mean velocity uncertainty, but constitutes 25% to 50% of the total uncertainty of the higher-order moments.

Velocity bias is present for all LDV systems operating in "burst" detection mode, since each particle traversing the measuring volume can trigger a measurement. Assuming that the particles are uniformly distributed in the fluid, the likelihood of a particle passing through the measurement volume is proportional to the fluid velocity. In situations where the data density is high this bias can be minimized by equal time sampling of the processor. Alternatively, velocity histories can be created by re-sampling the velocity history in equal time intervals. When the data density is low, these methods are not viable since they operate by discarding many of the velocity samples. In the present LDV measurements a bias-elimination residence-time-averaging algorithm was used to minimize the effects of the velocity bias.

Due to the finite size of the measuring volume the LDV data are not really a point measurement but integrated in space over the measuring volume. Finite probe size may cause large velocity gradients and may also present difficulty in accurately locating the wall (y = 0). Durst et al., (1995) derived the following corrections for the higher-order moments:

$$\overline{u^2}_{meas} = \overline{u^2}_{true} + \frac{{d_m}^2}{16}\left(\frac{dU}{dy}\right)^2 + K \tag{A.1}$$

$$\overline{u^3}_{meas} = \overline{u^3}_{true} + \frac{3d^2}{16}\left(\frac{dU}{dy}\right)\left(\frac{d\overline{u^2}}{dy}\right) + \frac{d_m{}^2}{32}\left(\frac{d^2\overline{u^3}}{dy^2}\right) + K \qquad \text{(A.2)}$$

In the above equations, d_m denotes the diameter of the probe volume in the vertical direction and K denotes the higher-order moments. The above expressions showed that near the wall the higher–order moments are proportional to the gradient of the mean velocity. The near-wall measurements by Durst et al., (1995) have shown that the effect of the velocity gradients on the streamwise intensities is important only in the viscous region $y^+ \leq 3$. In the present rough and smooth wall LDV experiments, the closest vertical location where the velocities were measured reliably was at $y^+ = 15$ and 14, respectively. Consequently, the effect of the velocity gradient due to the finite size of the measuring volume is negligible.

In what follows, a detailed description of the uncertainty methodology used for quantifying the statistical uncertainty in higher-order moments on both smooth and rough surfaces is presented.

The first step in the uncertainty analysis is to determine if the raw velocity components follow normal distribution. If the normality condition is satisfied, by making an additional approximation that the velocity samples are independent and the number of samples is large (N > 30), the velocity variance might be predicted by the chi-square distribution (χ^2). The chi-square test is widely known but it is valid only for variables with normal distributions. However, most of the turbulent quantities of interest are not normally distributed. For example distributions of $\overline{u^3}$, $\overline{v^3}$, and correlation coefficients of arbitrary order do not follow the normal distribution. Benedict and Gould (1996) discussed three different statistical techniques for assessing the uncertainty estimates for turbulence statistics. The most general of these statistical techniques is the one based on the resampling algorithm known as the bootstrap method. The bootstrap algorithm also requires independence between the samples and it was first introduced by Efron (1979). The bootstrap's implementation consists of drawing randomly, with replacement *B* independent bootstrap samples. $\mathrm{X}_{\mathrm{boot1}}$, X_{boot2}, X_{boot3}, … X_{bootB}, each consisting of *N* values from the original data set, *X*. Replacement implies that each bootstrap sample is always drawn from the entire raw data set *X*. For each bootstrap sample, a bootstrap replication, $\hat{\theta}_{boot,\,i}$ $i = 1, 2, \ldots, B$, of the desired statistics is calculated. The bootstrap estimate of variance is defined as

$$\mathrm{var}(\hat{\theta})_{boot} = \frac{1}{B-1}\sum_{i=1}^{B}\left(\hat{\theta}_{boot,\,i} - \overline{\hat{\theta}_{boot}}\right)^2 \tag{A.3}$$

where

$$\overline{\hat{\theta}_{boot}} = \frac{1}{B}\sum_{i=1}^{B}\hat{\theta}_{boot,\,i} \tag{A.4}$$

An approximate 95% confidence interval for estimator, $\hat{\theta}$, follows as $\hat{\theta} \pm 1.96\left[\mathrm{var}(\hat{\theta})_{booot}\right]^{1/2}$. Benedict and Gould (1996) have shown that the number of bootstrap replications (*B*) needs to be higher than 100 to obtain satisfactory result. In the present calculations 2000 bootstrap replications were used.

Figure A-1 show an example of the estimated uncertainty for the smooth open channel flow at shallow depth (*d* = 0.06 m). The $\overline{u^2}$, $\overline{v^2}$ and $-\overline{uv}$ uncertainties within 95% confidence interval were calculated at every wall normal location and they are normalized with their local average. The statistical uncertainty at every location was calculated by either chi-square test or bootstrap method depending upon the results of the initial normality test. The turbulence uncertainties vary along the flow depth as shown in Figure A–1. However, in the center of the profiles (0.3 < *y/d* < 0.7) the uncertainties are fairly constant. The lowest uncertainty is calculated for the wall normal stress, $\overline{u^2}$ while the largest is estimated for the $-\overline{uv}$. In general the uncertainties in the higher-order correlations become higher near the wall and near the free surface since the local values of the velocity there tend to zero. The values listed in Table A–1 are the uncertainties calculated in the centre of the velocity profiles (*y/d* = 0.5), where they are found to be constant percentage of their local values. This table provides a general guideline for examining velocity profiles, noting that near-wall uncertainties are generally higher.

A similar procedure was used to estimate the uncertainty of the LDV measurements on the rough bed. For the rough OCF experiments, the highest estimated uncertainty in the mean velocity at 95% confidence interval was ± 2% for measurement locations near the roughness. Farther from the wall, the uncertainty in the mean velocity is reduced (< ±0.5%). In Table A–1 typical estimates of the uncertainty calculated at *y/d* = 0.5 on the rough bed are listed. To improve the reliability of the higher-order turbulent moments, initially all velocity instantaneous records are filtered to eliminate measurements outside the three standard deviations from the obtained mean value. The highest uncertainties in normal stresses, Reynolds shear stress and triple products estimated at the plane of the rib crests are ±2%, ±5% and ±15%, respectively.

Table A-1 Typical uncertainty estimates for smooth and rough OCF at *y/d* = 0.5.

	Smooth	Rough
U	±0.4%	±0.5%
$\overline{u^2}$	±0.8%	±1.0%
$\overline{v^2}$	±1.2%	±1.5%
$-\overline{uv}$	±2.5%	±3.0%
$\overline{u^3}$	±7.0%	±9.0%
$\overline{v^3}$	±9.0%	±10.0%
ρ_{uv}	±4.0%	±6.0%

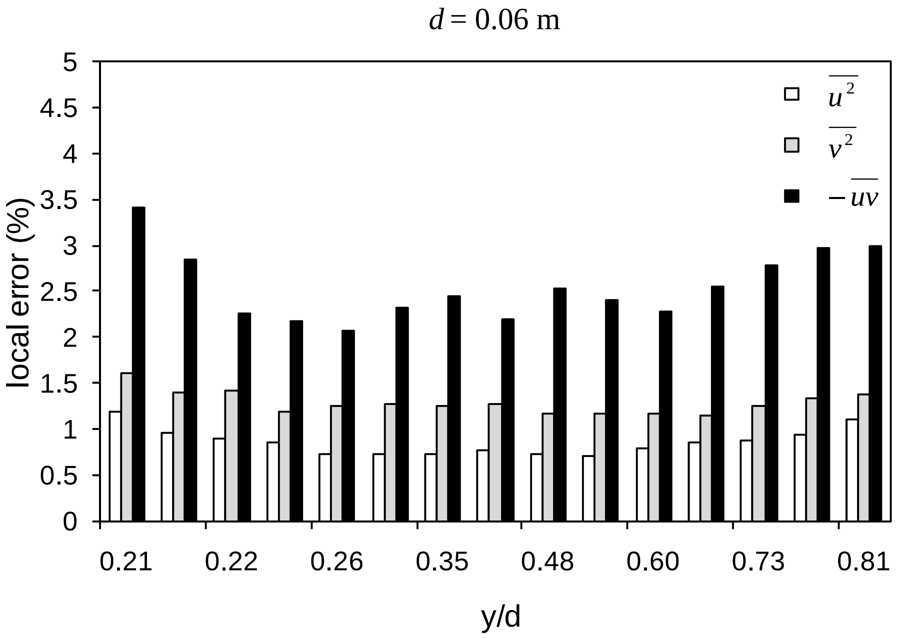

Figure A-1. Distribution of the uncertainties estimated along the depth of flow.

A.2. PIV measurements

The total uncertainty in the PIV measurements is also the sum of a precision component and a bias component. The bias component is due to the particle inability to follow the fluid, timing precision and error involved in the algorithm used to find the particle displacement. The error due to particle inability to follow the flow was considered negligible since the particles are very small and their density is very close to the fluid density. The timing error was also found to be negligible since the delay generator and the laser pulse duration was controlled internally by the PIV electronics. The raw PIV images were analysed prior to calculating the velocity vectors. The size of the particles in the individual PIV images was examined using *Matrox Inspector®* software. The average particle-image size was found to be approximately 10 pixels. Prasad et al., (1992) showed that when the ratio of particle image diameter to the pixel size is $d_{\text{par}}/d_{\text{pix}} > 3 – 4$, the bias uncertainty becomes negligibly small. The average velocity was calculated in every interrogation area from the particle displacements. The particle displacements are found from the peaks of the correlation function of the image grey-scale values. The sub-pixel position of these peaks is detected using Gaussian fitting algorithm. For the Gaussian peak-finding algorithm the error in average particle displacement is typically in the range 0.05 – 0.1 pixel (Forliti et al., 2000). For the displacement error of 0.1 pixel (conservative estimate) and laser pulse delay of 1800 μs the error in mean velocity was found to be 1.4%. The precision error of the velocity was evaluated from the standard deviation of the measured time series, assuming normal distribution in the velocities. For a confidence interval of 95% this error is equal to $1.96\sigma/\sqrt{N}$; where σ is the standard deviation of the velocity calculated from N

instantaneous velocity values. In our measurements the maximum standard deviation of velocity was 0.017 m/s corresponding to the relative error in velocity of ±0.4%. Hence, the combined measured uncertainty in the velocity evaluated from the bias and precision components becomes 1.45%.

A.3. PIV validation

Since the PIV is fairly recent velocity measurement technique which is still a subject of active research, it is of interest to compare and validate the turbulent statistics obtained from PIV to those from the LDV. To enhance the convergence, time averaging as well as spatial averaging has been performed along the streamwise direction *(x)*, supposing the homogeneity of the flow at the scale of the field-of-view. In what follows, statistics obtained from the PIV measurements are compared with the two-dimensional laser-Doppler velocimetry (LDV) measurements conducted in a rectangular tilting flume with 610 x 610 mm cross-section and 10 m long at water depth (= 0.10 m). The Reynolds number based on the total depth of flow is Re_d = 51,600.

Figure A-2 provide comparison of the mean velocity obtained from PIV and LDV measurements. The mean velocity profiles are computed by ensemble-averaging of 2000 velocity fields followed by a line-averaging in the streamwise direction in a manner similar to that described by Nakagawa and Hanratty (2001). The friction velocities, u_τ, listed in Table A-2 were determined for both LDV and PIV data using the Clauser chart method. More details for estimation of the friction velocity are provided in Chapter III. An excellent agreement is noted between the mean velocity profiles in the log-law format as shown in Figure A-2. The buffer layer is not resolved from the present PIV measurements and the closest point to the wall where the velocity was measured reliably was at $y^+ = 14$.

Figure A–3 shows the probability density functions of u′ computed from PIV experiments at $y^+ = 104$ and Re = 21000 in (x-y) plane. The same quantity from LDV experiments is also shown at $y^+ = 100$ and Re = 51600. The two distributions are in good agreement and no regular oscillations are present in the PIV data. Carlier and Stanislas (2005) observed regular oscillations with the period that corresponds to the length of 1 pixel in the image plane. These oscillations are due to the ‘peak locking effect’, which skews the evaluated displacement of particle images towards integer values of pixels. In the present measurements peak-locking effect does not appear, owing to the use of a more sophisticated peak-fitting algorithm which smoothes the random bias.

As the characteristics of existing turbulent structures will be looked in detailed in Chapter IV, it is of interest to examine the statistical properties of the vorticity extracted from the PIV data. The vorticity was computed from the instantaneous PIV maps by using a second order central difference scheme. The vorticity ($\overline{\omega_z'}$) was averaged over the ensemble of the 2000 maps to compute the mean profile in the wall normal direction. The RMS profile of the corresponding vorticity was calculated by subtracting the mean profile. Figure A-4 shows comparison of the RMS profile of the spanwise component of vorticity, $\overline{\omega_z'}$ together with the data of Spalart (1988) and Klewicki (1989). The RMS vorticity ($\overline{\omega_z'}^{1/2}$) is scaled with the depth of flow d and maximum velocity U_0 and it is plotted in outer scaling. In addition, to show the convergence of the present PIV data, $\overline{\omega_z'}$ was computed from different number of velocity maps (N) as indicated at Figure A-4.

The obtained profiles clearly show that the accuracy of the RMS vorticity improves with increasing number of *N*.

Table A-2. Experimental parameters

Measurement technique	**d (m)**	**U_0 (m/s)**	**u_τ (mm/s)**	**Δx^+** -	**Δy^+** -
PIV	0.10	0.19	9.5	7.8	7.8
LDV	0.10	0.49	24.3	-	-

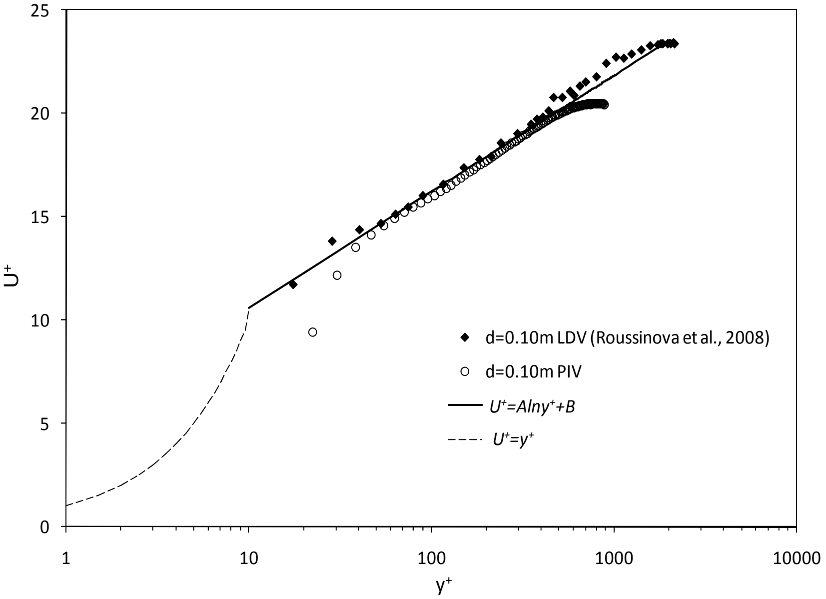

Figure A-2. Mean velocity profiles

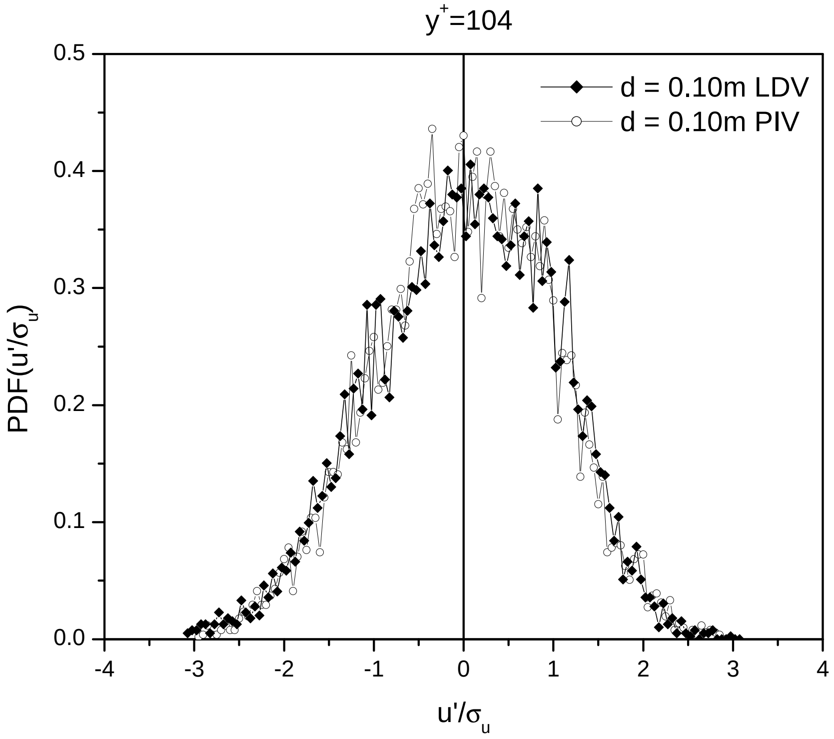

Figure A-3. Probability density function of u′ at $y^+ = 104$.

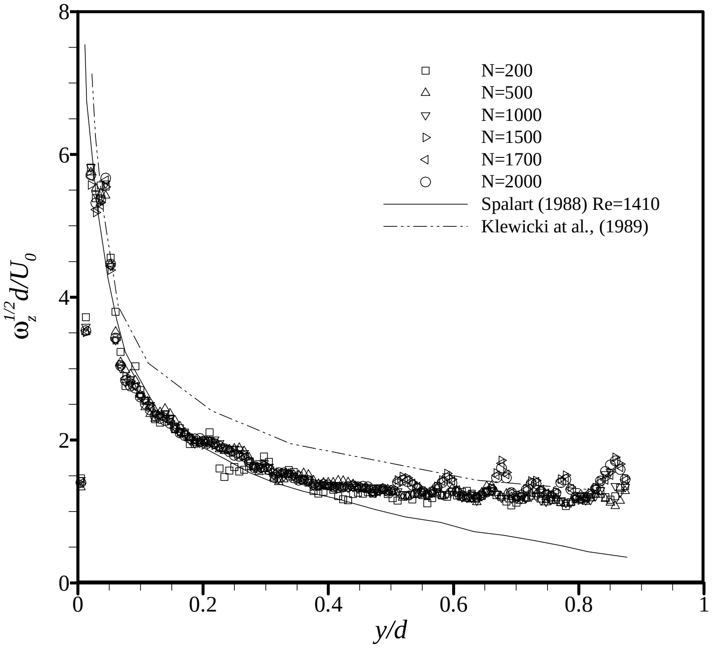

Figure A-4. Profiles of rms spanwise vorticity. For data sets by Spalart (1988) and Klewicki et al., (1989) vertical locations (y) are scaled with the thickness of the turbulent boundary layer (δ).

VITA AUCTORIS

NAME:	Vesselina Tzvetanova Roussinova
PLACE OF BIRTH:	Ihtiman, Bulgaria
YEAR OF BIRTH:	1970
EDUCATION	Sofia University, Sofia, Bulgaria 1990-1995, M.Sc. Engineering Physics
	University of Alberta, Edmonton, Alberta 1999-2001, M.Sc. Chemical Engineering
	University of Windsor, Windsor, Ontario 2004-2009, Ph.D., Civil and Environmental Engineering